



저작자표시-비영리-변경금지 2.0 대한민국

이용자는 아래의 조건을 따르는 경우에 한하여 자유롭게

- 이 저작물을 복제, 배포, 전송, 전시, 공연 및 방송할 수 있습니다.

다음과 같은 조건을 따라야 합니다:



저작자표시. 귀하는 원저작자를 표시하여야 합니다.



비영리. 귀하는 이 저작물을 영리 목적으로 이용할 수 없습니다.



변경금지. 귀하는 이 저작물을 개작, 변형 또는 가공할 수 없습니다.

- 귀하는, 이 저작물의 재이용이나 배포의 경우, 이 저작물에 적용된 이용허락조건을 명확하게 나타내어야 합니다.
- 저작권자로부터 별도의 허가를 받으면 이러한 조건들은 적용되지 않습니다.

저작권법에 따른 이용자의 권리는 위의 내용에 의하여 영향을 받지 않습니다.

이것은 [이용허락규약\(Legal Code\)](#)을 이해하기 쉽게 요약한 것입니다.

[Disclaimer](#)

공학박사 학위논문

**Novel Synthesis of Copper Nanowires  
and Hybrid Nanocomposites with  
Carbon for Functional Electrodes**

기능성 전극을 위한 구리 나노선과 탄소  
복합체 물질의 합성 연구

2018년 2월

서울대학교 융합과학기술대학원

융합과학부 나노융합전공

Zhenxing Yin

# Novel Synthesis of Copper Nanowires and Hybrid Nanocomposites with Carbon for Functional Electrodes

지도 교수 김 연 상

이 논문을 공학박사 학위논문으로 제출함  
2018년 2월

서울대학교 융합과학기술대학원  
융합과학부 나노융합전공  
Zhenxing Yin

Zhenxing Yin의 공학박사 학위논문을 인준함  
2018년 1월

위 원 장 박 원 철 (인)

부위원장 김 연 상 (인)

위 원 김 기 재 (인)

위 원 한 철 중 (인)

위 원 유 지 영 (인)

## **Abstract**

# **Novel Synthesis of Copper Nanowires and Hybrid Nanocomposites with Carbon for Functional Electrodes**

Zhenxing Yin

Program in Nano Science and Technology

Graduate School of Convergence Science & Technology

Seoul National University

As a new type of promising conductive nanomaterials, copper nanowire (Cu NW) and their nanocomposites have been widely investigated for various functional conductive electrodes, due to their solution-process ability, low cost, high conductivity and excellent flexibility. Compared with general nano-shapes, such as sphere, cube and plate, the Cu NWs have many unique properties, because of their unique one dimensional structure with a high aspect ratio. In this work, our research has primarily focused on

the Cu NWs and their nanocomposites synthesis with shape control and special electrode applications for next generational electronics.

Firstly, a whole manufacturing process of the curved Cu NWs (CCNs) based flexible transparent conductive electrode (FTCE) with all solution process was introduced as an alternative for Indium tin oxide (ITO), due to their excellent opto-electrical property and flexibility. Although a traditional transparent electrode of ITO has an outstanding opto-electrical performance, as a ceramic material, the brittleness is a critical limitation to apply for various flexible devices. Interestingly, the highly purity and good quality CCNs are designed and synthesized by a binary polyol co-reduction method. In addition, a meniscus-dragging deposition method is used to uniformly coat the well-dispersed CCNs on the glass or polyethylene terephthalate (PET) substrate with vacuum-free and transfer-free conditions. Furthermore, networking of the CCNs was achieved by a solvent-dipped annealing method to fabricate the FTCE at the low temperature of 50 °C. The CCNs thin film on PET substrate exhibited high transparency (86.62% at 550 nm), low sheet resistance ( $99.14 \Omega \cdot \square^{-1}$ ), and excellent flexibility and durability ( $R/R_0 < 1.05$  at 2000 bending, 5 mm of bending radius).

Secondly, we introduce an all-solution fabrication of the CCNs-based FTCEs utilizing a combination of self-designed innovative techniques, such

as multi-polyol synthetic method, meniscus-dragging deposition method, polyurethane (PU)-stamped patterning method, solvent-dipped welding method and PU-embedded transfer method. These suggested methods effectively solved the technical problems of the high-cost fabrication, the low robustness, the high roughness and the difficulty of patterning. As a result, the CCNs thin film partially embedded into PU matrix exhibited excellent opto-electrical performance ( $R_s = 53.48 \Omega \cdot \square^{-1}$  at  $T = 85.71\%$ ) and high mechanical stabilities ( $R/R_0 < 1.02$  at 1,000<sup>th</sup> bending and  $R/R_0 < 1.10$  at 10<sup>th</sup> tape peeling) with low surface roughness ( $R_{rms} = 14.36$  nm).

Thirdly, the reduced graphene oxide (RGO) nanosheets bridging oriented copper NWs were introduced for flexible, annealing-free and air-stable electrode. The RGO nanosheets connecting the Cu NWs not only provided conductive pathways for electron transfer but also acted as a protective layer of oxidation on contact points. As a result, the composite film exhibits a low sheet resistance ( $0.808 \Omega \cdot \square^{-1}$ ) and high flexibility (1,000<sup>th</sup> bending) without considerable change over 30 days. Furthermore, the Cu NW-RGO composites can be filtered on polyester cloth as a lightweight wearable conductor with high durability and simple process-ability, which are highly promising in kinds of electronic devices.

Finally, the novel 3-D Cu NW-MWCNT composites were introduced as a

promising battery anode for fast charge-discharge lithium ion battery (LIB). When composite film formed, both Cu NWs and MWCNT as the highly conductive 1-D nanomaterials present tremendous advantages to be applied to the current collector and active materials for LIBs, because their high aspect ratio and large surface areas induce better transport for electrons and ions. As an advanced anode for LIBs, the Cu NWs-MWCNT composite film exhibited low sheet resistance and excellent stability with high flexibility. The 3-D porous architecture of Cu NWs is strongly contact with the MWCNTs leads to the improvement of the LIB performances. Furthermore, both half cell and full cell showed high specific capacities ( $466 \text{ mAh}\cdot\text{g}^{-1}$  and  $113 \text{ mAh}\cdot\text{g}^{-1}$  at 0.2 C) with a high columbic efficiency, even operated at a high current ( $215 \text{ mAh}\cdot\text{g}^{-1}$  and  $48 \text{ mAh}\cdot\text{g}^{-1}$  at 5 C). When applied for flexible LIBs, the specific capacity still remained 92.8% after bending 1,000 cycles.

**Keywords: Copper nanowire, Flexible transparent electrode, Wearable electrode, Lithium ion battery, Current collector.**

**Student Number: 2014-31481**

# Contents

<b>Abstract.....</b>	<b>i</b>
<b>List of figures .....</b>	<b>x</b>
<b>List of schemes .....</b>	<b>xviii</b>
<b>List of tables .....</b>	<b>xix</b>
<b>Chapter 1. Introduction .....</b>	<b>1</b>
1.1 Background on the Cu nanomaterials .....	1
1.2 Shape control of Cu nanomaterials .....	5
References.....	8
<b>Chapter 2. Literature and Dissertation Overview .....</b>	<b>9</b>
2.1 Synthetic methods of Cu NWs and their nanocomposites.....	9
2.2 Networking of Cu NWs for conductive electrode .....	14
2.3 Dissertation overview .....	19
References.....	24
<b>Chapter 3. Novel Synthesis, Coating and Networking of     Curved Copper Nanowires for Flexible     Transparent Conductive Electrodes.....</b>	<b>26</b>
3.1 Introduction.....	26

3.2 Experimental section.....	29
3.2.1 CCNs preparation .....	29
3.2.2 Linear Cu NWs preparation .....	29
3.2.3 CCNs films fabrication.....	30
3.2.4 CCNs and films Characterization.....	31
3.3 Results and discussion .....	32
3.3.1 Overview of whole process .....	32
3.3.2 Binary polyol co-reduction method.....	34
3.3.3 Meniscus-dragging deposition .....	45
3.3.4 Solvent-dipped annealing method .....	47
3.3.4 Flexible transparent conductive electrode.....	52
3.4 Conclusion .....	57
References.....	58

**Chapter 4. Curved Copper Nanowires-based Robust Flexible Transparent Electrodes via All-solution Approach..... 61**

4.1 Introduction.....	61
4.2 Experimental section.....	65
4.2.1 Preparation of CCNs via multi-polyol synthesis.....	65
4.2.2 CCN film coating via MDD .....	65

4.2.3 CCN film patterning via PU-stamped patterning.....	66
4.2.4 CCN percolation via solvent-dipped welding .....	67
4.2.5 CCN film smoothing via PU-embedded transfer .....	67
4.2.6 Characterization of CCNs and FTCEs .....	68
4.3 Results and discussion .....	69
4.3.1 Synthesis process.....	69
4.3.2 Coating process.. ..	77
4.3.3 Patterning process.....	83
4.3.4 Welding process .....	84
4.3.5 Transfer process .....	92
4.3.6 Flexible transparent conductive electrode.....	95
4.4 Conclusion .....	101
References.....	102

**Chapter 5. Bridging Oriented Copper Nanowire-  
Graphene Composites for Solution-Processable,  
Annealing-Free, and Air-Stable Flexible  
Electrodes..... 105**

5.1 Introduction.....	105
5.2 Experimental section.....	109
5.2.1 Reagents .....	109
5.2.2 Apparatus.....	109

5.2.3 Preparation of Cu NW-RGO composites .....	110
5.2.4 Fabrication of electrodes .....	110
5.3 Results and discussion .....	111
5.3.1 Solvothermal synthesis of CuNW-RGO composites ..	111
5.3.2 Unique properties of Cu NW-RGO composites .....	124
5.3.3 Flexible and wearable electrodes .....	135
5.4 Conclusion .....	140
References.....	141

**Chapter 6. Copper Nanowire/Multi-walled Carbon Nanotube Composites as All-nanowire Flexible Electrode for Fast-Charging/Discharging Lithium-ion Battery ..... 145**

6.1 Introduction.....	145
6.2 Experimental section.....	149
6.2.1 Synthesis of CuNWs .....	149
6.2.2 Fabrication of CNMC anodes.....	150
6.2.3 Material characterizations .....	150
6.2.4 Electrochemical measurements .....	151
6.3 Results and discussion .....	153
6.3.1 Preparation and characterization of CNMC anode.....	153
6.3.2 Properties and merits of CNMC anode ... ..	157

6.3.3 Electrochemical analysis of CNMC anode .....	169
6.3.4 Flexible lithium-ion battery .....	178
6.4 Conclusion .....	180
References.....	181
<b>Chapter 7. Conclusion.....</b>	<b>184</b>
<b>(Appendix) Chapter 8. Rose Rock-shaped Nano Cu<sub>2</sub>O     anchored Graphene for High-Performance     Supercapacitors via Solvothermal Route.....</b>	<b>186</b>
8.1 Introduction.....	186
8.2 Experimental section.....	191
8.2.1 Reagents .....	191
8.2.2 Apparatus.....	191
8.2.3 Preparation of Cu <sub>2</sub> O-GN composite.....	192
8.2.4 Electrochemical testing .....	193
8.3 Results and discussion .....	194
8.3.1 Characterization of Cu <sub>2</sub> O-GN composite.....	194
8.3.2 Formation mechanism of Cu <sub>2</sub> O-GN composite ... ..	200
8.3.3 Electrochemical tests.....	211
8.4 Conclusion .....	221
References.....	222

국 문 초 록 ..... 226

## List of figures

**Figure 1.1** (a) Applications of NPs in the various fields. (b) Color change of the various solutions with different size, shape and composition of NPs. (c) The NPs-based flexible sensors with three different types. (d) Synthesis and treatment of various NPs for biomedical applications.

**Figure 1.2** (a) SEM image and (b) UV absorption of the monodisperse Cu NPs. (c) Photograph of the Cu NPs-based highly conductive electrode on polyimide substrate.

**Figure 1.3** The reaction routes of that leading of the metal nuclei grows to various different shapes of NPs.

**Figure 2.1** (a) Photograph of (b) schematic image of the low-temperature PECVD for preparation of CuNW-Graphene core-shell nanostructure with a radio frequency plasma system. (c–e) HR-TEM images and line intensity profile of the CuNW-Graphene core-shell nanostructure. (f–h) EDS analysis of Cu and C elements for demonstration of the CuNW-Graphene core-shell nanostructure.

**Figure 2.2** Synthetic mechanism for the growth of Cu NWs in reverse micelle system.

**Figure 2.3** Various coating method for the fabrication of NWs-based electrodes. (a) Spin coating,<sup>1</sup> (b) spray coating, (c) meyer rod coating, and (d) vacuum filtration.

**Figure 2.4** Various networking types of the Cu NWs with different

resistance. (a) non-contact type, (b) contact type, and (c) percolation type.

**Figure 3.1** SEM images of copper nanowires synthesized by different ratios of binary solvents. (a) 30 mL EG and 0 mL GC, (b) 20 mL EG and 10 mL GC, (c) 10 mL EG and 20 mL GC, (d) 0 mL EG and 30 mL GC.

**Figure 3.2** SEM images of Cu NWs synthesized by different reaction time at 208 °C. (a) 1 min, (b) 20 min, (c) 1 h and (d) 2 h.

**Figure 3.3** (a) Representative SEM image of CCNs. (b) XRD patterns. (c) SAED pattern of the slightly CCNs along the [110] zone axis, corresponding to the top-view TEM image. (d) UV–vis absorption spectrum.

**Figure 3.4** (a) SEAD pattern of CCNs. (b) TEM and (c) enlarged TEM image of black boxed areas.

**Figure 3.5** SEM images of typical (a, b) single CCN, (c, d) twisted CCNs and (e) ring structure.

**Figure 3.6** (a) UV–vis transmission spectra of CCNs thin film on glass substrate before and after washing. (b) UV–vis transmission spectra of CCNs thin films with different deposition number. (c) Sheet resistance and transmittance at 550 nm as a function of deposition number. (d) Optical microscopy images of two representative electrodes of 80.07% and 88.40%.

**Figure 3.7** A plot of transmittance at 550 nm versus sheet resistance for CCNs thin films on glass substrate compared with other groups.

**Figure 3.8** (a) UV–vis transmission spectrum and (b) SEM image of curved Cu NWs (CCNs) thin film ( $T = 86.62\%$ ,  $R_s = 99.14 \Omega \cdot \square^{-1}$ ) on

PET substrate. (c) Photographs of CCNs-based FTCE, and lighting of an LED with an external power supply.

**Figure 3.9** The relative resistance of linear Cu NWs and curved Cu NWs (CCNs) based FTCE under (a) cycling number of bending and (b) bending radius of 20, 15, 10, and 5 mm.

**Figure 4.1** SEM images of copper nanowires synthesized by different binary solvents. (a) 10 mL GC and 20 mL DEG, (b) 10 mL GC and 20 mL EG, (c) 10 mL PEG<sub>200</sub> and 20 mL EG, (d) 10 mL PEG<sub>400</sub> and 20 mL EG.

**Figure 4.2** SEM images of copper nanowires synthesized by different ratio of mixed polyol solvents. (a) 2.5 mL PEG<sub>200</sub>, 10 mL GC and 17.5 mL EG, (b) 5 mL PEG<sub>200</sub>, 10 mL GC and 15 mL EG, (c) 7.5 mL PEG<sub>200</sub>, 10 mL GC and 12.5 mL EG, (d) 10 mL PEG<sub>200</sub>, 10 mL GC and 10 mL EG.

**Figure 4.3** Representative (a–c) SEM and (d) XRD images of CCNs synthesized with the optimal ratio of 15 mL of EG, 10 mL of GC, and 5 mL of PEG<sub>200</sub>.

**Figure 4.4** (a) Large-scale coating of the CCNs on the PI film. (b) Control of the transmittance according to the coating conditions in the MDD. (c) OM and (d) SEM images of uniformly coating the CCNs on the PI film.

**Figure 4.5** (a) TEM image of the CCN with 4–10 nm of natural oxide layer when preserved after 2 days. (b) TEM image of the CCN after PEG<sub>200</sub>-dipped reduction process at 200 °C for 30 min.

**Figure 4.6** (a, b) SEM and (c, d) HR-TEM images of the percolated CCN network formed via the solvent-dipped welding method.

**Figure 4.7** (a) HR-TEM image and live FFT patterns of welded CCNs. (b) Corresponded schematic image of welding.

**Figure 4.8** (a) Transmittance of CCN thin films under various coating conditions before and after washing. (b) Plot of the transmittance at 550 nm vs. the sheet resistance for CCN thin films on the PI substrate and comparison with other groups. (c) Oxidation stability of the CCN thin films before and after welding within 10 days.

**Figure 4.9** Relative resistance ( $R/R_0$ ) of CCN thin films after transfer to the PU matrix with (a) different pre-curing times at a pressure of  $0.12 \text{ N}\cdot\text{cm}^{-2}$  and a pressing time of 30 min, (b) different pressures at a pre-curing time of 10 h and a pressing time of 30 min, and (c) different pressing times at a pre-curing time of 10 h and a pressure of  $0.12 \text{ N}\cdot\text{cm}^{-2}$ .

**Figure 4.10** (a) UV-vis transmission spectrum and (b) AFM image of the CCN thin film ( $T = 85.71\%$ ,  $R_s = 53.48 \text{ }\Omega\cdot\text{cm}^{-1}$ , and  $R_{rms} = 14.36 \text{ nm}$ ) on a PU matrix. (c) Relative resistance of the CCN thin film embedded on the PU matrix with 10 tape-peeling repetitions. (d) OM images of a  $20\text{-}\mu\text{m}$  line-space patterned CCN thin film ( $80.88\%$   $T$  of the sample, after washing) embedded on a PU matrix.

**Figure 4.11** (a) Lighting images of a light-emitting diode connected by the CCN thin film ( $T = 85.71\%$ ,  $R_s = 53.48 \text{ }\Omega\cdot\text{cm}^{-1}$ ) on PU/PET with an external power supply. The relative resistance of the CCN thin film partially embedded into the PU/PET under bending with radii of (b) 20, 15, 10, and 5 mm and (c) the cycling number of the bending with a 5-mm radius.

**Figure 5.1** (a, b) SEM images of Cu NW-RGO composites. (c) TEM image of Cu NW-RGO composites. (d) XRD pattern of Cu NW-RGO composites.

**Figure 5.2** (a, c) HR-TEM images and (b, d) corresponding FFT patterns of the Cu NW on composites with different incident electron beam.

**Figure 5.3** SEM images of Cu NW-RGO composites prepared by different concentrations of GO: (a) 0.25, (b) 0.75, (c) 1.25, and (d) 1.75  $\text{g}\cdot\text{L}^{-1}$ . Other conditions: 0.06  $\text{mol}\cdot\text{L}^{-1}$  CuCl, 0.1  $\text{mol}\cdot\text{L}^{-1}$  oleylamine, 0.01  $\text{mol}\cdot\text{L}^{-1}$   $\text{NH}_4\text{Cl}$ , 180  $^\circ\text{C}$ , 10 h.

**Figure 5.4** SEM images of Cu NW-RGO composites prepared by the different concentrations of oleylamine: (a) 0, (b) 0.05, (c) 0.1, and (d) 0.15  $\text{mol}\cdot\text{L}^{-1}$ . Other conditions: 0.06  $\text{mol}\cdot\text{L}^{-1}$  CuCl, 0.75  $\text{g}\cdot\text{L}^{-1}$  GO, 0.01  $\text{mol}\cdot\text{L}^{-1}$   $\text{NH}_4\text{Cl}$ , 180  $^\circ\text{C}$ , 10 h.

**Figure 5.5** SEM images of Cu NW-RGO composites prepared by the different heating rate: (a) 6 and (b) 3  $^\circ\text{C}\cdot\text{min}^{-1}$ . Other conditions: 0.75  $\text{g}\cdot\text{L}^{-1}$  GO, 0.06  $\text{mol}\cdot\text{L}^{-1}$  CuCl, 0.1  $\text{mol}\cdot\text{L}^{-1}$  oleylamine, 0.01  $\text{mol}\cdot\text{L}^{-1}$   $\text{NH}_4\text{Cl}$ , 180  $^\circ\text{C}$ , 10 h.

**Figure 5.6** (a) Sheet resistance of Cu NW-RGO composite films ( $5\text{ mg}\cdot\text{cm}^{-2}$ ) with different GO concentration: 0, 0.25, 0.5, 0.75, and 1.00  $\text{g}\cdot\text{L}^{-1}$ . (b) The sheet resistance of Cu NW-RGO composite films with different surface density: 1, 2, 3, 4, and 5  $\text{mg}\cdot\text{cm}^{-2}$ . (c) Changes in the resistance ratio of pure Cu NW films and Cu NW-RGO films kept at (c1) room temperature for 30 days, (c2) 60  $^\circ\text{C}$  for 5 h, and (c3) 100  $^\circ\text{C}$  for 150 min.

**Figure 5.7** (a) Photograph of the Cu NW-RGO composites filtered on a polyester cloth. (b) Photograph of the Cu NW-RGO composites on a polyester cloth with strong bending and lighting of an LED

with an external power supply. (c) The relative resistance of Cu NW-RGO film under 1,000 times of bending cycle. (d) The relative resistance of Cu NW-RGO film under 20, 15, 10, and 5 mm of bending radius.

**Figure 5.8** Photographs of Cu NW-RGO composites deposited on polyester fabric for wearable conductive electrode.

**Figure 6.1** Scanning electron micrographs of two types of proposed 1D nanomaterials and their composite: (a) CuNWs, (b) MWCNTs, and (c) CNMC7. (d) X-ray diffraction patterns of MWCNTs and CNMCs.

**Figure 6.2** (a) Schematic illustration of the conventional anode and proposed CNMC anode. (b) Sheet resistance of CNMC, MWCNT, and CuNW films. (c) Electrochemical impedance spectra of the half cells using CNMC7 and MWCNT as the anode in the frequency range of 1 MHz to 0.1 Hz. (d) Internal resistance of half cells with respect to the state of charge and the depth of discharge. The inset graphs show the GITT analysis, with CNMC7 and MWCNT as the anode.

**Figure 6.3** The photographs of 647  $\mu\text{m}$  of thick CNMC7 electrode, fabricated by a simple filtration method.

**Figure 6.4** (a) The SEM image of the full-cell cathode of  $\text{LiFePO}_4/\text{MWCNT}$  composites (1:2 of weight ratio). (b) Impedance analysis of the full cells using CNMCs and MWCNT as the anodes in frequency from 1 MHz to 0.1 Hz, where employed PP separator,  $\text{LiPF}_6$  of electrolyte and  $\text{LiFePO}_4/\text{MWCNT}$  of cathode, as described in Scheme 6.1.

**Figure 6.5** SEM image of CuNWs welding in CNMC7 anode.

**Figure 6.6** (a) Tap density of anodes with different composite ratios (w/w). (b) Photograph of the swelling test of the CNMC7 and MWCNT electrodes. After wetting with the electrolyte (1 M LiPF<sub>6</sub> in EC/DMC/DEC = 1:1:1, v/v/v), the CNMC7 film exhibited no change, but the area of the MWCNT film was expanded by approximately 16%. (c, d) Li<sup>+</sup> diffusion coefficient of half cells using CNMC7 and MWCNT anodes with respect to the state of charge and the depth of discharge, calculated from the GITT measurement.

**Figure 6.7** (a) Rate capability of various CNMC and MWCNT anodes. (b) Cycling performance and Coulombic efficiency of various CNMC and MWCNT anodes (after 31<sup>st</sup> cycle of rate-capability test). (c) Plot of the voltage (vs. Li/Li<sup>+</sup>) vs. the state of charge and depth of discharge for CNMC7 and MWCNT anodes in half cells. (d) Rate capability of CNMC and MWCNT anodes in the full cell with a PP separator, LiPF<sub>6</sub> electrolyte, and LiFePO<sub>4</sub>/MWCNT cathode.

**Figure 6.8** Volumetric capacities of MWNCT and CNMC anodes with rate performance.

**Figure 6.9** (a–e) The discharge curves of half cells at 0.2 C rate in initial cycle and 1<sup>st</sup> cycle, which made by CNMC and MWCNT anodes. (f) A diagram of relative reversible capacity ( $C_1/C_0$ ) of half cells in 1<sup>st</sup> cycle, comparing the CNMC and MWCNT anodes.

**Figure 6.10** (a) Charge/discharge curves of the full cells at 0.2 C in the 1<sup>st</sup> cycle, with anodes made of CNMC7 and MWCNT. (b) Cyclic voltammogram of an MWCNT electrode at a scan rate of 0.1 mV·s<sup>-1</sup> from -1.0 to 2.5 V (vs. Li/Li<sup>+</sup>).

**Figure 6.11** (a, b) Photographs of a flexible CNMC7 anode film. (c, d) Red LED powered by a flexible LIB. (e) Relative discharge capacity ( $C/C_i$ ) of the flexible LIB after numerous bending cycles.

**Figure 8.1** (a) XRD pattern of rose rock-shaped  $\text{Cu}_2\text{O}$ -GN composite. (b) TEM image of rose rock-shaped  $\text{Cu}_2\text{O}$ -GN composite. (c) High magnification TEM image of representative  $\text{Cu}_2\text{O}$ -GN composite. (d) HR-TEM image of  $\text{Cu}_2\text{O}$  surface with three different fringe lattices spacing, and corresponding (e) FFT pattern.

**Figure 8.2** (a) Wide scan XPS spectra of  $\text{Cu}_2\text{O}$ -GN, deconvoluted XPS spectra of (b) GO and (c, d)  $\text{Cu}_2\text{O}$ -GN.

**Figure 8.3** SEM images with low magnification and high magnification of  $\text{Cu}_2\text{O}$ -GN composite prepared by the different concentrations of PVP ( $\text{g}\cdot\text{L}^{-1}$ ): (a, b) 10 and (c, d) 0. Other conditions:  $0.06 \text{ mol}\cdot\text{L}^{-1}$   $\text{CuCl}_2$ ,  $5 \text{ g}\cdot\text{L}^{-1}$  NaAc,  $1 \text{ g}\cdot\text{L}^{-1}$  GO,  $160 \text{ }^\circ\text{C}$ , 20 h.

**Figure 8.4** (a–c) SEM images of  $\text{Cu}_2\text{O}$ -GN composite prepared by the different concentrations of GO ( $\text{g}\cdot\text{L}^{-1}$ ): (a) 1, (b) 2, and (c) 3. Other conditions:  $0.06 \text{ mol}\cdot\text{L}^{-1}$   $\text{CuCl}_2$ ,  $5 \text{ g}\cdot\text{L}^{-1}$  NaAc,  $160 \text{ }^\circ\text{C}$ , 20 h. Additionally, (d–f) SEM images of  $\text{Cu}_2\text{O}$ -GN composite prepared by the different concentrations of NaAc ( $\text{g}\cdot\text{L}^{-1}$ ): (d) 1, (e) 5, and (f) 10. Other conditions:  $0.06 \text{ mol}\cdot\text{L}^{-1}$   $\text{CuCl}_2$ ,  $3 \text{ g}\cdot\text{L}^{-1}$  GO,  $160 \text{ }^\circ\text{C}$ , 20 h.

**Figure 8.5** (a, b) SEM images of  $\text{Cu}_2\text{O}$ -GN composite prepared by the different concentrations of  $\text{CuCl}_2$  ( $\text{mol}\cdot\text{L}^{-1}$ ): (a) 0.06 and (b) 0.12. Other conditions:  $3 \text{ g}\cdot\text{L}^{-1}$  GO,  $5 \text{ g}\cdot\text{L}^{-1}$  NaAc,  $160 \text{ }^\circ\text{C}$ , 20 h. Additionally, (c, d) SEM images of  $\text{Cu}_2\text{O}$ -GN composite prepared by the different heating rate ( $^\circ\text{C}\cdot\text{min}^{-1}$ ): (c) 6 and (d) 3. Other conditions:  $0.06 \text{ mol}\cdot\text{L}^{-1}$   $\text{CuCl}_2$ ,  $3 \text{ g}\cdot\text{L}^{-1}$  GO,  $5 \text{ g}\cdot\text{L}^{-1}$  NaAc,

160 °C, 20 h.

**Figure 8.6** (a) CV curves of Cu<sub>2</sub>O-GN and GN in 6 mol·L<sup>-1</sup> KOH with 0.05 V·s<sup>-1</sup> at 25 °C. (b, c) Charge-discharge curves of Cu<sub>2</sub>O-GN electrode. (d) The relationship between the specific capacitance and the current of Cu<sub>2</sub>O-GN prepared at different concentrations of GO. (e) Ragone plots of Cu<sub>2</sub>O-GN with different concentrations of GO. (f) Specific capacitance retention of Cu<sub>2</sub>O-GN at a constant current of 1.0 A·g<sup>-1</sup>.

**Figure 8.7** Electrochemical performance of Cu<sub>2</sub>O-GN electrodes for symmetric supercapacitors: (a) CV curves at different scan rates from 0.01 to 0.2 V·s<sup>-1</sup>. (b) Charge-discharge curves at different mass normalised current from 1.0 to 10.0 A·g<sup>-1</sup>. (c) The relationship between the specific capacitance under different current densities from 1.0 to 10.0 A·g<sup>-1</sup>. (d) The corresponding Ragone plots related to specific energy and specific power of Cu<sub>2</sub>O-GN.

## List of schemes

**Scheme 3.1** Fabrication of curved copper nanowires (CCNs)-based flexible transparent conductive electrode (FTCE), including synthesis, coating, and networking.

**Scheme 3.2** Mechanism comparison of the synthesis of linear shape and curved shape of Cu NWs.

**Scheme 4.1** Fabrication of the smooth, robust, and patternable CCN-based FTCEs via all-solution processes, including synthesis, coating, patterning, welding, and transfer. In the MDD, the flow speed of the upper layer was higher than that of the lower layer. This flow-speed difference (indicated by parallel arrows in solvent) caused the wires to form an orderly arrangement on the substrate.

**Scheme 5.1** Fabrication of Cu NW-RGO composite wearable electrode.

**Scheme 5.2** Schematic illustration of the electron transference in (a) Cu NW-RGO composites without annealing, (b) Cu NW/RGO physical mixture without annealing and (c) Cu NWs without annealing.

**Scheme 6.1** Schematic illustration of the CNMC anode film preparation and their application in battery cells (half cell and full cell).

## List of tables

**Table 4.1** Process characteristics of various solution processes for thin film coating.

**Table 5.1** Sheet resistances in the different surface density.

**Table 5.2** The film thicknesses, sheet resistances, and electrical conductivities and resistivities of Cu NW/RGO physical mixture and Cu NW-RGO composite films with different GO concentration: 0, 0.25, 0.5, 0.75, and 1.00 g·L<sup>-1</sup>. (Surface density: 5 mg·cm<sup>-2</sup>).

**Table 6.1** The comparison of electrochemical performances with other CNT-based anodes.

**Table 8.1** Comparison of the specific capacitance of some related materials in the literature.

# Chapter 1. Introduction

## 1.1 Background on the Cu nanomaterials

Nanomaterial is the size range from 1 to 100 nm particle between zero dimension (0D) and three dimensions (3D). Compare with bulk substances, the nanomaterials have various unique properties, due to their small size effect, surface effect and quantum size effect. These properties are reflected in many fields, such as optic, catalytic, biologic, magnetic, mechanic and electronic. Therefore, the nanomaterials with these remarkable properties have been attracted enormous attention in the scientific community, and are widely used for many practical applications (Figure 1.1).<sup>[1-4]</sup> To develop the novel nanomaterials with some special properties, control of their size, morphology, crystalline and compositions are extremely important.<sup>[2, 4]</sup>

Among various nanomaterials, the copper (Cu) based nanoparticles (NPs) as the promising conductive materials are often investigated for conductive ink, and have been numerous interests for next-generation printing electronics, because of their low cost, high conductivity and simple solution-process ability (Figure 1.2).<sup>[5-7]</sup> Compare with silver (Ag), the

weight Cu is less than 2/3 and the price is less than 1/100. However, electrical conductivity and mechanical properties of Cu is very close to that of Ag.<sup>[8]</sup> Therefore, the Cu has been attracted as next-generation Ag replacement.

At ambient conditions, the Cu NPs easily react with oxygen in the air, and then form the natural oxide layer of Cu<sub>2</sub>O and CuO.<sup>[9]</sup> Unlike the highly conductive Cu, these oxide layers acts as the semiconductors generally hinder the electron transport in contact points. Furthermore, due to the high activity, small size and large surface area induce high surface energy; the Cu NPs are easy to be aggregated with each other.<sup>[10]</sup> Therefore, the problems of rapid oxidation and strong aggregation have to be effectively addressed to fabricate high-performance Cu NPs-based electrodes.

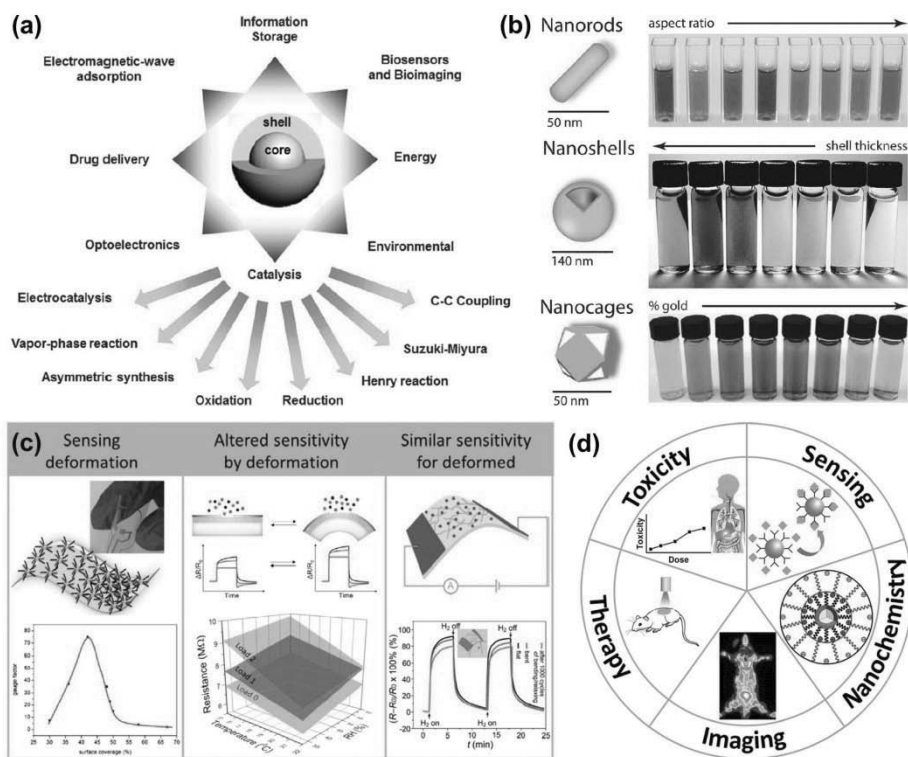


**Figure 1.1** (a) Applications of NPs in the various fields.<sup>[1]</sup> (b) Color change of the various solutions with different size, shape and composition of NPs.<sup>[2]</sup> (c) The NPs-based flexible sensors with three different types.<sup>[3]</sup> (d) Synthesis and treatment of various NPs for biomedical applications.<sup>[4]</sup> (Reprinted with permission from Ref. [1], [2], [3], [4] of Chapter 1. Copyright (a) 2015 Royal Society of Chemistry, (b) 2011 Royal Society of Chemistry, (c) 2013 American Chemistry Society, and (d) 2016 American Chemistry Society)

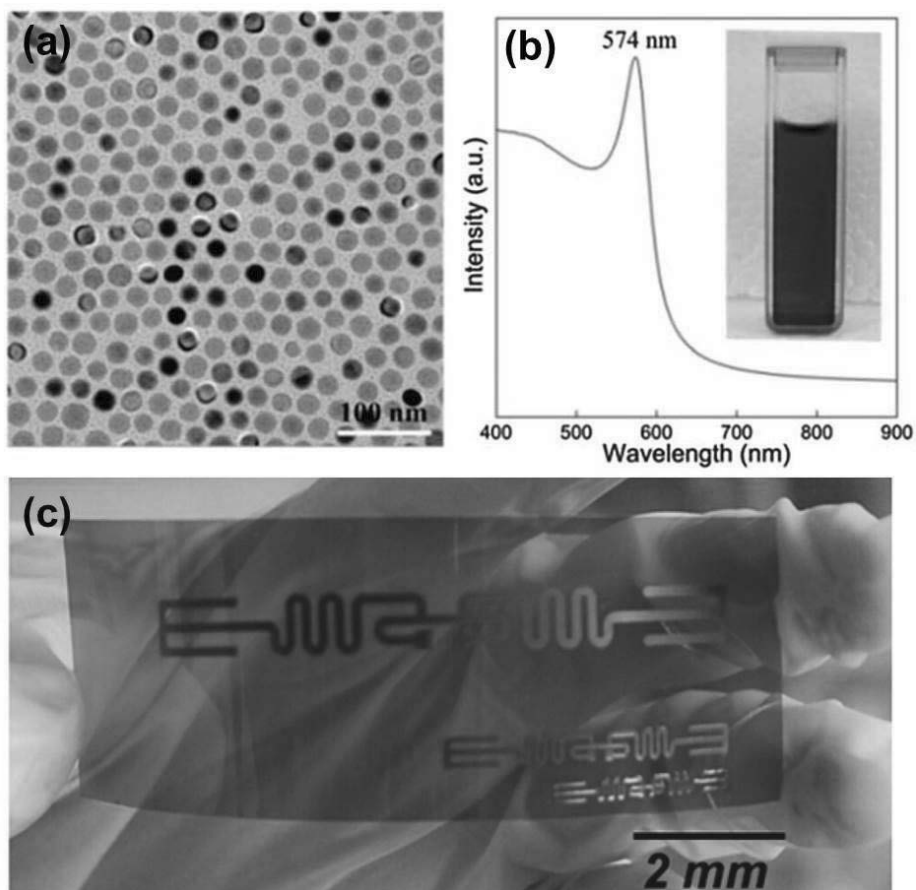


**Figure 1.2** (a) SEM image and (b) UV absorption of the monodisperse Cu NPs.<sup>[6]</sup> (c) Photograph of the Cu NPs-based highly conductive electrode on polyimide substrate.<sup>[7]</sup> (Reprinted with permission from Ref. [6], [7] of Chapter 1. Copyright (a–b) 2013 Royal Society of Chemistry and (c) 2011 American Chemistry Society)

## 1.2 Shape control of Cu nanomaterials

According to control the crystal structure in seed formation, the various shapes of metal nanomaterials are generally synthesized by a simple wet chemical method (Figure 1.2), due to the several merits of low cost fabrication, mild reaction condition and facile NP size control. In the presence of reducing agent and surfactant, the metal seeds are readily formed by their precursor, and grow to polyhedron shapes.<sup>[11]</sup> When the surface energy is sufficiently high and the shape is unstable, the polyhedron NPs may then grow into other shapes, such as nanowires and nanoplates (Figure 1.3).<sup>[11, 12]</sup> On the basis of the special properties from these particular shapes, the NPs can be effectively used for various practical applications, such as catalysis, sensor, energy device, drug delivery, bio-imaging and electronics, etc.

The most representative shapes of Cu NPs are sphere, cube, plate, and wire. Among them, the Cu nanowires (Cu NWs) as one of the most promising conductive materials have been widely investigated for printing electronics and flexible electronics, due to solution-process ability, high conductivity and mechanical stability.<sup>[13, 14]</sup> For the current path, the Cu nanomaterials with general shapes have a lot of resistance in contact points,

because of the natural oxide layer and incomplete metallic bonding. However, the Cu NWs transfer the electrons to dozens of micrometer through conduction band of single NW, which effectively reduce the overall electrode resistance. Moreover, the Cu NWs show a good mechanical stability due to ductility of Cu and structural merit of NW.<sup>[14, 15]</sup> Therefore, the Cu NWs are well suited as the conductive materials for next-generation functional electrodes, such as solution-processable electrode, flexible electrode, foldable electrode, transparent electrode, annealing-free electrode, air-stable electrode and the combined electrode.

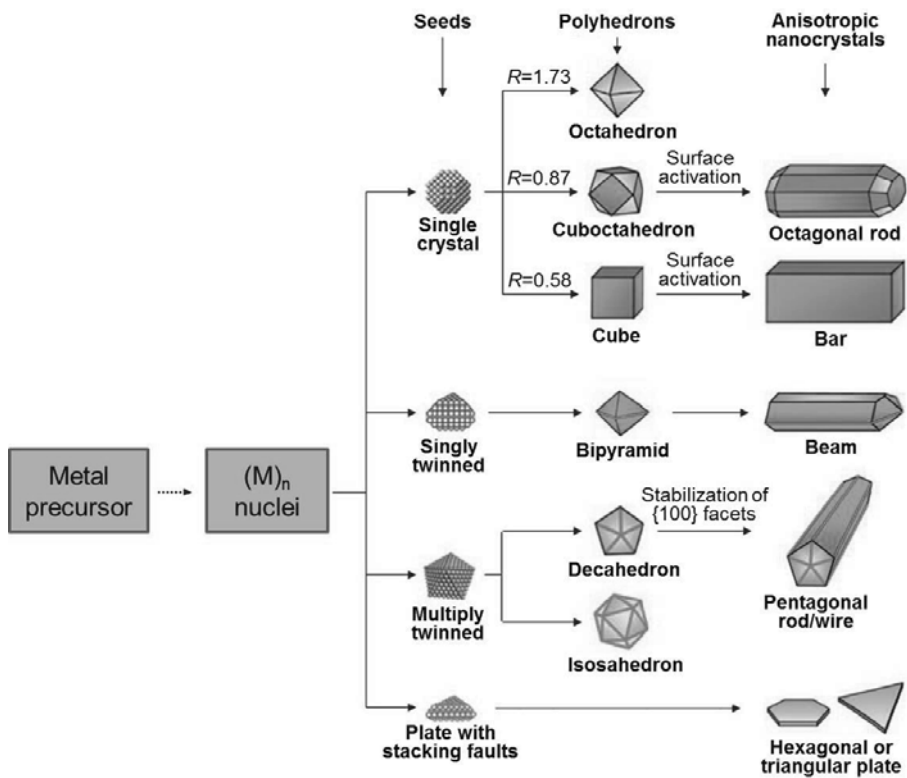


**Figure 1.3** The reaction routes of that leading of the metal nuclei grows to various different shapes of NPs.<sup>[11]</sup> (Reprinted with permission from Ref. [11] of Chapter 1. Copyright 2009 WILEY-VCH Verlag GmbH & Co. KGaA, Weinheim)

## References

- [1] M. B. Gawande, A. Goswami, T. Asefa, H. Guo, A. V. Biradar, D.-L. Peng, R. Zboril, R. S. Varma, *Chem. Soc. Rev.* **2015**, *44*, 7540.
- [2] E. C. Dreaden, A. M. Alkilany, X. Huang, C. J. Murphy, M. A. El-Sayed, *Chem. Soc. Rev.* **2012**, *41*, 2740.
- [3] M. Segev-Bar, H. Haick. *ACS Nano* **2013**, *7*, 8366.
- [4] G. Chen, I. Roy, C. Yang, P. N. Prasad, *Chem. Rev.* **2016**, *116*, 2826.
- [5] Y. Zhang, P. Zhu, G. Li, T. Zhao, X. Fu, R. Sun, F. Zhou, C.-p. Wong, *ACS Appl. Mater. Interfaces* **2014**, *6*, 560.
- [6] H. Guo, X. Liu, Q. Xie, L. Wang, D.-L. Peng, P. S. Brancob, M. B. Gawande, *RSC Adv.* **2013**, *3*, 19812.
- [7] S. Jeong, H. C. Song, W. W. Lee, S. S. Lee, Y. Choi, W. Son, E. D. Kim, C. H. Paik, S. H. Oh, B.-H. Ryu, *Langmuir* **2011**, *27*, 3144.
- [8] A. R. Rathmell, B. J. Wiley, *Adv. Mater.* **2011**, *23*, 4798.
- [9] S. Magdassi, M. Grouchko, A. Kamyshny, *Materials* **2010**, *3*, 4626.
- [10] D. Deng, Y. Jin, Y. Cheng, T. Qi, F. Xiao *ACS Appl. Mater. Interfaces* **2013**, *5*, 3839.
- [11] Y. Xia, Y. Xiong, B. Lim, S. E. Skrabalak, *Angew. Chem. Int. Ed.* **2009**, *48*, 60.
- [12] A. R. Tao, S. Habas, P. Yang *Small* **2008**, *4*, 310.
- [13] J. Song, J. Li, J. Xu, H. Zeng, *Nano Lett.* **2014**, *14*, 6298.
- [14] Z. Yin, C. Lee, S. Cho, J. Yoo, Y. Piao, Y. S. Kim, *Small* **2014**, *10*, 5047.
- [15] S. Bhanushali, P. Ghosh, A. Ganesh, W. Cheng, *Small* **2015**, *11*, 1232.

# **Chapter 2 Literature and Dissertation Overview**

## **2.1 Synthetic methods of Cu NWs and their nanocomposites**

The preparation of Cu NWs and their nanocomposites are reported with several methods, such as vapor deposition, template, electric field directed self-assembly and micelle/reverse micelle.<sup>[1-4]</sup> These methods have their own advantages and disadvantages. Vapor deposition method is the most mature technology, because the process condition is easy to control, and the synthesized Cu NWs have a very high purity. Recently, Cu NW-graphene core-shell nanocomposites were firstly synthesized by a low-temperature PECVD process under 400 °C, and applied for transparent conductive electrode with excellent opto-electrical performance.<sup>[5]</sup> However, high cost manufacturing process and low yield of Cu NWs with uneven size distribution still the critical problems that must be addressed before wide application. The template-assisted method can be efficient to control the shapes of nanomaterials, and the structural integrity is quite higher than

other methods. Furthermore, this method has a high practical value, because the NWs have a high yields with an excellent dispersibility and can be large-scale synthesized. However, separation from the template is an extra and necessary process in this method, which is quite troublesome and easy to damage the prepared NWs. Additionally, since the size of the template is limited to a certain range, it is difficult to change the size of Cu NWs at a large scale. On the contrary, the electric field directed self-assembly method is suitable for use in an all solid state environment without any template. It is easy to control the growth direction of Cu NWs with high purity. Unfortunately, with the same as vapor deposition method, low yield and uneven size of Cu NWs are still unsolved issues.

Micelle/reverse micelle method as a wet chemical synthesis often used for the preparation of Cu NWs and their nanocomposites.<sup>[6, 7]</sup> In general, the precursors, reactants and surfactants are participated in the micelle/reverse micelle method. Among them, the surfactant act as an important factor to mainly control the size and morphology of prepared nanoparticles. Normally, micelle/reverse micelle was made by opposite polarity of solvent and surfactant, which is oil in water (o/w) or water in oil (w/o). These micelles as the micro-cages restrict or provide the growth of nanoparticles. Certainly, the special surfactants can support to grow in part of the crystal

face of nanoparticles (NPs), then formation of NWs and nanocubes. In addition, the activity and chemical stability of NPs are also often associated with surfactants, because the surfactants as the capping molecules adsorb in the NPs surface and reduce the surface energy. Therefore, the types and concentration of surfactants in the reaction are extremely important.

Recently, various studies have shown that halide ions contribute to the growth of Cu NP in one direction, then formation of the Cu NWs.<sup>[8, 9]</sup> The Cu NWs and their composites synthesized by this method have a good interfacial property, and a narrow size distribution with high stabilities. Furthermore, the overall reaction conditions are mild even a large-scale synthesis.<sup>[10]</sup> Therefore, the production cost is significantly lower than other methods; also, it is expected to achieve the industrialization.

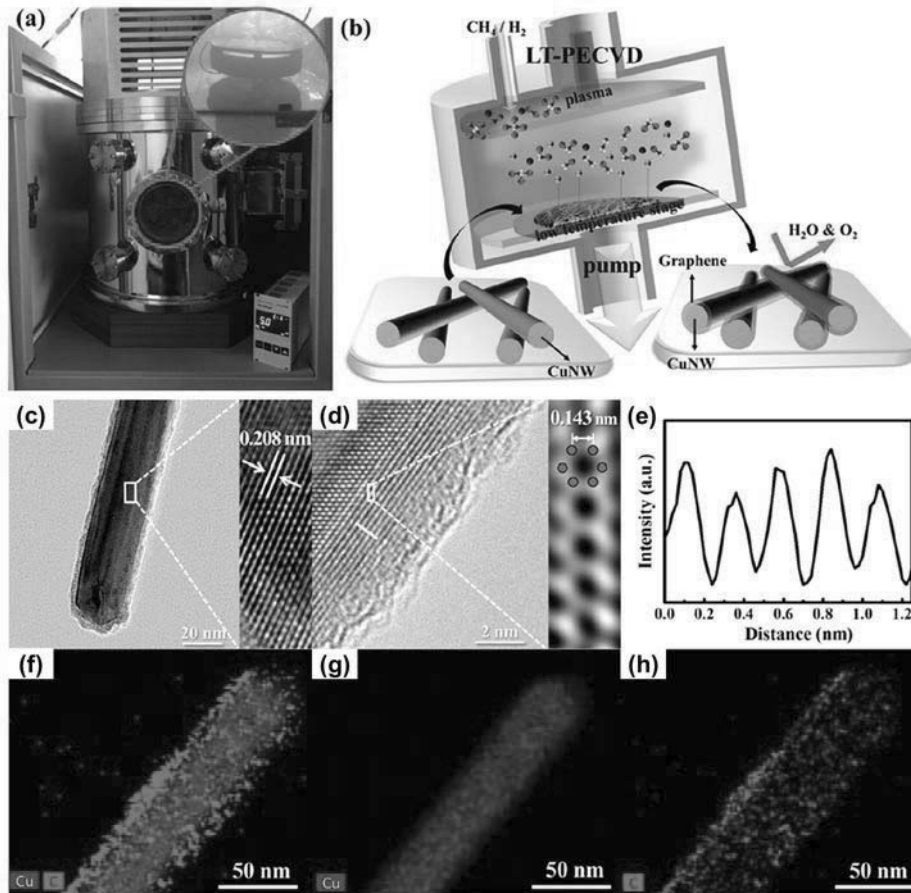


**Figure 2.1** (a) Photograph of (b) schematic image of the low-temperature PECVD for preparation of CuNW-Graphene core-shell nanostructure with a radio frequency plasma system. (c–e) HR-TEM images and line intensity profile of the CuNW-Graphene core-shell nanostructure. (f–h) EDS analysis of Cu and C elements for demonstration of the CuNW-Graphene core-shell nanostructure. (Reprinted with permission from Ref. [5] of Chapter 2. Copyright 2015 American Chemistry Society)

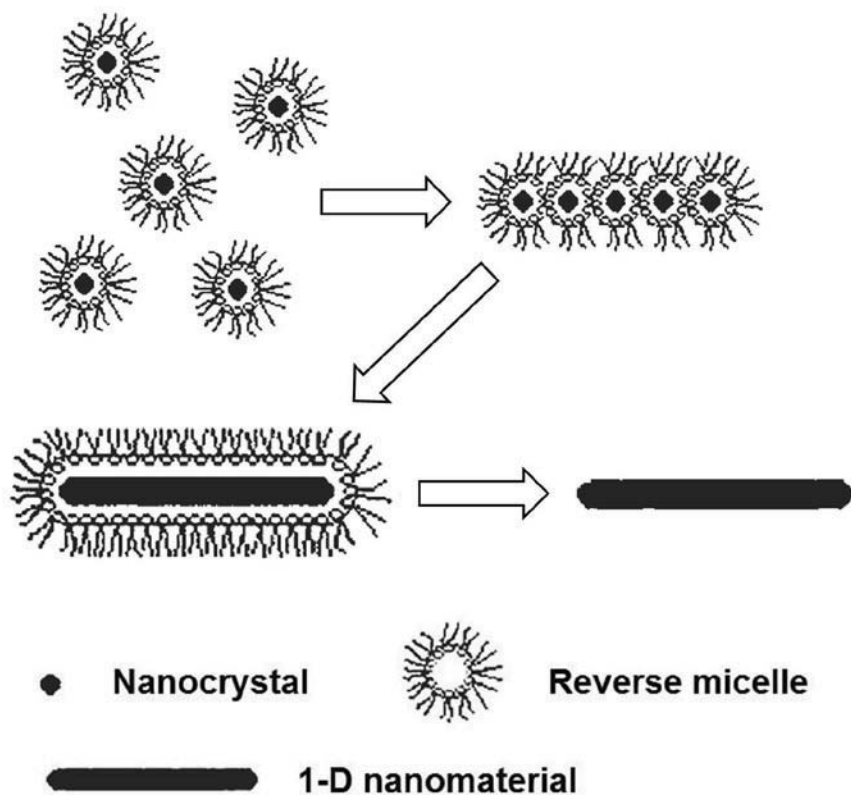


**Figure 2.2** Synthetic mechanism for the growth of Cu NWs in reverse micelle system.<sup>[6]</sup> (Reprinted with permission from Ref. [6] of Chapter 2. Copyright 2004 Royal Society of Chemistry)

## **2.2 Networking of Cu NWs for conductive electrode**

As well known, the Cu NWs typically preserved and dispersed in a solvent to use for conductive ink. Although the intrinsic dispersibility of Cu NWs is difficult to be directly applicable for coating or deposition due to the easy aggregation and high molecular mass of Cu NWs, it can be appropriately improved with the assistance of surfactants, such as thiol, amine and acid.<sup>[11-13]</sup> However, the excessive surfactant as a residue hinders the electron transfer between Cu NWs, which the conductivity of electrode. Therefore, the choice of suitable surfactants is extremely critical for both NWs dispersibility and ink application.

In addition to Cu NWs surface treatment, another important factor for ink application is the solvent. The compatibility, polarity, and viscosity of solvent are strongly related to the application of Cu NWs, involving dispersion, coating and manufacturing. Also, the non-toxic non-corrosive solvents have to be used, taking into account the practical applications. Furthermore, various deposition and coating methods are often used to prepare ink-based electrodes, which is a necessary process. Spin coating,

spray coating, meyer rod coating, dip coating, vacuum filtration, convective assembly, and meniscus-dragging deposition methods have been reported to fabricate NWs-based electrodes.<sup>[14-20]</sup> However, due to the limitations of the Cu NWs dispersibility and solvent properties, the experimental techniques and conditional regulation of these methods are very harsh. Therefore, the synthesis of Cu NWs, selection of solvents, choice of coating methods must be suitable for each other with high compatibility.

After deposition, the Cu NWs are in contact with each other for electron transportation. In general, the connection of Cu NWs can be divided into non-contact type, contact type and percolation type.<sup>[21, 22]</sup> The non-contact type is caused by the surface oxidation of Cu NWs or residual surfactants, which functioned as high contact resistance to reduce the electrode conductivity. Therefore, the electrodes with this non-contact type have a very low conductivity. Obviously, the conductivity of the electrode increases with the removal of residues of oxide layer and surfactants. Recently, the acidic solvents and reducing agents were used to remove the oxide layer on Cu NWs surface for enhance the conductivity of electrodes.<sup>[21, 23]</sup> However, the contact resistance is still present due to the small contact area in Cu NWs junction. Furthermore, the secondary oxidation is also a problem to be solved. Therefore, many research groups

use the percolation type of Cu NWs to make electrodes. The basic principle of percolation type is that the individual Cu NWs are welded by the metallic bonding through improvement of the kinetic energy of electrons from sufficient external energy. Many special technologies and instruments also researched for the Cu NWs percolation, such as laser welding, intense-pulsed-light irradiation, thermal sintering and solvent-dipped welding method.<sup>[24-27]</sup>

Through the connection of Cu NWs, the high conductive films with special properties are prepared for various functional conductive electrodes and applicable for many practical applications, such as flexible transparent conductive electrode (FTCE), wearable electrode and 3D current-collecting electrode.

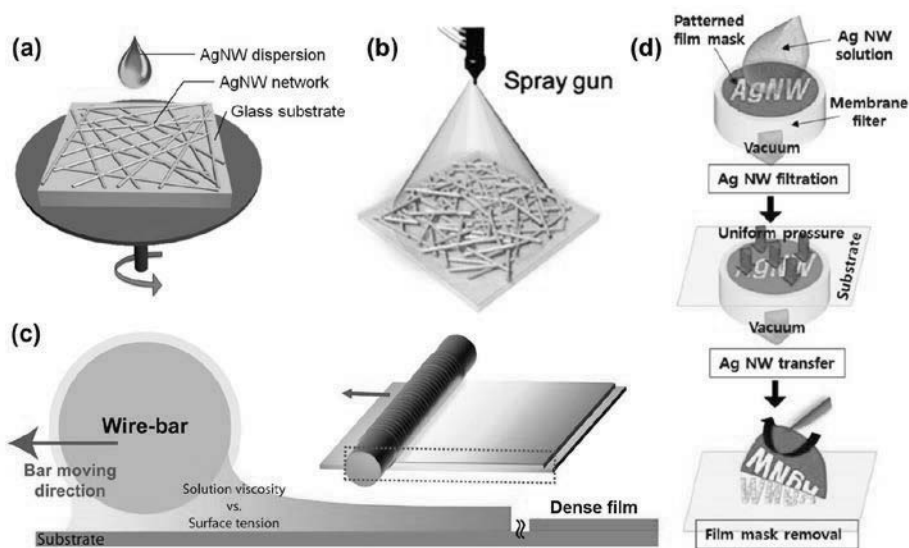


**Figure 2.3** Various coating method for the fabrication of NWs-based electrodes. (a) Spin coating,<sup>[14]</sup> (b) spray coating,<sup>[15]</sup> (c) meyer rod coating,<sup>[16]</sup> and (d) vacuum filtration.<sup>[18]</sup> (Reprinted with permission from Ref. [14], [15], [16], [18] of Chapter 2. Copyright (a) 2013 Optical Society of America, (b) 2016 Royal Society of Chemistry, (c) 2015 WILEY-VCH Verlag GmbH & Co. KGaA, Weinheim, and (d) 2012 Royal Society of Chemistry)

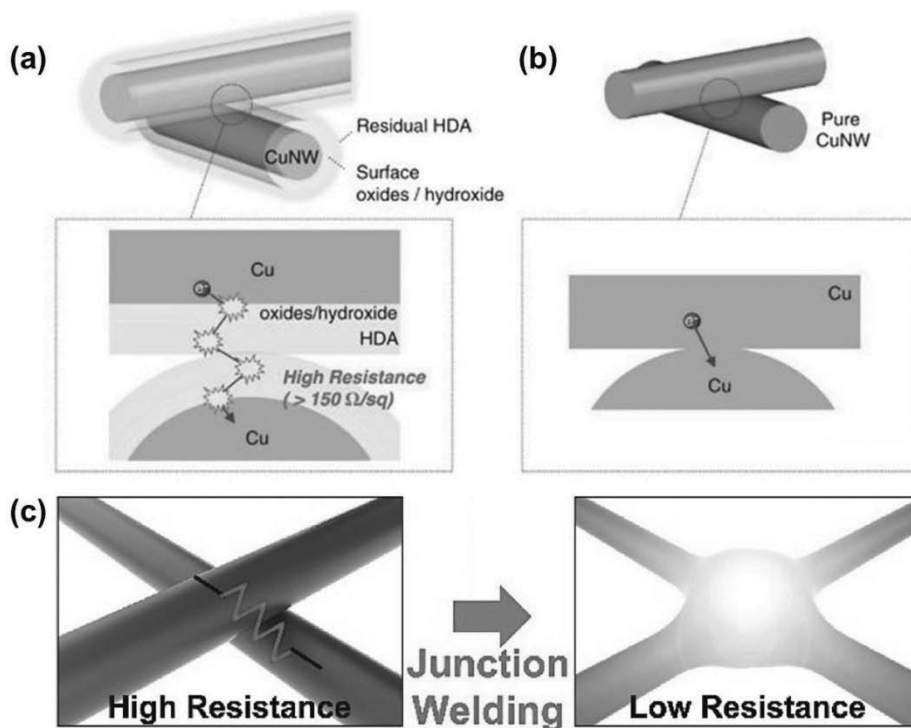


**Figure 2.4** Various networking types of the Cu NWs with different resistance. (a) non-contact type,<sup>[21]</sup> (b) contact type,<sup>[21]</sup> and (c) percolation type.<sup>[22]</sup> (Reprinted with permission from Ref. [21], [22] of Chapter 2. Copyright (a, b) 2014 Nature Publishing Group, and (c) 2017 WILEY-VCH Verlag GmbH & Co. KGaA, Weinheim)

## 2.3 Dissertation overview

This graduation thesis consists of 7 chapters, and the contents are mainly focused on the synthesis and applications of the Cu NWs and their nanocomposites. The synthetic methods, characteristics, post-process treatment and various applications of Cu NWs and their nanocomposites are introduced in chapter 2. In addition, a detailed explanation for research backgrounds, public demands and technical problems of FTCE, wearable electrode and 3D current-collecting electrode with Cu NWs and their nanocomposites are provided in "introduction part" of several following chapters.

In chapter 3, we introduce a whole manufacturing process of the curved Cu NWs (CCNs) based FTCE with all solution processes, including synthesis, coating and networking. The CCNs with high purity and good quality are designed and synthesized by a binary polyol co-reduction method. In this reaction, volume ratio and reaction time are the significant factors for the successful synthesis. These NWs have an average 50 nm in width and 25–40  $\mu\text{m}$  range in length with curved structure and high softness. Furthermore, a meniscus-dragging deposition (MDD) method is used to uniformly coat the well-dispersed CCNs on the glass or PET

substrate with a simple process. The optoelectrical property of the CCNs thin films is precisely controlled by applying the MDD method. The FTCE is fabricated by networking of CCNs using solvent-dipped annealing method with vacuum-free, transfer-free, and low-temperature conditions. To remove the natural oxide layer, the CCNs thin films are reduced by glycerol or  $\text{NaBH}_4$  solution at low temperature. As a highly robust FTCE, the CCNs thin film exhibits excellent optoelectrical performance ( $T = 86.62\%$ ,  $R_s = 99.14 \Omega \cdot \square^{-1}$ ), flexibility, and durability ( $R/R_0 < 1.05$  at 2000 bending, 5 mm of bending radius).

In chapter 4, we introduce that CCN-based high-performance FTCEs were fabricated via a fully solution-processed approach, involving synthesis, coating, patterning, welding, and transfer. Each step involved an innovative technique for completing the all-solution processes. The high-quality and well-dispersed CCNs were synthesized using a multi-polyol method through the synergistic effect of specific polyol reduction. To precisely control the optoelectrical properties of the FTCEs, the CCNs were uniformly coated on a polyimide (PI) substrate via a simple MDD method by tuning several coating parameters. We also employed polyurethane (PU)-stamped patterning method to effectively produce  $20 \mu\text{m}$  patterns on CCN thin films. The CCN thin films exhibited high electrical performance,

which is attributed to the deeply percolated CCN network formed via a solvent-dipped welding method. Finally, the CCN thin films on the PI substrate were partially embedded and transferred to the PU matrix to reduce their surface roughness. Through consecutive processes involving the proposed methods, a highly percolated CCN thin film on the PU matrix exhibited high optoelectrical performance ( $R_s = 53.48 \Omega \cdot \square^{-1}$  at  $T = 85.71\%$ ), excellent mechanical properties ( $R/R_0 < 1.10$  after the 10<sup>th</sup> repetition of tape peeling or 1,000 bending cycles), and a low root-mean-square surface roughness ( $R_{rms} = 14.36$  nm).

In chapter 5, we introduce a straightforward solvothermal method to prepare a flexible conductive material that contains reduced graphene oxide (RGO) nanosheets bridging oriented Cu NWs. The GO-assistance route can successfully meet the industrial manufacturing criteria and help the composite films maintain high conductivity and durable flexibility without any extra treatment, such as annealing or acid processes. The composite film exhibits a high electrical performance ( $0.808 \Omega \cdot \square^{-1}$ ) without considerable change over 30 days under ambient conditions. Moreover, the Cu NW-RGO composites can be deposited on polyester cloth as a light-weight wearable electrode with high durability and simple processability, and are very promising for a wide variety of electronic devices.

In chapter 6, a novel lightweight three-dimensional (3D) composite anode for a fast-charging/discharging Li-ion battery (LIB) is introduced, which was fabricated entirely using one-dimensional (1D) nanomaterials of Cu NWs and multi-walled Carbon nanotubes (MWCNTs). Because of their excellent electrical conductivity, high-aspect ratio structures, and large surface areas of these nanomaterials, the CuNW-MWCNT composite (CNMC) with 3D structure provides significant advantages regarding the transport pathways for both electrons and ions. As an advanced binder-free anode, a CNMC film with a controllable thickness ( $\sim 600 \mu\text{m}$ ) exhibited a considerably low sheet resistance, and internal cell resistance. Furthermore, the random Cu NW network with 3D structure acting as a rigid framework not only prevented MWCNT shrinkage and expansion due to aggregation and swelling but also minimized the effect of volume change during the charge/discharge process. Both half cell and full cell of LIBs with the CNMC anode exhibited high specific capacities and Coulombic efficiencies, even at a high current. More importantly, we for the first time overcame the limitation of MWCNTs as anode materials for fast-charging/discharging LIBs (both half cells and full cells) by employing Cu NWs, and the resulting anode can be applied to flexible LIBs. This innovative anode structure can lead to the development of ultrafast chargeable LIBs for

electric vehicles.

Finally, the chapter 7 summarizes the overall research results of the synthesis and applications of Cu NWs and their nanocomposites. Furthermore, as the additional contents of appendix, we introduce the rose rock-shaped  $\text{Cu}_2\text{O}$ -RGO nanocomposites for high-performance supercapacitors in chapter 8.

## References

- [1] C. Kim, W. Gu, M. Briceno, I. M. Robertson, H. Choi, K. Kim, *Adv. Mater.* **2008**, *20*, 1859.
- [2] C. F. Monson, A. T. Woolley, *Nano Lett.* **2003**, *3*, 359.
- [3] J. Zhang, J. Sun, W. Liu, S. Shi, H. Sun, J. Guo, *Nanotechnology* **2005**, *16*, 2030.
- [4] M. Jin, G. He, H. Zhang, J. Zeng, Z. Xie, Y. Xia, *Angew. Chem. Int. Ed.* **2011**, *50*, 10560.
- [5] Y. Ahn, Y. Jeong, D. Lee, Y. Lee, *ACS Nano* **2015**, *9*, 3125.
- [6] J. Zhang, B. Han, D. Liu, J. Chen, Zh. Liu, T. Mu, R. Zhang, G. Yang, *Phys. Chem. Chem. Phys.* **2004**, *6*, 2391.
- [7] Y. Chang, M. L. Lye, H. C. Zeng, *Langmuir* **2005**, *21*, 3746.
- [8] X. Huang, Y. Chen, C. Chiu, H. Zhang, Y. Xu, X. Duan, Y. Huang, *Nanoscale* **2013**, *5*, 6284.
- [9] H. Z. Guo, Y. Z. Chen, H. M. Ping, J. R. Jin, D.-L. Peng, *Nanoscale* **2013**, *5*, 2394.
- [10] S. Li, Y. Chen, L. Huang, D. Pan, *Inorg. Chem.* **2014**, *53*, 4440.
- [11] E. Ye, S. Zhang, S. Liu, M. Han, *Chem. Eur. J.* **2011**, *17*, 3074.
- [12] H.-J. Yang, S.-Y. He, H.-Y. Tuan, *Langmuir* **2014**, *30*, 602.
- [13] H. Guo, N. Lin, Y. Chen, Z. Wang, Q. Xie, T. Zheng, N. Gao, S. Li, J. Kang, D. Cai, D.-L. Peng, *Sci. Rep.* **2013**, *3*, 2323.
- [14] S. Xie, Z. Ouyang, B. Jia, M. Gu, *Opt. Express* **2013**, *21*, A355..
- [15] H. S. Kang, J. Choi, W. Cho, H. Lee, D. Lee, D. G. Lee, H.-T. Kim, *J. Mater. Chem. C* **2016**, *4*, 9834.
- [16] W.-J. Lee, W.-T. Park, S. Park, S. Sung, Y.-Y. Noh, M.-H. Yoon, *Adv. Mater.* **2015**, *27*, 5043.
- [17] E. Y. Jang, T. J. Kang, H. W. Im, D. W. Kim, Y. H. Kim, *Small* **2008**, *4*, 2255.

- [18] J. Lee, P. Lee, H. Lee, D. Lee, S. S. Lee, S. H. Ko, *Nanoscale* **2012**, *4*, 6408.
- [19] S. K. Duan, Q. L. Niu, J. F. Wei, J. B. He, Y. A. Yin, Y. Zhang, *Phys. Chem. Chem. Phys.* **2015**, *17*, 8106.
- [20] Y. Ko, S. K. Song, N. H. Kim, S. T. Chang, *Langmuir* **2016**, *32*, 366.
- [21] Y. Won, A. Kim, D. Lee, W. Yang, K. Woo, S. Jeong, J. Moon, *NPG Asia Mater.* **2014**, *6*, e105.
- [22] J. H. Park, S. Han, D. Kim, B. K. You, D. J. Joe, S. Hong, J. Seo, J. Kwon, C. K. Jeong, H.-J. Park, T.-S. Kim, S. H. Ko, K. J. Lee, *Adv. Funct. Mater.* **2017**, *27*, 1701138.
- [23] C. R. Chu, C. Lee, J. Koo, H. M. Lee, *Nano Res.* **2016**, *9*, 2162.
- [24] S. Han, S. Hong, J. Ham, J. Yeo, J. Lee, B. Kang, P. Lee, J. Kwon, S. S. Lee, M.-Y. Yang, S. H. Ko, *Adv. Mater.* **2014**, *26*, 5808.
- [25] S. Ding, J. Jiu, Y. Tian, T. Sugahara, S. Nagao, K. Suganuma, *Phys. Chem. Chem. Phys.* **2015**, *17*, 31110.
- [26] Z. Zhong, H. Lee, D. Kang, S. Kwon, Y.-M. Choi, I. Kim, K.-Y. Kim, Y. Lee, K. Woo, J. Moon, *ACS Nano* **2016**, *10*, 7847.
- [27] D. Zhang, R. Wang, M. Wen, D. Weng, X. Cui, J. Sun, H. Li, Y. Lu, *J. Am. Chem. Soc.* **2012**, *134*, 14283.

# **Chapter 3. Novel Synthesis, Coating and Networking of Curved Copper Nanowires for Flexible Transparent Conductive Electrodes**

## **3.1 Introduction**

Flexible transparent conductive electrode (FTCE) is an essential and crucial component in next generational electronic devices with high flexibility, conductivity and transparency.<sup>[1]</sup> For advanced flexible devices, such as touch screen, e-books, organic light-emitting diodes (OLED), solar cells, and liquid-crystal display (LCD) panels, various transparent electrodes with high flexibility have been researched.<sup>[2, 3]</sup> As a traditional transparent electrode, indium tin oxide (ITO) is utilized the most in devices due to their outstanding opto-electrical performance.<sup>[1, 4, 5]</sup> However, as a ceramic material, the brittleness of ITO is a critical limitation to use for flexible devices.<sup>[4]</sup> Furthermore, the price of ITO film is too high due to the insufficient indium sources and the vapor-phase sputtering process.<sup>[4, 5]</sup>

Recently, solution-processable single-walled carbon nanotube (SWCNT), reduced graphene oxide (RGO), and metal nanowires thin films have been extensively explored as alternatives for ITO and application for flexible devices, due to their high flexibility and opto-electrical property.<sup>[6-9]</sup> As substituted nanomaterials, solution-processable SWCNT and RGO thin films are feasible to use for FTCE. Although the SWCNT and RGO have high mechanical properties, the relatively poor opto-electrical performance is still a problem that must be addressed before wide application, because of their high contact resistance.<sup>[7, 8]</sup> Metal nanowires randomly that have been deposited on the flexible transparent substrate exhibited high flexibility, superior conductivity, and excellent transparency due to their structural advantages in nanowire shape.<sup>[10]</sup> In particular, the opto-electrical performance of silver nanowires (Ag NWs) thin film is close to that of ITO electrode.<sup>[9]</sup> However, as a noble metal, the scarcity and high price of Ag are also critical issues for wide application. In comparison, the electrical conductivity of copper (Cu) is very close to that of Ag with a significantly cheaper price.<sup>[10]</sup> Unfortunately, the problems of rapid oxidation, strong aggregation, and high sintering temperature by large surface area and high surface energy, still blocked the Cu NWs to be widely used for FTCE on various plastic substrates, such as polyethylene terephthalate (PET).<sup>[11]</sup> In

addition, the electrical performance of general metal nanowires thin films are easy to be degenerated by tensile strain from flexible substrate bending, because of the fixed rigid structural networking of linear nanowires.

Recently, the curved and ring structural Cu NWs as impurities were synthesized by the N-methyl-2-pyrrolidone/water system through a solvothermal method.<sup>[12]</sup> Although the self-bendable structure of nanowires induce high ductility and good softness, the low-purity and poor-quality limit their applications.<sup>[12]</sup> Furthermore, general Cu NWs have rapid oxidation, strong aggregation, and high sintering temperature that must be addressed to achieve high-performance and low-cost FTCE.

Herein, we firstly report the whole manufacturing process of curved Cu NWs (CCNs) based FTCE. We designed the processes as follows; 1) CCNs with high purity and good quality were synthesized by a binary polyol co-reduction method, which enhances the flexibility and durability of FTCE. 2) A meniscus-dragging deposition (MDD) method was used to simply, directly and uniformly coat well-dispersed CCNs on the glass or PET substrate with vacuum-free and transfer-free conditions. 3) Networking of CCNs was achieved by a solvent-dipped annealing method to fabricate the FTCE at the low temperature of 50 °C. The whole experiments were based on solution processes, involving synthesis, coating and networking.

## **3.2 Experimental section**

### **3.2.1 CCNs preparation**

In a typical procedure, 2 mmol of CuCl, 0.3 mmol of NH<sub>4</sub>Cl, and 6 mmol of oleylamine were dissolved in mixed solution of 20 ml EG and 10 ml GC in a 100 ml round-bottom flask with strong magnetic stirring. The reaction temperature was then raised to 110 °C and kept 15 min for fully forming Cu<sup>+</sup>-amine complex. Finally, the reaction temperature was heated up to 208 °C (9 °C·min<sup>-1</sup> of heating rate), refluxed and kept for 20 min. After cooling down to room temperature using rapid cold water quenching, the red brown CCNs precipitates were washed by n-hexane and ethanol. When n-hexane and ethanol were added, the red brown precipitates were suspended to the upper layer by n-hexane. The supernatant was isolated to conical tube and centrifuged for 3 min in 3,500 rpm. This step was repeated 3 times before the CCNs were re-dispersed and preserved in n-hexane.

### **3.2.2 Linear Cu NWs preparation**

2 mmol of CuCl, 0.3 mmol of NH<sub>4</sub>Cl, and 6 mmol of oleylamine were

dissolved in 30 ml ethylene glycol in a 100 ml round-bottom flask with strong magnetic stirring. As the CCNs synthesis, Cu<sup>+</sup>-amine complex was formed in 110 °C. After then, the reaction temperature was heated up to 198 °C (9 °C·min<sup>-1</sup> of heating rate), refluxed and kept for 20 min. After quenching, the Cu NWs were washed and re-dispersed by n-hexane.

### **3.2.3 CCNs films fabrication**

The slide glasses (25 × 25 mm, Fisher Scientific, USA) employed as the coating substrate and deposition plate were cleaned by piranha solution for 30 min and washed by ethanol. In addition, the commercial PET films (SKC Film Co., Korea) (70 × 75 mm) were also used as a flexible coating substrate for FTCE. The synthesized CCNs were dispersed in hexane with a concentration of 3 mg·mL<sup>-1</sup> to use a coating solution. The 20 μL CCNs solution was injected into the wedge between the deposition plate and coating substrate at a deposition angle of  $\theta = 30^\circ$ . The deposition plate was pushed with a linear alternative back-and-forth movement by a motorized stage (AL1-1515-3S, Micro Motion Technology, Valley Center, USA) at a constant velocity of 20 mm·s<sup>-1</sup> to deposit the CCNs on the coating substrates with various deposition numbers. The above-mentioned

deposition process was repeated on the 90° rotated pre-coated substrates. After completely drying, the CCNs films on the glass or PET substrate were covered by GC solvent at 140 °C and 2 mg·mL<sup>-1</sup> NaBH<sub>4</sub> solution at 50 °C, respectively, for 3 min rinsed with ethanol and acetone.

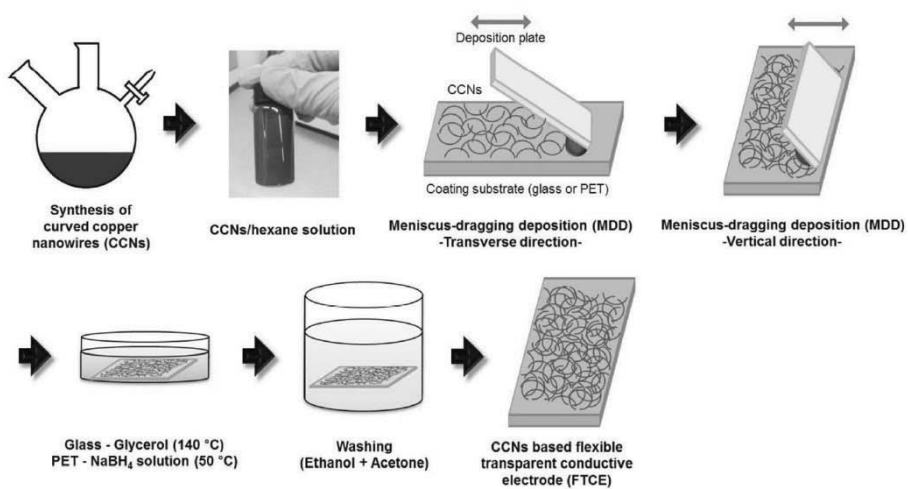
### **3.2.4 CCNs and films Characterization**

The synthesized CCNs were characterized by X-ray diffraction measurements (Bruker D8 DISCOVER), ultraviolet-visible spectroscopy (PerkinElmer Lambda 35), high-resolution transmission electron microscope (JEOL JEM-2100F) and scanning electron microscope (Hitachi S-4800 FE-SEM). Optical microscopy images of the CCNs thin films were obtained by digital cameras (Olympus utv1x-2). The sheet resistances of the CCNs films were characterized by a Keithley 2612A System of source meter with a four-point probe configuration. The transmittance of the CCNs thin films were measured by UV-vis-NIR spectrophotometry (V-670, Jasco), which was calculated based on the reference of an identical glass or PET substrate. Therefore, the intrinsic transmittances of the glass and PET substrates were not included in measured transmittance.

## 3.3 Results and discussion

### 3.3.1 Overview of whole process

As illustrate in Scheme 3.1, the combination of three steps, such as synthesis, coating and networking, is very important for whole manufacturing processes. The CCNs were synthesized within the 1 h reaction time without any expensive catalyst and then well-dispersed in the hexane solution. The transparency and conductivity of the CCNs thin films on glass or PET substrate were precisely controlled in wide ranges by applying the MDD method.<sup>[4, 13]</sup> For proper conductivity, the CCNs thin films were dipped and annealed at a low temperature of 140 °C in glycerol (GC) for a glass substrate or 50 °C in NaBH<sub>4</sub> solution for a PET substrate to eliminate the oxide layer. Then, the CCNs directly connected with each other and formed a conducting network for electron transfer routes. As a highly robust FTCE, the CCNs thin film on PET substrate exhibited high transparency (86.62 % at 550 nm), low sheet resistance (99.14 Ω·□<sup>-1</sup>), excellent flexibility and durability ( $R/R_0 < 1.05$  at 2000 bending, 5 mm of bending radius).



**Scheme 3.1** Fabrication of curved copper nanowires (CCNs)-based flexible transparent conductive electrode (FTCE), including synthesis, coating, and networking.

### 3.3.2 Binary polyol co-reduction method

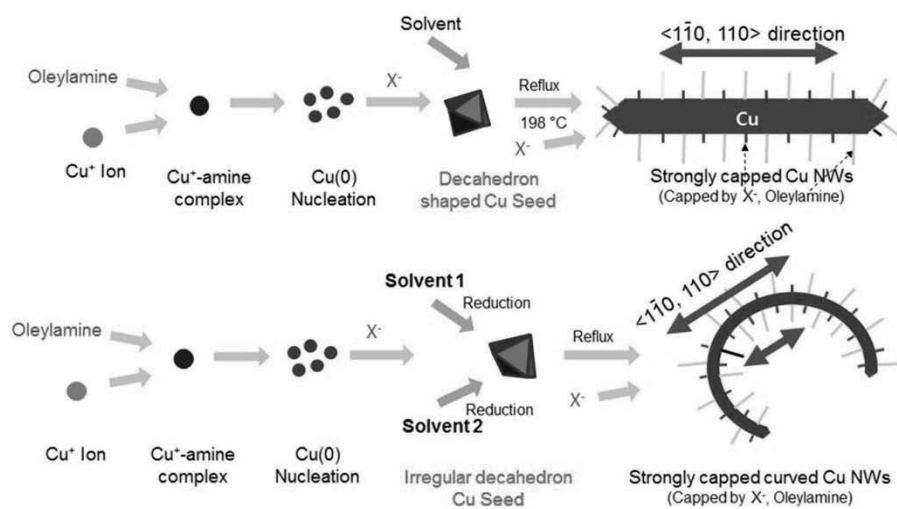
Binary polyol solvents of ethylene glycol (EG) and glycerol (GC) were designed to successfully synthesize the CCNs, which is modified by a salt-assisted polyol reduction method.<sup>[10]</sup> In the experimental condition, the volume ratio of binary solvents is a significant factor in forming the curved structure. In the presence of salt ion, a single solvent of EG or GC reduces the  $\text{Cu}^+$ -amine ions to form decahedron shaped seeds and grow into nanowires at high temperature.<sup>[10, 14, 15]</sup> However, under the binary polyol solvents of EG and GC, the  $\text{Cu}^+$ -amine ions are easily reduced to the irregular decahedral multiply twinned particles, because the shape strongly depended on the co-reduction effect and reduction potential gap of them.<sup>[16, 17]</sup> In addition, this gap is gradually changed by increasing the reaction temperature. Therefore, these irregular decahedral Cu seeds induce the twinning planes twisted along the elliptical direction with partial line defects in the growth. As well known, the deformation of a material strongly related to atomic movement of dislocation, such as line defects. Millions of these line defects result for plastic formation of NW due to rolling and extruding operation, further induced the seeds growth to curved nanowire shape.<sup>[12]</sup> In general, the initial shape of crystal seeds and atomic

arrangement have strongly effect on the final shape of nanowires, which is caused by reaction condition, such as reduction potential.<sup>[16, 18]</sup>

Also, by controlling the volume ratio of EG and GC, differently shaped Cu NWs were clearly observed. Figure 3.1 shows the effects of volume ratio variation of the binary polyol solvents with fixed total volume as 30 ml. In the case of EG,  $\text{Cu}^+$ -amine ions were reduced neatly, and the atoms arranged into symmetrical pentagonal seeds at the same reduction surrounding of the single solvent.<sup>[10, 19]</sup> In the effect of  $\text{Cl}^-$  ion, the relatively stable  $\{100\}$  plane exposed on the surface, and the seed elongated in the  $[1\bar{1}0]$  direction produces only the straight Cu NW shape.<sup>[19, 20, 21]</sup> (Figure 3.1a) In the optimized condition, under the influence of co-reduction effect of 20 ml EG and 10 ml GC, Cu nanocrystals reduced to form the irregular decahedron shaped Cu seeds.<sup>[16]</sup> These structures elongated in the  $[1\bar{1}0]$  direction to form curved wires or elliptical wires with randomly twisted twinning planes and partially line defects by growing process.<sup>[12, 18]</sup> (Scheme 3.2 and Figure 3.1b) Additionally, the products tend to be affected by the high concentration of GC. Under the 10 ml EG and 20 ml GC of binary polyol solvents, GC assumes the main role in the reaction and collapses the curved structure that has a much stronger reduction potential. (Figure 3.1c) Figure 3.1d shows the linear Cu NWs synthesized in the 30 ml

EG, which is the same mechanism with GC solvent.<sup>[10]</sup> Certainly, 30 ml of EG and 30ml of GC make different sizes of Cu NWs due to the noticeable reduction potential difference. This potential gap induced that the Cu seed formed an irregular decahedral shape in the interface reaction in mixed solution, further growth to curved shape. According to the additive 10ml GC in this system, the reaction temperature was slightly enhanced to 208 °C.

Besides the volume ratio of the solvents, the reaction time is another critical factor to synthesize the CCNs. Figure 3.2 clearly shows the morphology change by the reaction time. On the basis of the analysis, the Cu NWs were bended at the first time of reaction with their low diameter, due to EG and GC effect. As well known, through the passage of reaction time, the Cu NWs grows in three dimensions with different growth speed, because of the crystal effect and capping agent.<sup>[10]</sup> The curved structure strongly depends on the crystallinity of individual crystal plane and wire width. In addition, the CCN shape is an intermediated product formed by growth of an unstable seed. When the mixed solvents reached to the stable temperature and time, the Cu atoms were overlaid and arranged in the curved surface to reduce their surface energy for steady state, which is a growing process of NW. As a result, the rigidity of NWs is enhanced and the curvature of CCNs is reduced after 20 min with increasing of NW width.



**Scheme 3.2** Mechanism comparison of the synthesis of linear shape and curved shape of Cu NWs.

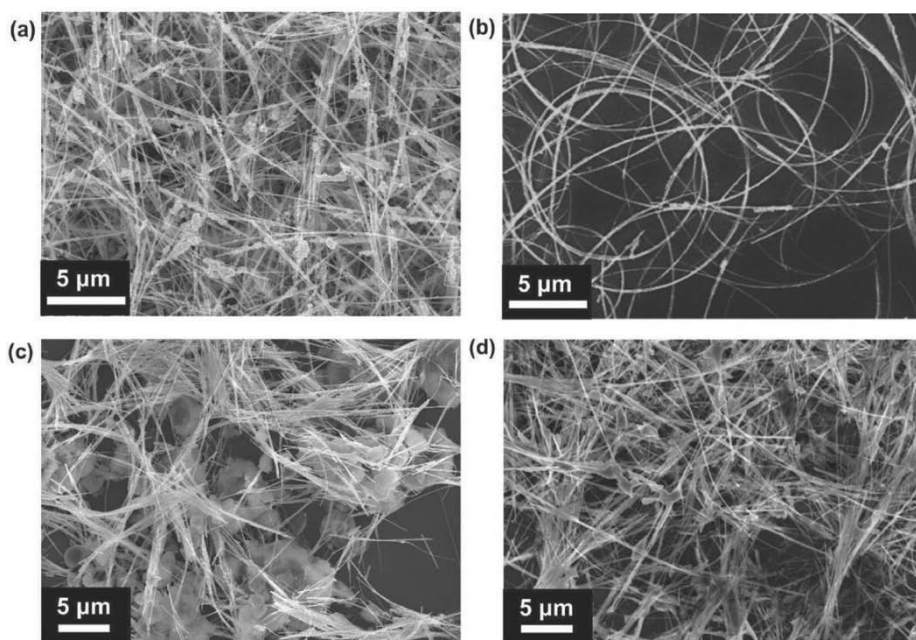


**Figure 3.1** SEM images of copper nanowires synthesized by different ratios of binary solvents. (a) 30 mL EG and 0 mL GC, (b) 20 mL EG and 10 mL GC, (c) 10 mL EG and 20 mL GC, (d) 0 mL EG and 30 mL GC.

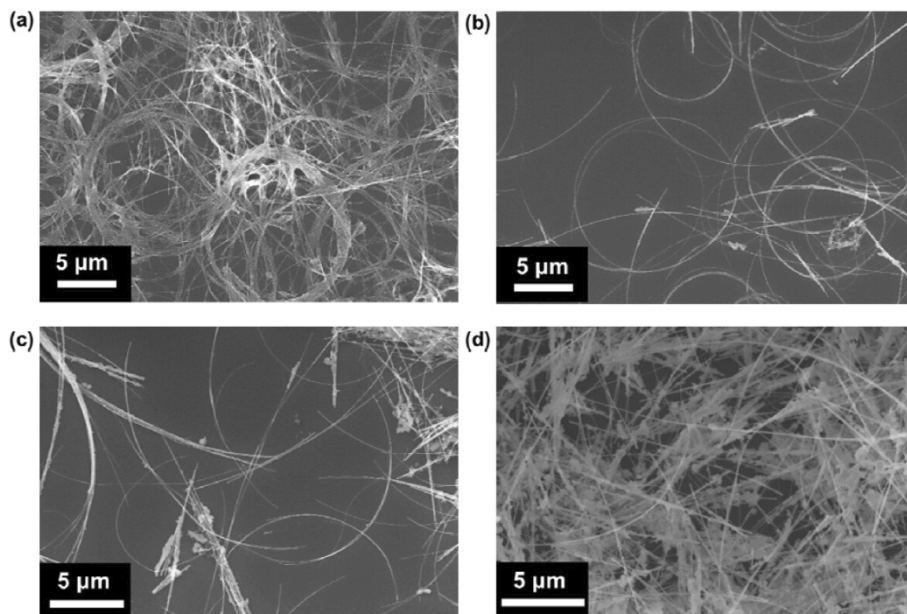


**Figure 3.2** SEM images of Cu NWs synthesized by different reaction time at 208 °C. (a) 1 min, (b) 20 min, (c) 1 h and (d) 2 h.

On the analysis of SEM and TEM images, the average diameter of CCNs is 50 nm, and the length in 25–40  $\mu\text{m}$  range. (Figure 3.3a) The crystal structure of CCNs was measured by X-ray diffraction (XRD) and a selected area of electron diffraction (SAED). The XRD pattern is shown in Figure 3.3b. The three characteristic peaks were only located at  $2\theta = 43.5, 50.7,$  and  $74.4^\circ$ , which correspond to the diffractions from the  $\{111\}, \{200\},$  and  $\{220\}$  planes of face-centered cubic (fcc) structured Cu (JCPDS # 03-1028); means the pure phase of the CCNs.<sup>[22]</sup> On the basis of the SAED analysis, the pattern acquired from individual slightly and highly curved nanowires are shown in Figure 3.3c and 3.4. The diffraction spots in Figure 3.3c are indexed by fcc structured Cu, which indicates that the electron beam belongs to the  $[110]$  zone axis and the CCNs elongated to the  $[1\bar{1}0]$  direction.<sup>[21, 23]</sup> Figure 3.4 shows the complex mixture diffraction spots induced from  $[001]$  zone axis and  $[112]$  zone axis, when the electron beam is perpendicular to bottom plane of the CCNs. Obviously, the crystallization of crystal planes from  $[001]$  zone is not good in curved structural Cu NWs. Particularly, the light intensity of the  $(\bar{2}\bar{2}0)$  diffraction spot from  $[001]$  zone axis is very weak even disappear in the SAED pattern. We speculated that the line defects and twisted twin plane start from this plane induced from  $(\bar{2}\bar{2}0)$  plane, due to the effect of interface reaction from GC and EG. Figure

3.3d is the ultraviolet–visible (UV–vis) absorption spectrum of CCNs, which were as-synthesized and dispersed in the hexane solution. As previously reported, the surface plasmon resonance range for Cu nanoparticles was 550–590 nm, because free electrons in the conduction band were induced and oscillated by light.<sup>[24]</sup> The absorption peak was located at 572 nm in this research, which attributed to the plasma excitation in CCNs.

Through observation of SEM images, most of the CCNs exist individually, and others are mutually twisted from two or three wires that can even form a ring structure. (Figure 3.5) The nanoring structure is made by self-connection of curved nanowires edges, because of the Ostwald ripening in the reaction.<sup>[18]</sup> Although longer nanowires are more effective in fabricating high performance FTCE, we optimized the size of CCNs for the MDD method after considering the aggregation and precipitation.<sup>[25]</sup>

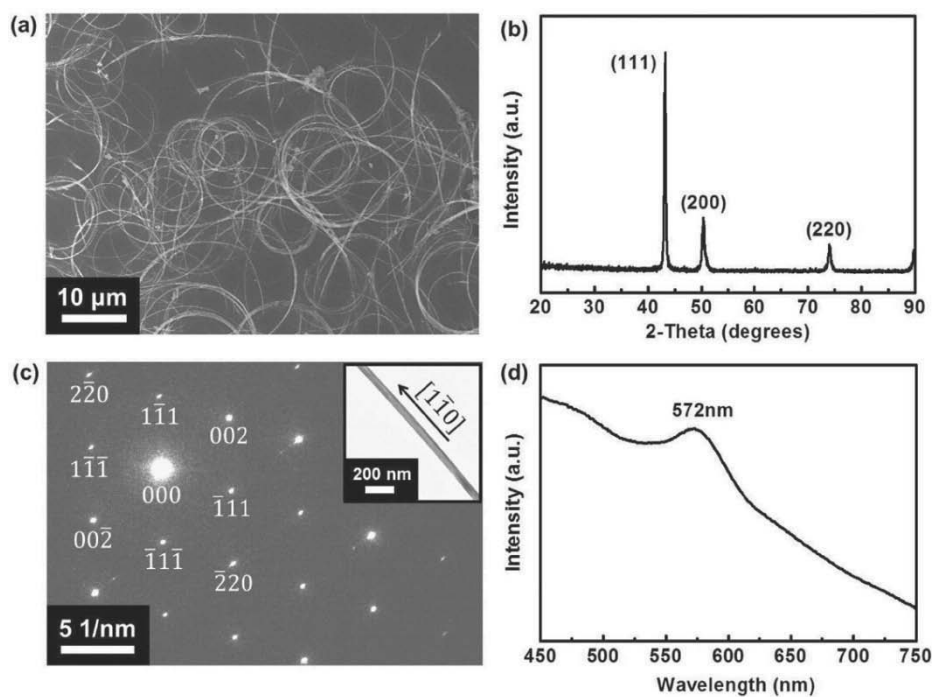


**Figure 3.3** (a) Representative SEM image of CCNs. (b) XRD patterns. (c) SAED pattern of the slightly CCNs along the [110] zone axis, corresponding to the top-view TEM image. (d) UV-vis absorption spectrum.

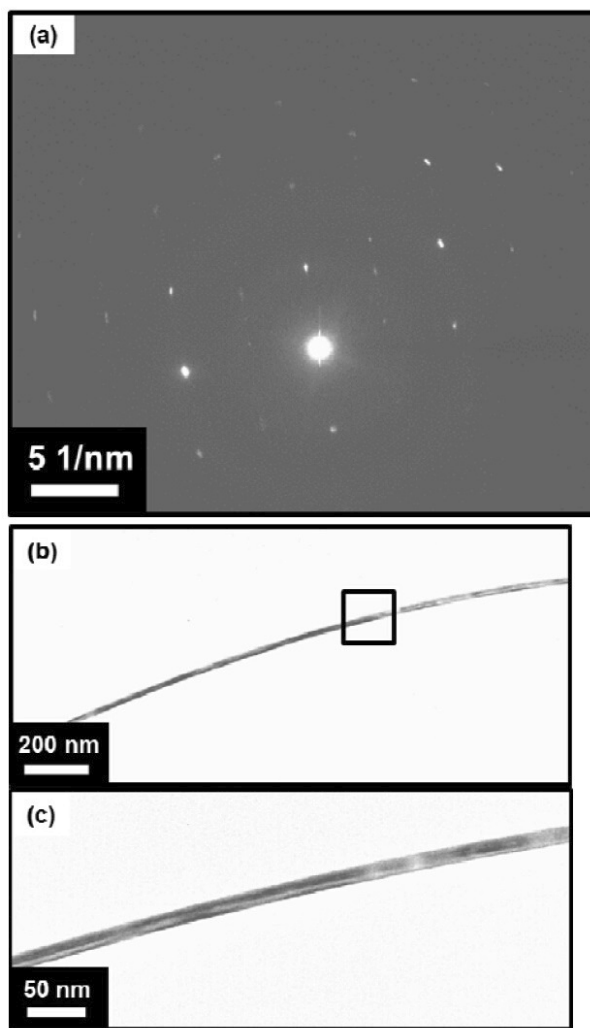


**Figure 3.4** (a) SEAD pattern of CCNs. (b) TEM and (c) enlarged TEM image of black boxed areas.

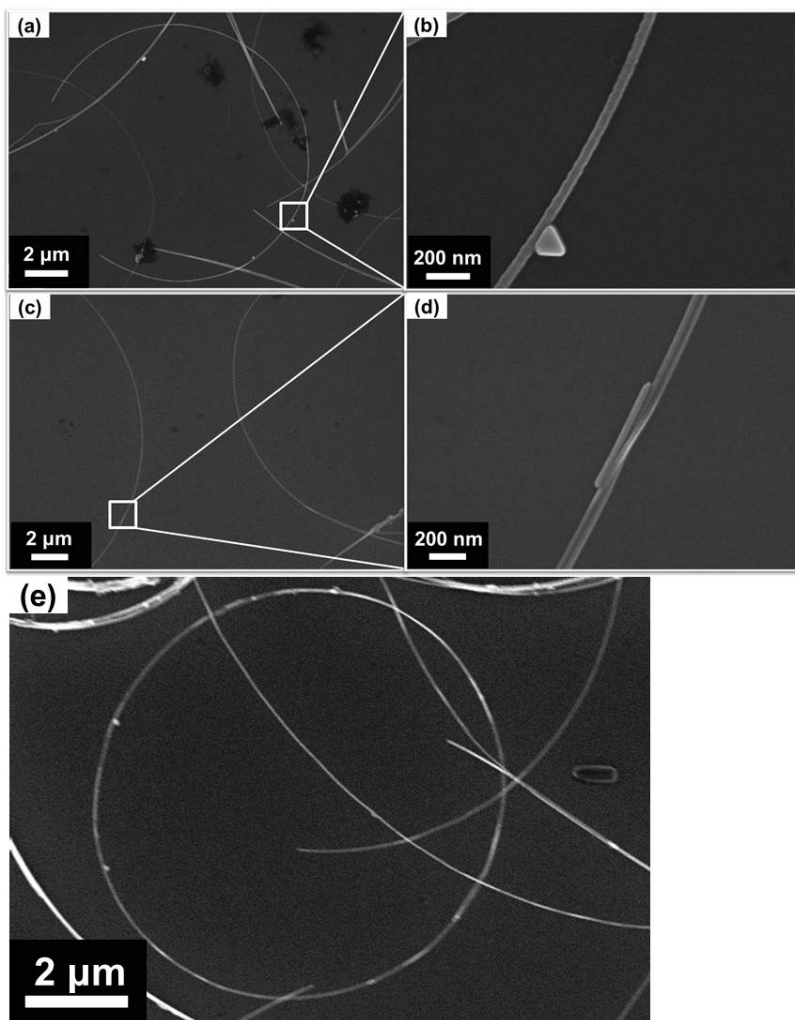


**Figure 3.5** SEM images of typical (a, b) single CCN, (c, d) twisted CCNs and (e) ring structure of Cu NW.

### 3.3.3 Meniscus-dragging deposition

In general, the Cu NWs thin films were fabricated by various conventional coating techniques that included wire-wound rod coating, filtration-transfer method, and air-spraying.<sup>[4, 22, 26]</sup> However, some of these strategies are difficult for Cu NWs film depositions uniformly, rapidly, simply and cost-effectively, due to the complicated processes, harsh coating conditions, high cost equipment and the colloidal particle aggregation. In particular, the filtration-transfer method required vacuum process and high cost nitrocellulose membrane to transfer the Cu NWs on the transparent substrate. This increases the total price of transparent electrodes until they are almost as comparable as Ag NWs.<sup>[22]</sup> In addition, the transfer membrane cannot be applied to large size and can easily fail due to incomplete transfers or tearing problems.

In this study, a facile and simple MDD method was used for coating the CCNs on glass or PET substrates to overcome above-mentioned drawbacks in the conventional coating processes. (Scheme 3.1) The MDD technique can offer a precise control of film thickness by varying simple coating parameters (concentration of materials, deposition speed, deposition number, deposition angle) with extremely low consumption of coating materials.<sup>[13]</sup>

<sup>27, 28]</sup> A drop of CCNs suspension with a volume of 20  $\mu\text{l}$  was injected between the deposition and coating substrate. The deposition plate was pushed back-and-forth to drag the meniscus of the CCNs solution trapped between two plates. During the alternating motion of the deposition plate, the CCNs suspended in the wedge of two plates were evenly deposited on the coating substrate. After rotating the pre-coated substrate with  $90^\circ$ , the same coating procedure was repeated to form large number of junctions between the individual CCN on the substrate.

### 3.3.4 Solvent-dipped annealing method

In order to achieve proper conductivity, the coated Cu NWs were generally sintered at high temperature with reducing gas.<sup>[22, 26, 29]</sup> However, the high sintering temperature is still limited to common plastic substrate, such as PET. In addition, Cu is very sensitive to oxygen at such high temperature. Recently, optical sintering method is explored to connect the Cu NWs through laser or flash light.<sup>[5]</sup> This method strongly depends on instant heating at the junction of wires. However, the high-price optical tools induced the increasing of total production cost and limitation of widespread application. In addition, for non-oxygen condition, the vacuum equipment has often been used in the sintering process, which results in an expensive and limited large scale process.<sup>[22, 29]</sup>

With that in mind, we firstly introduce the solvent-dipped annealing method to connect the CCNs by removing oxide layer without any vacuum and transfer process. The CCNs thin films coated on the glass or PET substrates were reduced by covering the films with a small volume of GC or NaBH<sub>4</sub> solution and were heated on a hotplate for 3 min. The CCNs films on glass substrate were reduced by the GC solvent at 140 °C, while, the 2 mg·mL<sup>-1</sup> of NaBH<sub>4</sub> solution was used for annealing the CCNs film on PET

substrate at 50 °C. (Scheme 3.1) The annealed CCNs films were washed with ethanol and acetone. Then, the resistance of CCNs thin film changes from mega-ohm to ohm scale. For metal nanowire type, except for intrinsic electrical characteristic of materials, the opto-electrical performance of thin films strongly depends on random networking of wires and their contact resistance.<sup>[30-32]</sup> However, the natural oxide layer on the surface acts as a barrier, enhances the contact resistance even loses the electrical performance.<sup>[10, 33, 34]</sup> In order to remove the natural oxide layer and successfully connect with each other, the CCNs coated onto slide glass were reduced by GC at 140 °C of annealing condition. Then, residual GC was eliminated by washing off the ethanol and acetone. This process improved the transmittance, because the un-connected single nanowire was also removed by washing. Figure 3.6a is a transmittance of the CCNs thin films, which increased 3.76% of transmittance after washing step.

The opto-electrical property of the CCNs films were finely tuned by the MDD method. As shown in Figure 3.6b, the transmittance spectra of the CCNs films on the glass substrate can be controlled by varying the deposition number (DN, one alternating motion of the deposition plate is defined as  $DN = 1$ ). The transmittance at 550 nm of the CCNs film was gradually lowered and the corresponding sheet resistance was reduced with

increasing the DN (Figure 3.6c), because the larger number of contact points between the CCNs can be formed at the higher DN, like shown in Figure 3.6d. As shown in Figure 3.7, expressing the sheet resistance as a function of the transmittance at 550 nm, the precise control of the opto-electrical properties of the CCNs films was enabled by applying the MDD technique. Clearly, the CCNs films prepared in this work had excellent opto-electrical performances (at  $T = 80.07\%$ ,  $R_s = 32.79 \Omega \cdot \square^{-1}$ ;  $T = 84.25\%$ ,  $R_s = 53.11 \Omega \cdot \square^{-1}$ ;  $T = 86.83\%$ ,  $R_s = 80.14 \Omega \cdot \square^{-1}$ ; and  $T = 88.40\%$ ,  $R_s = 98.07 \Omega \cdot \square^{-1}$ ) which are comparable to those of Cu NWs films formed by other coating method.<sup>[1, 5, 23, 35]</sup> Furthermore, the suggested methods using CCNs films are also applied for fabrication of FTCE with low-temperature, vacuum-free, transfer-free, and simple processes.

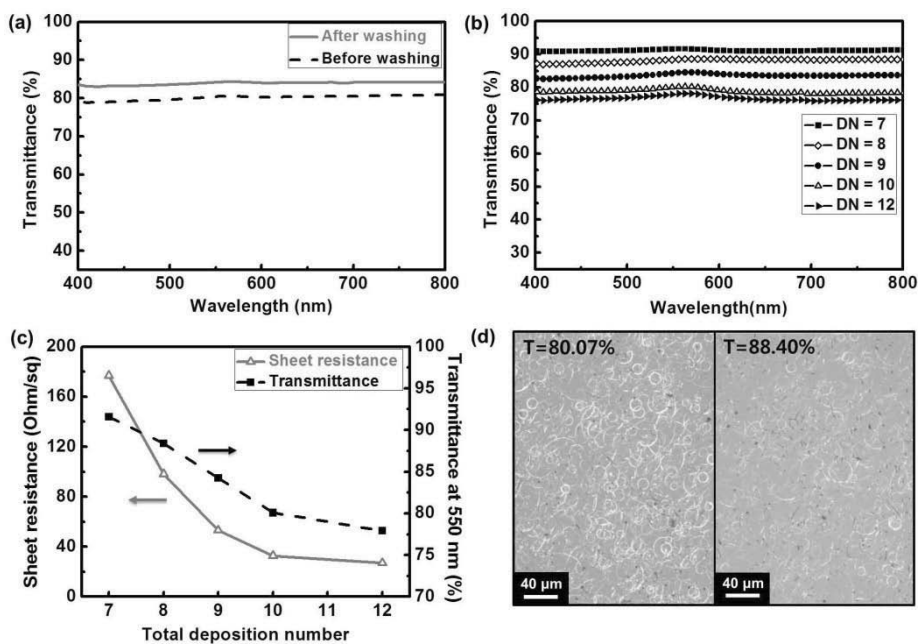


**Figure 3.6** (a) UV-vis transmission spectra of CCNs thin film on glass substrate before and after washing. (b) UV-vis transmission spectra of CCNs thin films with different deposition number. (c) Sheet resistance and transmittance at 550 nm as a function of deposition number. (d) Optical microscopy images of two representative electrodes of 80.07% and 88.40%.

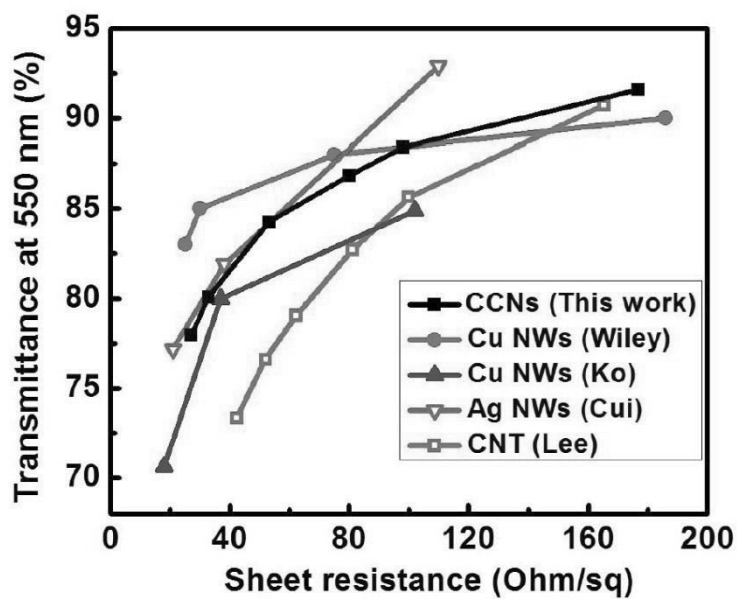


**Figure 3.7** A plot of transmittance at 550 nm versus sheet resistance for CCNs thin films on glass substrate compared with other groups.

### 3.3.5 Flexible transparent conductive electrode

The highly uniform and robust FTCE was also prepared by the same methods, such as CCNs synthesis, MDD coating and solvent-dipped networking. For excellent flexibility, the common flexible PET as a substrate was used to instead of slide glass from the above mentioned experiments. To remove the natural oxide layer, the CCNs film on PET substrate was annealed with  $\text{NaBH}_4$  solution at  $50\text{ }^\circ\text{C}$ , which is below the glass transition temperature ( $80\text{ }^\circ\text{C}$ ) of PET. Typically, the CCNs thin film on PET substrate exhibited  $99.14\ \Omega\cdot\text{cm}^{-1}$  of low sheet resistance at 86.62% of high transmittance. (Figure 3.8a and b) The electrical and mechanical performances of Cu NWs electrode are strongly related to the percolation in nanowire junction.<sup>[36]</sup> For general straight Cu NWs, even though random networking of linear structure and inherent malleability of Cu can slightly resist the bending, the junction fracture was induced by strong or too much bending. In particular, the single linear nanowire as a typical one-dimensional material is difficult to resist the strain from two-dimensional plane.<sup>[36]</sup> This is because the linear parts of the straight Cu NWs have no stretchable ability that can reduce the stress from tensile strain.<sup>[37, 38]</sup> These junction fractures were unrecoverable to damage the networking and reduce

the conductivity. Although the deep percolation enhanced connection bond in nanowire junctions, the PET substrate is not suitable for high temperature sintering process, because of their low glass transition temperature (80 °C). However, the CCNs grow to a two-dimensional structure through increasing the crystal defects in growth process. These two-dimensional nanowires structure have good elastic property to resist tensile strain from the film. Compared to the straight type, the CCNs thin film is highly stable under excessive or strong bending. (Figure 3.8c) The deformation of curved structure was caused by line defects and twisted twin plane, which increase the softness of CCNs, even more than the linear type.<sup>[12, 39]</sup> Furthermore, most of stress from tensile strain was received by the curved parts of nanowires due to their self-bendable structure. Also, three-dimensional percolation can improve the conductivity and flexibility of Cu NWs electrode, due to their stable structure and many junctions.<sup>[36, 40]</sup> In order to ensure high transparency of FTCE, the deposition quantity of CCNs is only a little in this system. Therefore, the sheet resistance of CCNs based FTCE is much higher than conductive Cu line or non-transparent Cu films.<sup>[10]</sup>

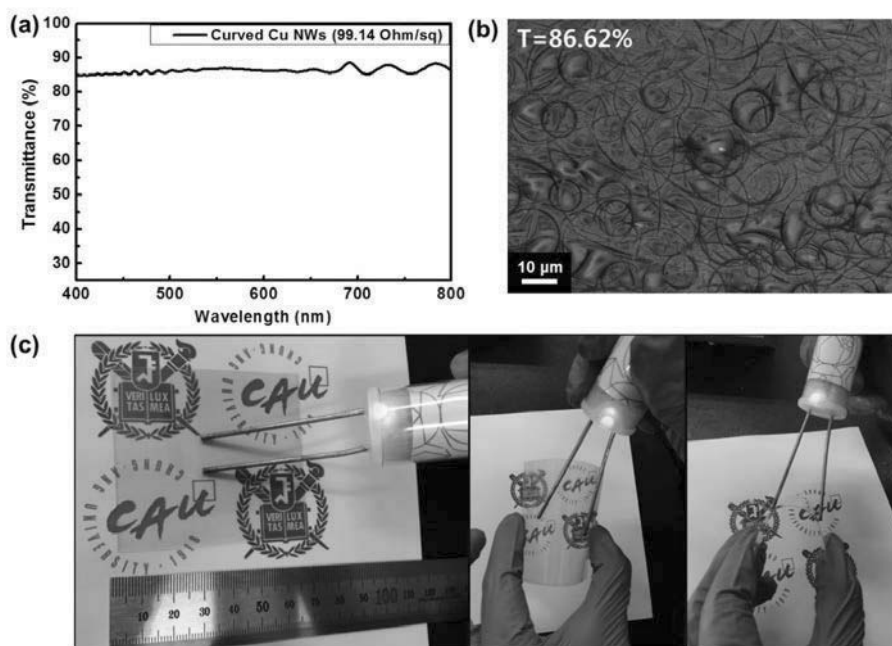


**Figure 3.8** (a) UV-vis transmission spectrum and (b) SEM image of curved Cu NWs (CCNs) thin film ( $T = 86.62\%$ ,  $R_s = 99.14 \Omega \cdot \square^{-1}$ ) on PET substrate. (c) Photographs of CCNs-based FTCE, and lighting of an LED with an external power supply.

To test flexibility, the FTCE was stressed by different bending cycles and bending radius using a lab-designed bending machine, which was bended by 5 mm of bending radius under  $50 \text{ mm}\cdot\text{s}^{-1}$  of motion speed from 1 to 2000 cycles. As a result, the resistance ratio was still maintained below 1.04, even bended up to 2000 cycles. (Figure 3.9a) As a comparison, the linear Cu NWs show highly degradation of electrical performance within 2000<sup>th</sup> bending. Figure 3.9b shows the resistance ratio of several bending radius (5, 10, 15 and 20 mm) of thin films. In comparison to linear Cu NWs, the CCNs thin film has a very low variation ( $R/R_0 < 1.05$ ) even tensile or compressive bending of 5 mm radius. The excellent durability of CCNs thin film is attributed to their self-bendable structure and high softness. Compared to other FTCEs, the CCNs thin film on PET substrate exhibited more outstanding performances of transparency, conductivity and flexibility.<sup>[5, 23, 41]</sup>

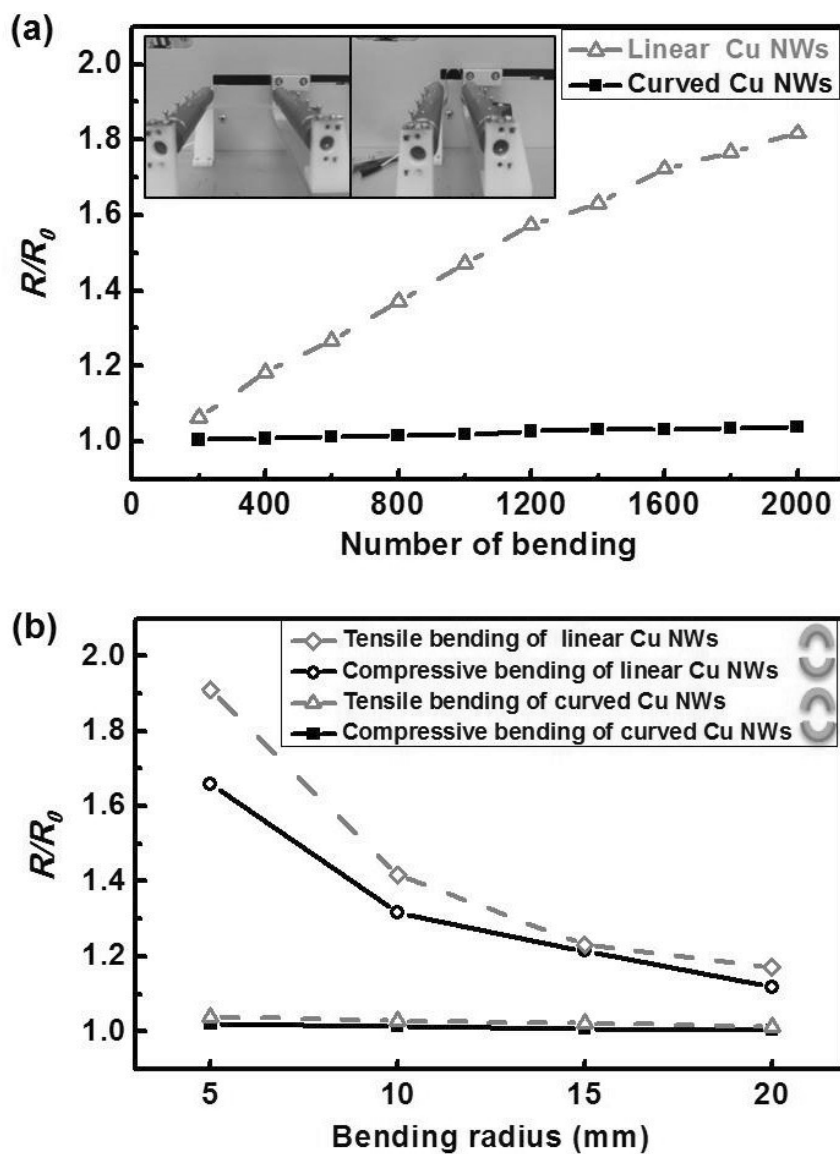


**Figure 3.9** The relative resistance of linear Cu NWs and curved Cu NWs (CCNs) based FTCE under (a) cycling number of bending and (b) bending radius of 20, 15, 10, and 5 mm.

### 3.4 Conclusion

In summary, we have demonstrated the whole manufacturing process of highly robust flexible transparent conductive electrode (FTCE) using the curved copper nanowires (CCNs), which consisted of the binary polyol co-reduction method for CCNs, the MDD method for simple coating, and the GC/NaBH<sub>4</sub> solution dipped annealing method to connect the CCNs. The CCNs thin films on a slide glass showed a low sheet resistance with a high transparency ( $T = 86.83\%$ ,  $R_s = 80.14 \Omega \cdot \square^{-1}$ ). Also, as a highly robust FTCE, the CCNs thin film on PET substrate exhibited an excellent flexibility and durability ( $R/R_0 < 1.05$  at 2000 bending, 5 mm of bending radius) with high opto-electrical performance ( $T = 86.62\%$ ,  $R_s = 99.14 \Omega \cdot \square^{-1}$ ). We believe that the suggested methods for highly robust FTCE in this work are promising in wide applications.

## References

- [1] L. Hu, H. S. Kim, J.-Y. Lee, P. Peumans, Y. Cui, *ACS Nano* **2010**, *4*, 2955.
- [2] J. Wu, M. Agrawal, H. A. Becerril, Z. Bao, Z. Liu, Y. Chen, P. Peumans, *ACS Nano* **2009**, *4*, 43.
- [3] M.-G. Kang, M.-S. Kim, J. Kim, L. J. Guo, *Adv. Mater.* **2008**, *20*, 4408.
- [4] S. Ye, A. R. Rathmell, Z. Chen, I. E. Stewart, B. J. Wiley, *Adv. mater.* **2014**, *26*, 6670.
- [5] S. Han, S. Hong, J. Ham, J. Yeo, J. Lee, B. Kang, P. Lee,; J. Kwon, S. S. Lee, M.-Y. Yang, S. H. Ko, *Adv. Mater.* **2014**, *26*, 5808.
- [6] D. Zhang, K. Ryu, X. Liu, E. Polikarpov, J. Ly, M. E. Tompson, C. Zhou, *Nano Lett.* **2006**, *6*, 1880.
- [7] D. S. Hecht, L. Hu, G. Irvin, *Adv. Mater.* **2011**, *23*, 1482.
- [8] R. R. Wang, J. Sun, L. A. Gao, C. H. Xu, J. Zhang, Y. Q. Liu, *Nanoscale* **2011**, *3*, 904.
- [9] C.-H. Liu, X. Yu, *Nanoscale Res. Lett.* **2011**, *6*, 75.
- [10] Z. Yin, C. Lee, S. Cho, J. Yoo, Y. Piao, Y. S. Kim, *Small* **2014**, *10*, 5047.
- [11] H.-G. Im, S.-H. Jung, J. Jin, D. Lee, J. Lee, D. Lee, J.-Y. Lee, I.-D. Kim, B.-S. Bae, *ACS Nano*, **2014**, *8*, 10973.
- [12] Y. J. Zhan, Y. Lu, C. Peng, J. Lou, *J. Cryst. Growth* **2011**, *325*, 76.
- [13] Y. U. Ko, S. Cho, K. S. Choi, Y. Park, S. T. Kim, N. H. Kim, S. Y. Kim, S. T. Chang, *J. Mater. Chem.* **2012**, *22*, 3606.
- [14] G.-H. Lim, S. J. Lee, I. Han, S. Bok, J. H. Lee, J. Nam, J. H. Cho, B. Lim, *Chem. Phys. Lett.* **2014**, *602*, 10.
- [15] B. Jia, M. Qin, Z. Zhang, A. Chu, L. Zhang, Y. Liu, X. Qu, *J. Mater. Sci.* **2013**, *48*, 4073.
- [16] H. Hofmeister, *Fivefold twinned nanoparticles*. Encyclopedia of Nanoscience and Nanotechnology; American Scientific: Stevenson

- Ranch, CA (2004).
- [17] P. M. Ajayan, L. D. Marks, *Phys. Rev. Lett.* **1998**, *60*, 585.
- [18] L. Zhou, X.-F. Fu, L. Yu, X. Zhang, X.-F. Yu, Z.-H. Hao, *Appl. Phys. Lett.* **2009**, *94*, 153102.
- [19] Y. Xia, Y. Xiong, B. Lim, S. E. Skrabalak, *Angew. Chem. Int. Ed.* **2009**, *48*, 60.
- [20] S. Bhanushali, P. Ghosh, A. Ganesh, W. Cheng, *Small* **2015**, *11*, 1232.
- [21] B. Wiley, Y. Sun, B. Mayers, Y. Xia, *Chem. Eur. J.* **2005**, *11*, 454.
- [22] D. Zhang, R. Wang, M. Wen, D. Weng, X. Cui, J. Sun, H. Li, Y. Lu, *J. Am. Chem. Soc.* **2012**, *134*, 14283.
- [23] A. R. Rathmell, S. M. Bergin, Y.-L. Hua, Z.-Y. Li, B. J. Wiley, *Adv. Mater.* **2010**, *22*, 3558.
- [24] T. M. D. Dang, T. T. T. Le, E. F. Blanc, & M. C. Dang, *Adv. Nat. Sci. Nanosci. Nanotechnol.* **2011**, *2*, 1.
- [25] J. Lee, P. Lee, H. B. Lee, S. Hong, I. Lee, J. Yeo, S. S. Lee, T.-S. Kim, D. Lee, S. H. Ko, *Adv. Funct. Mater.* **2013**, *23*, 4171.
- [26] A. R. Rathmell, B. J. Wiley, *Adv. Mater.* **2011**, *23*, 4798.
- [27] J. S. Lee, N. H. Kim, M. S. Kang, H. Yu, D. R. Lee, J. H. Oh, S. T. Chang, J. H. Cho, *Small* **2013**, *9*, 2817.
- [28] Y. U. Ko, N. H. Kim, N. R. Lee, S. T. Chang, *Carbon* **2014**, *77*, 964.
- [29] H. Guo, N. Lin, Y. Chen, Z. Wang, Q. Xie, T. Zheng, N. Gao, S. Li, J. Kang, D. Cai, D.-L. Peng, *Sci. Rep.* **2013**, *3*, 2323.
- [30] J. Lee, I. Lee, T.-S. Kim, J.-Y. Lee, *Small* **2013**, *9*, 2887.
- [31] S. De, T. M. Higgins, P. E. Lyons, E. M. Doherty, P. N. Nirmalraj, W. J. Blau, J. J. Boland, J. N. Coleman, *ACS Nano* **2009**, *3*, 1767.
- [32] A. Kamyshny, S. Magdassi, *Small* **2014**, *10*, 3515.
- [33] C. Sachse, N. Weiß, N. Gaponik, L. Müller-Meskamp, A. Eychmüller, K. Leo, *Adv. Energy Mater.* **2014**, *4*, 1300737.
- [34] W. Gaynor, S. Hofmann, M. G. Christophoro, C. Sachse, S. Mehra, A. Salleo, M. D. McGehee, M. C. Gather, B. Lüssem, L. Müller-

- Meskamp, P. Peumans, K. Leo, *Adv. Mater.* **2013**, *25*, 4006.
- [35] U. J. Kim, I. H. Lee, J. J. Bae, S. Lee, G. H. Han, S. J. Chae, F. Günes, J. H. Choi, C. W. Baik, S. Kim, J. M. Kim, Y. H. Lee, *Adv. Mater.* **2011**, *23*, 3809.
- [36] Y. Tang, S. Gong, Y. Chen, L. W. Yap, W. Cheng, *ACS Nano* **2014**, *8*, 5707.
- [37] D. C. Hyun, M. Park, C. Park, B. Kim, Y. Xia, J. H. Hur, J. M. Kim, J. J. Park, U. Jeong, *Adv. Mater.* **2011**, *23*, 2946.
- [38] S. Xu, Y. Zhang, J. Cho, J. Lee, X. Huang, L. Jia, J. A. Fan, Y. Su, J. Su, H. Zhang, H. Cheng, B. Lu, C. Yu, C. Chuang, T.-I. Kim, T. Song, K. Shigeta, S. Kang, C. Dagdeviren, I. Petrov, P. V. Braun, Y. Huang, U. Paik, J. A. Rogers, *Nat. Commun.* **2013**, *4*, 1543.
- [39] C. Peng, Y. Zhan, J. Lou, *Small* **2012**, *8*, 1889.
- [40] Y. Tang, K. L. Yeo, Y. Chen, L. W. Yap, W. Xiong, W. Cheng, *J. Mater. Chem. A* **2013**, *1*, 6723.
- [41] H. Z. Geng, K. K. Kim, K. P. So, Y. S. Lee, Y. Chang, Y. H. Lee, *J. Am. Chem. Soc.* **2007**, *129*, 7758.

# **Chapter 4. Curved Copper Nanowires-based Robust Flexible Transparent Electrodes via All-solution Approach**

## **4.1 Introduction**

Metal nanowire (NW)-based flexible transparent conductive electrodes (FTCEs) have attracted considerable attention owing to their demand in flexible electronics.<sup>[1, 2]</sup> To date, most transparent electrodes in modern flat-panel electronics are made with indium tin oxide (ITO) materials owing to their good electrical conductivity and high transparency in the visible range.<sup>[1, 3]</sup> However, the scarcity of In and the high-vacuum sputtering required for manufacturing make the cost too high for the public.<sup>[1, 4, 5]</sup> More importantly, the high brittleness of ITO is a critical limitation that has prompted efforts to develop new alternatives for advanced flexible devices. In the past several years, solution-processable single-walled carbon nanotube (SWCNT) and reduced graphene oxide (RGO) thin films pioneered the development of FTCEs as substitute materials.<sup>[6, 7]</sup> Although FTCEs exhibit excellent conductivity and remarkable flexibility, the high

contact resistance at their junctions is an obstacle for high electrical performance.<sup>[6, 8]</sup> SWCNTs and RGO are particularly useful for the development of useful devices, such as sensors, supercapacitors, and batteries.<sup>[9-11]</sup> However, entirely replacing ITO with these materials for flexible optical devices is difficult.

As the most promising materials for replacing ITO, solution-processable Ag and Cu NW thin films have been extensively explored for FTCEs because of their low sheet resistance, high transparency, and outstanding flexibility.<sup>[12, 13]</sup> To fabricate FTCEs from these materials, metal NWs are randomly distributed on the transparent substrate via a solution-based coating method and deeply percolated within its networks via thermal welding. The large areas produced by uncovered NW films ensure a high transparency. The connected NW networks provide electron transference, yielding excellent electrical conductivity. Furthermore, the inherent metallic ductility and high aspect ratio of the one-dimensional NW structure are beneficial for the flexibility of FTCEs. Although many reported Ag and Cu NW thin films have superior functional properties to ITO, their high surface roughness and difficulty of patterning limit their applications in FTCEs for flexible devices.<sup>[14, 15]</sup> Moreover, the high cost of material synthesis must be reduced for widespread commercialization. In particular, Ag NW thin films

have been comprehensively researched, exhibiting considerable optoelectrical performance.<sup>[12, 16]</sup> However, Ag is a noble metal that has been even more expensive and scarce than In in recent years.<sup>[17]</sup>

Compared with Ag, Cu-based materials are abundant, significantly cheaper, and have nearly identical electrical properties, making them suitable for the requirements of the electronics market.<sup>[18]</sup> In our previous study, we synthesized Cu NWs with curved structures using a low-cost and simple binary polyol method and coated them on a polyethylene terephthalate (PET) substrate as an FTCE.<sup>[19]</sup> The curved Cu NWs (CCNs) not only provided shape control but also enhanced the mechanical properties of the FTCEs, as the self-bendable structure induced good ductility and softness.<sup>[19]</sup> Compared with straight nanowires, CCNs usually occupy more space and have the same electron-transfer properties; thus, they more easily form an effective network. Furthermore, the curved shape has a smaller point-to-point linear distance per NW, resulting in higher optoelectrical performance and patternability for FTCEs.<sup>[19]</sup> However, several technical issues must be solved for the practical applications of CCNs, such as their low robustness, high surface roughness, and difficulty of patterning. Additionally, few Cu NW-based FTCEs have been fabricated via all-solution processes without complicated material synthesis, expensive

facilities, or harsh conditions.

Herein, we propose an all-solution approach for the entire manufacturing process of CCN-based FTCEs, comprising multi-polyol synthesis, meniscus-dragging deposition (MDD), polyurethane (PU)-stamped patterning, solvent-dipped welding, and PU-embedded transfer. Furthermore, a series of innovative methods are suggested for solving the technical issues regarding the fabrication of CCN-based FTCEs with high optoelectrical performance, such as the low robustness, high surface roughness, and difficulty of patterning.

## **4.2 Experimental section**

### **4.2.1 Preparation of CCNs via multi-polyol synthesis**

In a typical synthesis procedure, 2 mmol of a CuCl, 6 mmol of an oleylamine, and 0.3 mmol of an ammonium-chloride were dissolved in a reductant containing the following mixed polyols: 15 mL of ethylene glycol, 10 mL of glycerol, and 5 mL of polyethylene glycol<sub>200</sub>. The Cu<sup>+</sup>-amine complex was fully formed via strong magnetic stirring when the reaction temperature was increased to 110 °C. After 15 min, the temperature was increased to 208 °C at a heating rate of 9 °C·min<sup>-1</sup>, followed by 20 min of refluxing. The resulting red-brown CCNs, which were completely prepared, were cooled to 25 °C via cold-water quenching. The CCNs were washed with n-hexane and ethanol, then centrifuged for 5 min at 6,000 rpm. The washing and centrifugation were repeated three times. Finally, the CCNs were re-dispersed in cyclohexane for the coating step.

### **4.2.2 CCN film coating via MDD**

An ethanol-washed polyimide (PI) film and a slide glass were prepared

as the coating substrate and deposition plate, respectively. We injected 20  $\mu\text{L}$  of a CCN dispersion ( $1.5 \text{ mg}\cdot\text{mL}^{-1}$ ) between the PI substrate and the deposition plate using a micropipette at a deposition angle of  $\theta = 30^\circ$ . The trapped CCN meniscus was spread ten times on the coating plate via linear back-and-forth motion at a speed of  $40 \text{ mm}\cdot\text{s}^{-1}$ . After the solvent of the CCN film dried, a specific number of additional CCN coatings was applied on the CCN film, yielding an aligned CCN film. The substrate with the aligned CCN film was rotated by  $90^\circ$ , and CCNs were vertically deposited on the parallel CCN film using the same method. After repeating these procedures, we obtained a crossed-formation CCN film on the PI substrate.

### **4.2.3 CCN film patterning via PU-stamped patterning**

Two parts of a urethane liquid compound (Clear Flex® 95, Smooth-On) were mixed at a weight ratio of 1.5:1 and pre-cured on a line-space patterned polydimethylsiloxane (PDMS) mold at a constant temperature of  $40 \text{ }^\circ\text{C}$ . After 5 h of pre-curing, the reverse-patterned PU matrix was obtained. The procured PU matrix was directly stamped onto the CCN thin film (77.26%  $T$  of sample, before washing) for 1 h with  $0.12 \text{ N}\cdot\text{cm}^{-2}$  of pressure. The CCNs were completely embedded in the convex parts of the

PU matrix, which was carefully peeled from the PI substrate.

#### **4.2.4 CCN percolation via solvent-dipped welding**

The CCN thin film on the PI substrate was covered by a PEG<sub>200</sub> solvent. When the temperature was increased to 200 °C for 30 min, the natural oxide layer was sufficiently reduced, and the film gradually became conductive. A pressure of 0.3 N·cm<sup>-2</sup> was applied on the CCN thin film using a weight, while the other conditions were kept unchanged. After another 30 min of pressing for complete percolation, the weight was carefully removed from CCN thin film. The CCN thin film was rapidly placed in acetone, and the temperature of the PEG<sub>200</sub> was reduced to 140 °C. Finally, the CCN thin film was washed with acetone to remove the residual PEG<sub>200</sub>.

#### **4.2.5 CCN film smoothing via PU-embedded transfer**

Two parts of the urethane liquid compound (Clear Flex® 95, Smooth-On) were mixed at a weight ratio of 1.5:1 and pre-cured on a flexible transparent substrate (PET, PDMS) at a constant temperature of 40 °C. After 10 h of pre-curing, the PU matrix was kept in contact with the CCN film for 30 min

with an applied pressure of  $0.3 \text{ N}\cdot\text{cm}^{-2}$ . Then, the CCNs were successfully transferred to the PU matrix when it was carefully peeled from the PI substrate. The PU matrix was completely cured through an additional 2 h of curing at  $40 \text{ }^\circ\text{C}$ . The flexible transparent substrate was easily peeled from the PU matrix if required.

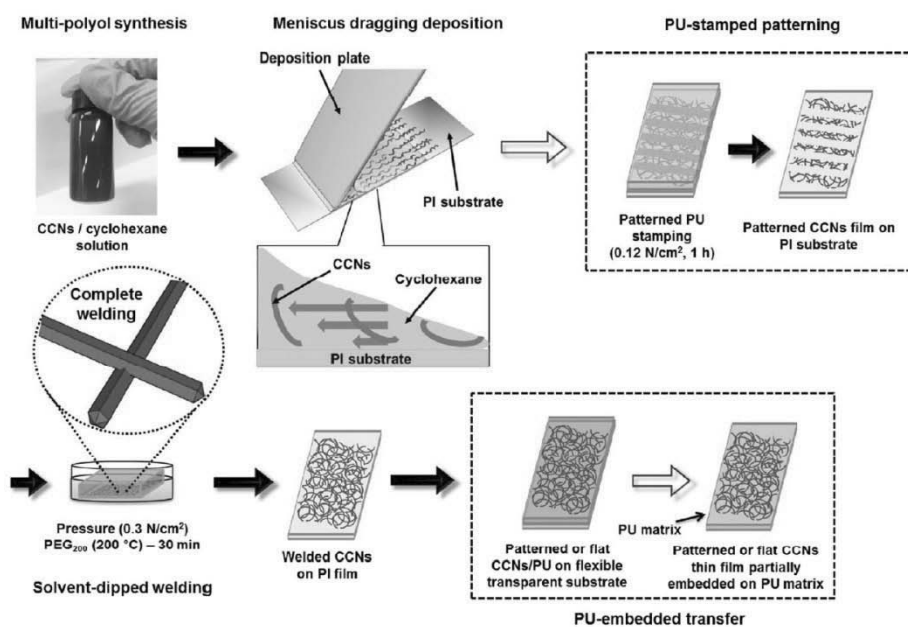
#### **4.2.6 Characterization of CCNs and FTCEs**

The prepared CCNs were characterized using scanning electron microscopy (Hitachi S-4800), X-ray diffraction measurements (Bruker D8 DISCOVER), ultraviolet–visible spectroscopy (PerkinElmer Lambda 35), and high-resolution transmission electron microscopy (JEOL JEM-2100F). The optoelectrical performance of the CCN thin films was investigated using optical microscopy (Olympus utv1x-2), UV–vis–NIR spectroscopy (Jasco V-670), and a four-point probe (Keithley 2612A source meter). The transmittance of the CCN thin films was calculated based on identical reference substrates, such as PI, PU, and PU/PET. Therefore, the transmittances proposed in this work were only measured for the CCN thin films, without considering the substrates. The surface roughness was measured using atomic-force microscopy (Park Systems XE-100).

## 4.3 Results and discussion

### 4.3.1 Synthesis process

The CCN-based smooth, robust, and patternable FTCEs were fabricated by a combination of several innovative techniques—as illustrated in Scheme 4.1—including synthesis, coating, patterning, welding, and transfer. Although many researchers emphasize the low price of Cu NWs, the use of expensive reagents, catalysts, and instruments, as well as the experimental conditions, make FTCEs with Cu NWs even more expensive to fabricate than those with Ag NWs.<sup>[20, 21]</sup> To overcome this problem, the CCNs were prepared with a commonly used reagent in a short reaction time of 1 h via a multi-polyol synthesis method and homogeneously dispersed in a cyclohexane solvent, which was modified from the binary polyol system, for the coating step.<sup>[19]</sup> The multi-polyol synthesis method used in this study solved the problems of low purity and CCN aggregation that we previously encountered.



**Scheme 4.1** Fabrication of the smooth, robust, and patternable CCN-based FTCEs via all-solution processes, including synthesis, coating, patterning, welding, and transfer. In the MDD, the flow speed of the upper layer was higher than that of the lower layer. This flow-speed difference (indicated by parallel arrows in solvent) caused the wires to form an orderly arrangement on the substrate.

The shape of the Cu NWs was clearly changed by controlling the reduction solvent types and ratio, as shown in Figures 4.1 and 4.2. With a single polyol, the precursors experienced the same reduction conditions, resulting in the atomic arrangement of symmetrical decahedron-shaped seeds with the effect of the salt ions, and grew in the  $[1\bar{1}0]$  direction, forming linear Cu NWs.<sup>[22–24]</sup> The dimensions of the Cu NWs clearly differed depending on the polyol types, because of the different reduction potentials arising from the variations in their molecular structures. From the SEM images, we infer that the polyol reducing ability at 198 °C decreased in the following order: GC > EG > diethylene glycol > PEG<sub>200</sub>. To observe the relevance of the Cu NW morphology and the co-reduction effect, various binary polyol systems were investigated, as shown in Figure 4.1. The GC/EG mixture was the only suitable synthesis condition for the CCNs. As previously reported, EG and GC reduce Cu<sup>+</sup>-amine ions, forming asymmetric decahedral multiply twin particles via the co-reduction effect and reduction-potential gap. Thus, they grow in the  $[1\bar{1}0]$  direction of curved structural NWs with plastic deformation due to partial line defects.<sup>[19, 25, 26]</sup> However, the low purity arising from the curved shape and the CCN aggregation are problems that must be addressed for the homogeneous distribution of CCNs in the coating process. Normally, the active peripheral

atoms, large surface area, and curved structure of CCNs yield a high surface energy.<sup>[19, 27]</sup> To reach a steady state, a passivation layer is usually formed on the CCN surface via reactions with negative elements and the adsorption of surfactants.<sup>[22, 28]</sup> Nevertheless, the dominant reduction condition and high reaction temperature in the synthesis process restrain the surface passivation, resulting in the easy aggregation of CCNs. In this study, we added PEG<sub>200</sub> to the EG/GC mixtures to significantly reduce the surface energy of the CCNs and prevented aggregation by controlling the CCN dimensions. Furthermore, the partially mild reduction condition due to the PEG<sub>200</sub> altered the asymmetric degree of Cu seeds, enhancing the purity of the CCNs. Figure 4.2 clearly shows the morphological changes arising from different mixing ratios of GC, EG and PEG<sub>200</sub>. In the optimal condition of 15 mL of EG, 10 mL of GC, and 5 mL of PEG<sub>200</sub>, the PEG<sub>200</sub> was well blended with the GC and EG, which allowed the easy preparation of multiple highly asymmetric decahedral Cu seeds, yielding high-purity CCNs with good curvature. However, with excessive amounts of PEG<sub>200</sub>, the CCNs lost their curved structure because the mild reductant PEG<sub>200</sub> was dominant in the ternary polyol system, reducing the asymmetry of the Cu seeds. Figure 4.3 shows SEM images and XRD spectra of the synthesized CCNs. In the SEM images, an average width of 65 nm and length of 25  $\mu$ m

were measured for dozens of randomly selected, highly curved Cu NWs (Figure 4.3a–c). In the XRD patterns of the CCNs (Figure 4.3d), the three characteristic peaks at  $2\theta = 43.5^\circ$ ,  $50.7^\circ$ , and  $74.4^\circ$  are assigned to the typical {111}, {200}, and {220} planes, respectively, of face-centered cubic Cu (JCPDS #03-1018), indicating a pure phase. The absorption peak of the CCNs was located at 573 nm, owing to the surface plasma resonance caused by the oscillation of free electrons in the conduction band.

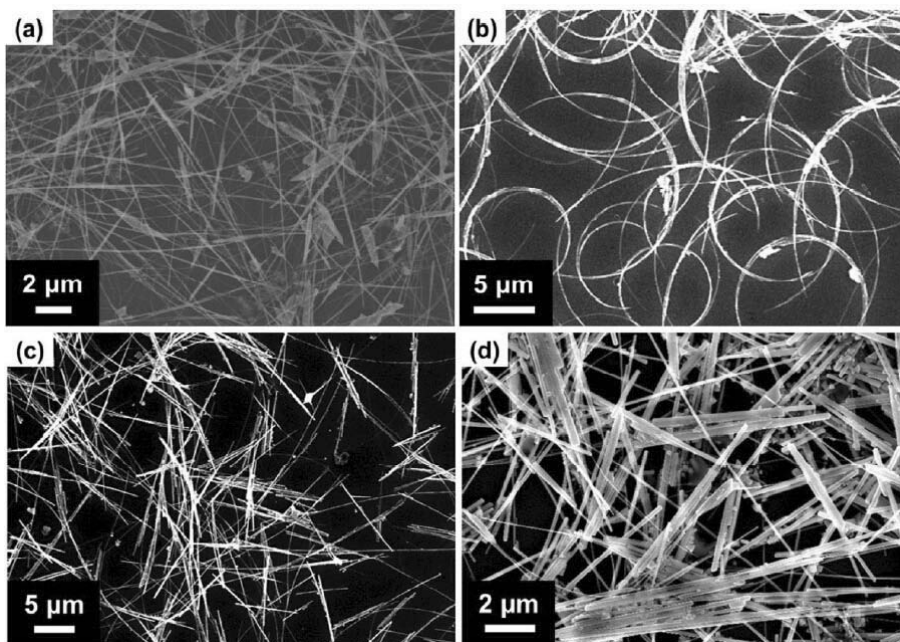


**Figure 4.1** SEM images of copper nanowires synthesized by different binary solvents. (a) 10 mL GC and 20 mL DEG, (b) 10 mL GC and 20 mL EG, (c) 10 mL PEG<sub>200</sub> and 20 mL EG, (d) 10 mL PEG<sub>400</sub> and 20 mL EG.

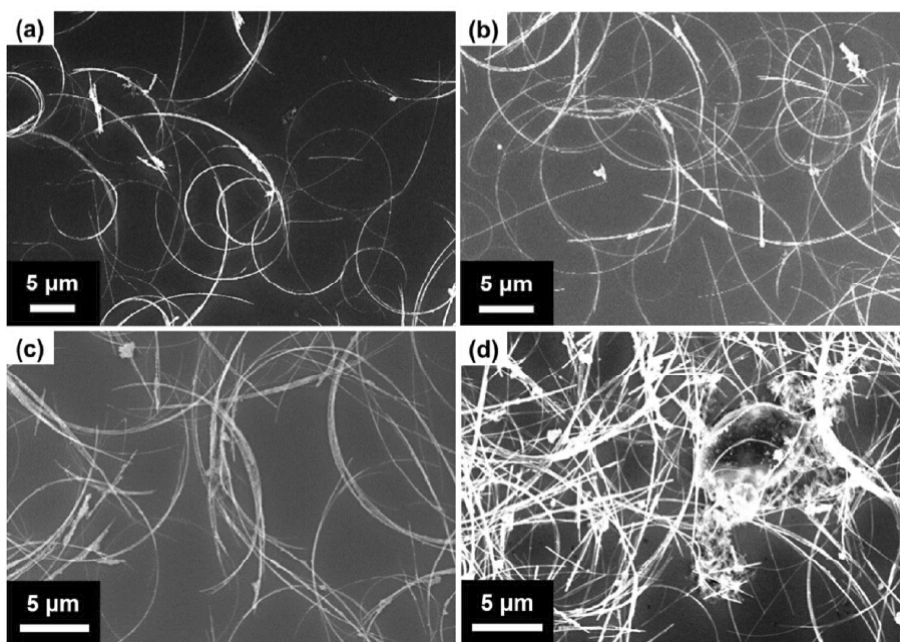


**Figure 4.2** SEM images of copper nanowires synthesized by different ratio of mixed polyol solvents. (a) 2.5 mL PEG<sub>200</sub>, 10 mL GC and 17.5 mL EG, (b) 5 mL PEG<sub>200</sub>, 10 mL GC and 15 mL EG, (c) 7.5 mL PEG<sub>200</sub>, 10 mL GC and 12.5 mL EG, (d) 10 mL PEG<sub>200</sub>, 10 mL GC and 10 mL EG.

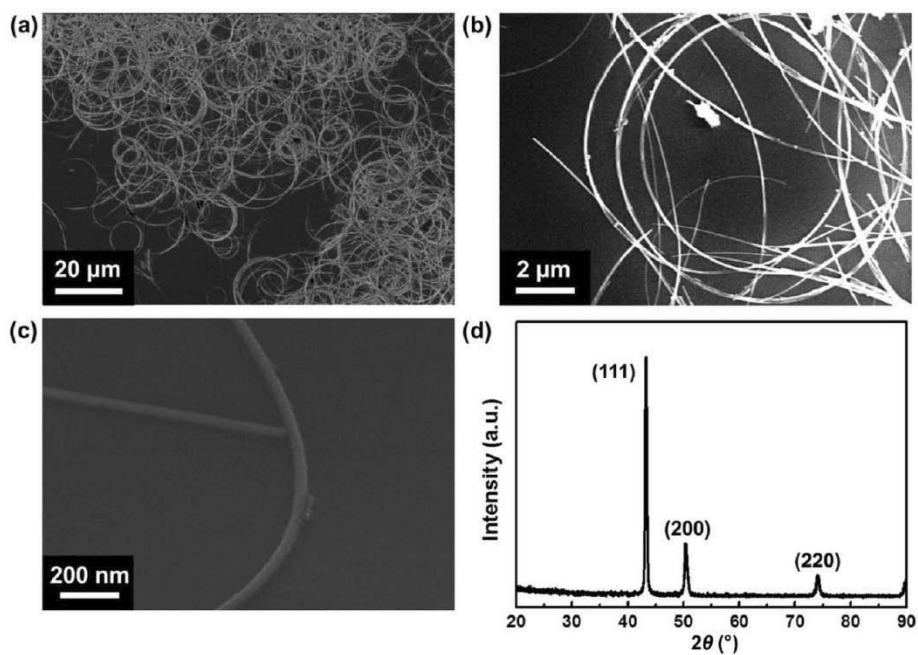


**Figure 4.3** Representative (a–c) SEM and (d) XRD images of CCNs synthesized with the optimal ratio of 15 mL of EG, 10 mL of GC, and 5 mL of PEG<sub>200</sub>.

### 4.3.2 Coating process

After the synthesis process, the CCNs were preserved and well dispersed in cyclohexane, as shown in Scheme 4.1. Generally, the dispersion of NWs is strongly related to the compatibility, polarity, and viscosity of the dispersible solvent.<sup>[29]</sup> Although cyclohexane has a weak polarity, its viscosity is more than three times that of n-hexane. This is attributed to the ring structure of the molecule, which causes CCNs to be well dispersed. More importantly, the alkyl chains in cyclohexane induce a high hydrophobicity, which is compatible with oleylamine-capped CCNs deposited on a PI film. Moreover, the high vapor pressure of the solvent is suitable for solvent-volatilization coating methods, such as spin coating, wire-wound coating, spray coating, dip coating, convective assembly, and MDD. However, when applied over a large area, spin coating and wire-wound coating place limitations on the uniformity and efficiency of alignment. Furthermore, dip coating, spray coating, and convective assembly involve large consumption of materials and extremely long operation times. Therefore, we proposed a simple MDD method for the uniform, rapid, cost-effective, and large-area coating of CCNs on the PI substrate. The detailed process characteristics are shown in Table 4.1.<sup>[30–37]</sup>

The commercial PI film is typically applied to actual devices via the roll-to-roll process because of its high glass transition temperature and outstanding flexibility.

When the CCNs/cyclohexane dispersion was injected between the PI substrate and the deposition plate, a meniscus of dispersion was quickly formed by the capillary action of the cyclohexane. The linear back-and-forth motion of the deposition plate dragged the liquid meniscus onto the PI substrate, and the CCNs were efficiently aligned through the shear gradient of fluid,<sup>[30, 38]</sup> as shown in the coating process depicted in Scheme 4.1. Because the shear gradient of fluid was due to the linear motion of the deposition plate, we selected  $40 \text{ mm}\cdot\text{s}^{-1}$  as the optimal coating speed for the efficient alignment of the CCN thin film. Furthermore, the aspect ratio of the NWs is an important factor for efficient coating. When the CCN length exceeds  $20 \text{ }\mu\text{m}$ , the CCNs are arranged on PI substrate in an orderly manner, parallel to the dragging direction, because NWs with a high aspect ratio are more likely to be significantly influenced by the shear gradient of fluid. The solvent properties also contributed to the uniformity of the films. Because cyclohexane has the novel properties of a high volatility, low surface tension, and low viscosity, the solvent was quickly evaporated before disrupting the CCN alignment via Brownian motion. For this reason, the

CCNs/cyclohexane dispersion can be easily applied for the MDD method to form a complete CCN network with any substrate, such as PET, glass, silicon wafers, or PI. In addition, the solvent-receding flow that occurred during the evaporation had little impact on the CCN alignment, owing to the pinning force acting on the CCNs at the edge of the liquid film.<sup>[38]</sup> Therefore, the film size was easily controlled by changing the width of the deposition plate, as shown in Figure 4.4a. To acquire the parameters related to the film-thickness control, it is important to consider the bond number (Bo) and capillary number (Ca). According to previous research, these are calculated using the following equations

$$\text{Bo} = \frac{\rho g r^2}{\gamma}$$

$$\text{Ca} = \frac{\mu U}{\gamma}$$

Where,  $\rho$  is the density of the coating fluid,  $g$  is the gravitational acceleration,  $r$  is the radius of the fluid meniscus,  $\mu$  is the viscosity of the fluid,  $U$  is the speed of the linear back-and-forth motion of the coating plate, and  $\gamma$  is the surface tension of the fluid. In this study, a low bond number ( $\sim 0.046$ ) and a low capillary number ( $\sim 0.00147$ ) caused the cylindrical meniscus to spread between the plate and substrate, which is similar to previous process characteristics, as illustrated in coating process of Scheme

4.1. Considering these low dimensionless numbers, the film thickness strongly depended on the number of coatings (NC), deposition number (DN), deposition speed (DS), and CCN concentration.<sup>[30, 31, 39–41]</sup> The DS and DN were fixed at  $40 \text{ mm}\cdot\text{s}^{-1}$  and 10, respectively, for efficient alignment and coverage. A CCN concentration of  $1.5 \text{ mg}\cdot\text{mL}^{-1}$  was employed for comparison with previous reports, as the transmittance range of the CCNs was 75%–90% at different NCs (Figure 4.4b). By controlling these parameters, uniform and efficient connected CCNs were obtained, as evidenced by OM and SEM (Figures 4.4c and d).

	Coating time	Uniform large area	Material consumption	Align
Spin-coating	Short	X	High	X
Wire-wound coating	Short	O	Low	X
Spray-coating	Long	O	Low	X
Dip-coating	Short	O	High	O
Convective assembly	Long	O	Low	O
Meniscus-dragging deposition	Short	O	Low	O

**Table 4.1** Process characteristics of various solution processes for thin film coating.

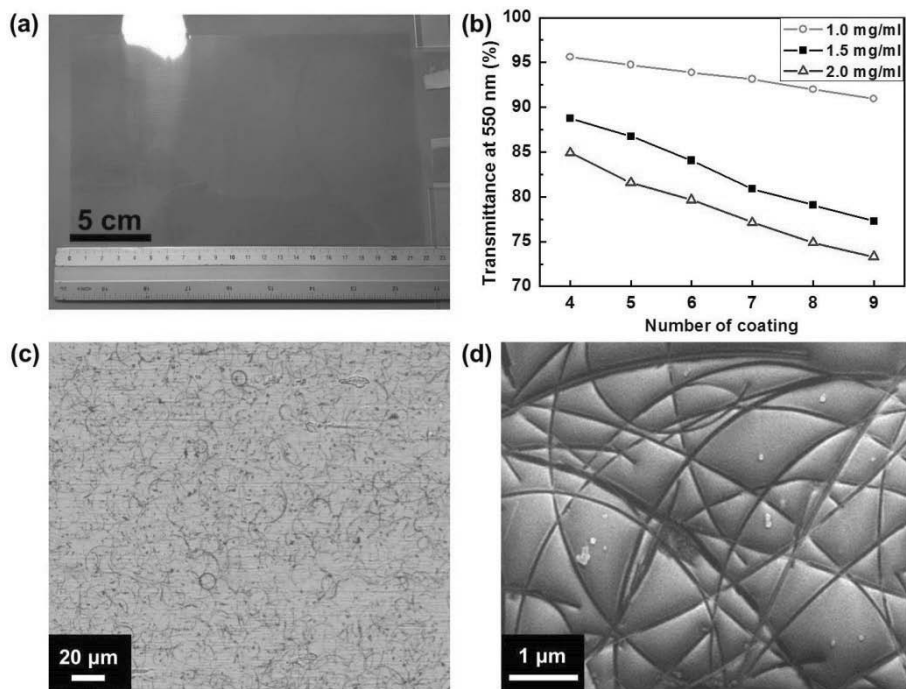


**Figure 4.4** (a) Large-scale coating of the CCNs on the PI film. (b) Control of the transmittance according to the coating conditions in the MDD. (c) OM and (d) SEM images of uniformly coating the CCNs on the PI film.

### 4.3.3 Patterning process

According to the device requirements, different patterning shapes and dimensions must be produced.<sup>[2, 13]</sup> Therefore, we proposed a feasible method for 20- $\mu\text{m}$  patterning in the CCN-based FTCE fabrication (Scheme 4.1). The proposed PU-stamped patterning method was used to remove the contact parts of the CCNs from the PI substrate by embedding them in pre-cured PU. To fabricate the line-space pattern on the PU, urethane liquid monomers were cured at 40 °C on the patterned PDMS substrate. After 5 h of pre-curing, the reverse-patterned PU mold was fully formed and stamped on the CCN thin film (77.26%  $T$  of sample before washing) on the PI substrate. As a result, the unwelded NWs were embedded into the convex parts of the PU mold, forming the same line-space patterns on the CCN thin films as those on the PDMS mold.

#### 4.3.4 Welding process

In addition to the random distribution, the contact resistance in the junctions is another significant factor affecting the optoelectrical performance of metal NW thin films.<sup>[22, 27, 42]</sup> The network of CCNs can be divided between percolation-type and contact-type.<sup>[21, 43, 44]</sup> Generally, thermal-sintering methods are applied under reducing-gas conditions to remove the oxide layer and improve the electrical properties via the deep percolation of NWs.<sup>[21, 45]</sup> However, vacuum facilities and harsh conditions are often needed to prevent oxidation and connect the NW junctions, which make continuous manufacturing difficult. Washing methods involve removing the oxide layer for the direct contact of NWs through chemical reactions with the solvent.<sup>[19, 46]</sup> Unfortunately, the secondary oxidation on the junction parts caused by exposure to air degrades the electrical performance of the contact-type CCNs. Recently, light irradiation—as a photonic welding method—was reported to effectively percolate metal NWs under ambient conditions.<sup>[47]</sup> However, the pulse controllers in light-irradiation systems are unsuitable for widespread use, owing to the precise production required for the delivery of a high electrical current in milliseconds.

To overcome this critical drawback, we proposed an effective strategy of solvent-dipped welding for improving the electrical performance. The natural oxide layer on the CCN surface was removed via the reduction reaction when the PEG<sub>200</sub> was heated to 200 °C and maintained for 30 min (Scheme 4.1 and Figure 4.5). Then, the CCN thin film was gradually conducted and exhibited the best electrical properties with the contact-type CCN connection. For a completely percolated NW connection, a low pressure of 0.3 N·cm<sup>-2</sup> was applied for the welding of the NWs in order to reduce the contact resistance while the NWs were immersed and annealed in PEG<sub>200</sub> at 200 °C. The PEG<sub>200</sub> not only protected the CCNs from oxidation during the welding process but also formed a thin liquid film between the weight and the CCNs to prevent scratches due to direct contact. SEM and HR-TEM were performed to observe the percolated CCN network after the solvent-dipped welding process. The randomly distributed and intact NW network is clearly observed in Figures 4.6a and b. During thermal treatment above 150 °C, the surface atoms of the Cu NWs became sufficiently active to be welded.<sup>[48]</sup> Although the annealing process provided enough energy for the welding of CCNs, the buoyancy of the solvent and the solvent layer in the junctions were critical obstacles. Thus, an auxiliary pressure of 0.3 N·cm<sup>-2</sup> was applied to reduce the force of buoyancy and

minimize the gap of CCNs, similar to an Ohmic contact.<sup>[49]</sup> In this condition, the active atoms overcame the gap of the NW contact point and were connected to the metallic bonding, which was further integrated by completely crystalline Cu. The atomic arrangement of the welding parts followed the (111) planes of NW1 and NW2, which maintained their original lattice spacing and crystal orientation (Figures 4.6c and d). However, the fringe lattice spacing on the (200) and (220) planes was stretched to 0.36 nm with the gradual rotation of the crystal orientation, because of the metallic bonding in the cross-sectional junction (Figure 4.6d). The different live fast Fourier transform (FFT) patterns for NW1, NW2, and the welded junction, as well as a corresponding schematic image, are shown in Figure 4.7. According to the FFT analysis, the patterns for NW1 and NW2 exhibit two typical cases of the CCNs, which are attributed to perpendicular and parallel beams on an exposed plane, respectively.<sup>[8]</sup> In addition, the welded parts exhibited new complete patterns according to the welding mechanism—not the overlapping patterns of NW1 and NW2.

After the welding was complete, the CCN thin films were washed with acetone to remove the residual PEG<sub>200</sub> and unconnected NWs. This enhanced the transmittance, as shown in Figure 4.8a. As previously reported, GC with a high viscosity requires considerable solvent consumption for the

complete removal of the residue in the washing process. Therefore, PEG<sub>200</sub>, which has a relatively low viscosity, was used for the reduction of the CCNs and better removal of the residue. The CCN thin films fabricated in this study had excellent electrical properties and a high transparency, as shown in Figure 4.8b ( $R_s = 21.15 \Omega \cdot \square^{-1}$  at 80.88%  $T$ ;  $R_s = 35.68 \Omega \cdot \square^{-1}$  at 82.51%  $T$ ;  $R_s = 47.30 \Omega \cdot \square^{-1}$  at 84.59%  $T$ ;  $R_s = 65.72 \Omega \cdot \square^{-1}$  at 86.80%  $T$ ;  $R_s = 82.71 \Omega \cdot \square^{-1}$  at 89.45%  $T$ ;  $R_s = 132.59 \Omega \cdot \square^{-1}$  at 91.01%  $T$ ). Additionally, compared with other FTCEs, the proposed CCN thin films yielded high optoelectrical performance.<sup>[13, 19, 32, 50, 51]</sup> We selected the 84.59%  $T$  film as a standard sample to perform systematic experiments. The solvent-dipped welding improved the oxidation stability of the CCN thin film, and Figure 4.8c shows the relative-resistance change ( $R/R_0$ ) over 10 days of exposure to air. The  $R/R_0$  of the reduced CCN thin films without any pressure was dramatically increased to 1.17, owing to the secondary oxidation on the junctions. Compared with the reduced film, the CCNs percolated via solvent-dipped welding merged, forming a complete crystal structure with the junction gaps removed, which not only reduced the contact resistance but also prevented oxidation. Nevertheless, the  $R/R_0$  of the welded CCN thin film was slightly increased (< 5%) by the natural oxidation on the surface of the CCN films.

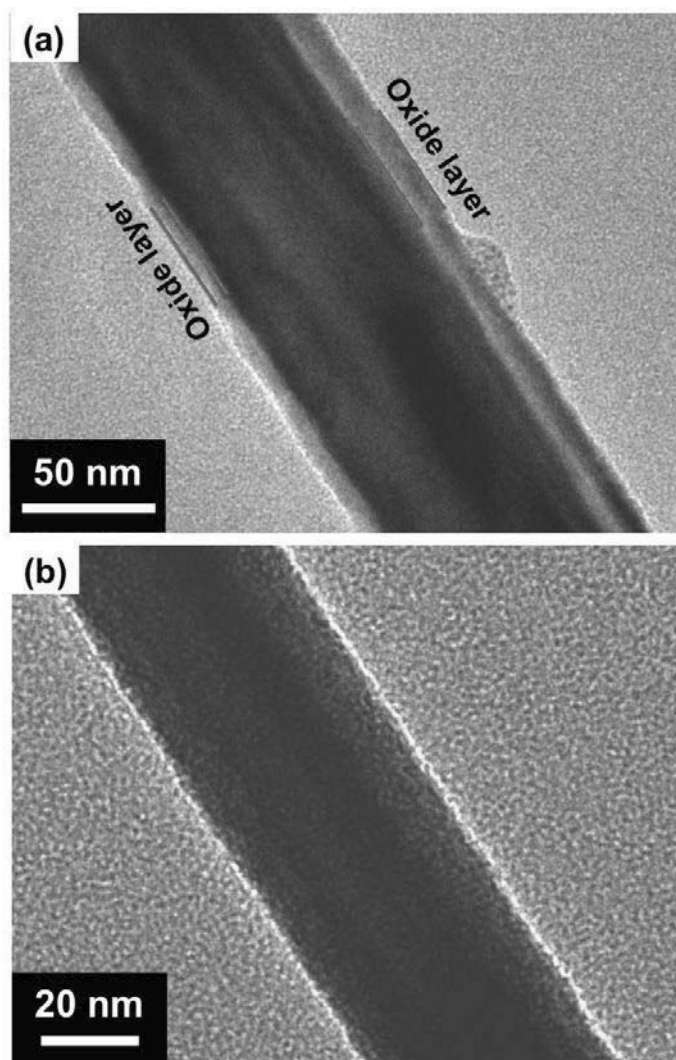


**Figure 4.5** (a) TEM image of the CCN with 4–10 nm of natural oxide layer when preserved after 2 days. (b) TEM image of the CCN after PEG<sub>200</sub>-dipped reduction process at 200 °C for 30 min.

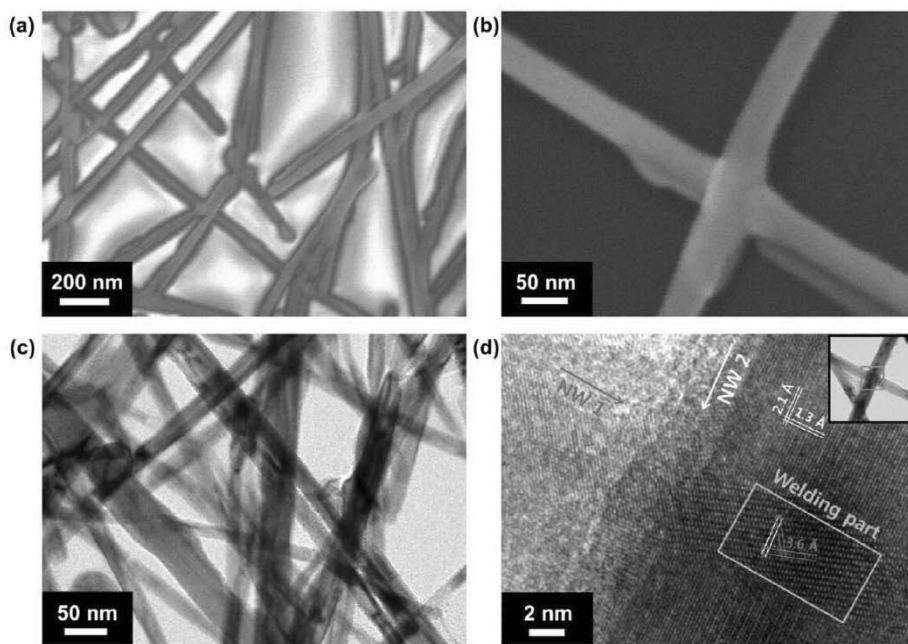


**Figure 4.6** (a, b) SEM and (c, d) HR-TEM images of the percolated CCN network formed via the solvent-dipped welding method.

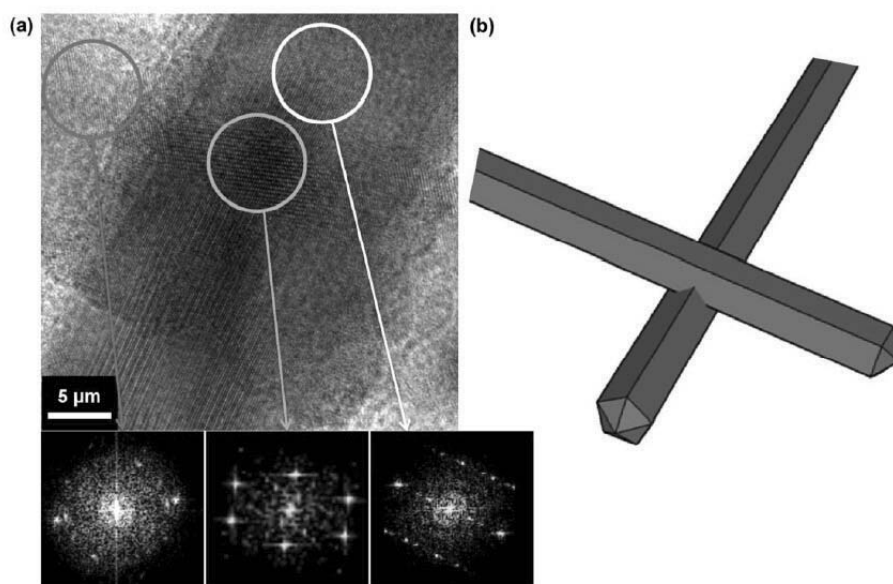


**Figure 4.7** (a) HR-TEM image and live FFT patterns of welded CCNs. (b) Corresponded schematic image of welding.

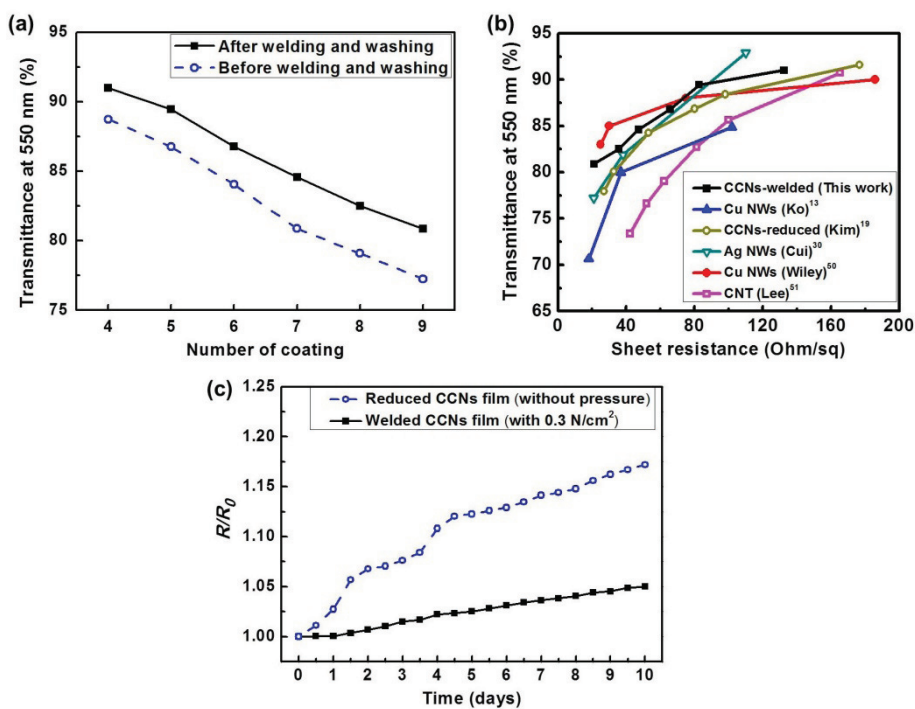


**Figure 4.8** (a) Transmittance of CCN thin films under various coating conditions before and after washing. (b) Plot of the transmittance at 550 nm vs. the sheet resistance for CCN thin films on the PI substrate and comparison with other groups. (c) Oxidation stability of the CCN thin films before and after welding within 10 days.

### 4.3.5 Transfer process

Although the CCN thin films exhibited high optoelectrical performance, the critical technical problem of the high surface roughness was unsolved for the CCNs deposited on the PI substrate. Furthermore, the PI substrate has low transparency for use in optical-device fabrication. To overcome this roughness issue, we proposed a PU-embedded transfer method, as illustrated in Scheme 4.1. The liquid monomers of the PU elastomer were mixed and coated on a flexible transparent substrate. After 10 h of pre-curing at 40 °C, another 30 min of pressing was applied to the PU-contacted CCN thin for a successful transfer. The PU matrix was peeled from the flexible transparent substrate when the PU was perfectly cured (Scheme 4.1). The transfer method involved partially embedding the CCN thin film into the pre-curing PU substrate by controlling the pre-curing time, pressure, and pressing time (Figure 4.9). Therefore, the embedding depth depended on the hardness of the PU matrix, the parallel force acting in the embedding direction, and the retention time of the exerted force. Furthermore, the pre-curing PU matrix exhibited strong adhesion and a large curing force, completing the transfer of the CCNs. The aforementioned patterning process was implemented using the same method. Through the observation

of  $R/R_0$  with the adjustment of several experimental conditions, the optimal transfer conditions were determined as follows: a pre-curing time of 10 h, pressure of  $0.12 \text{ N}\cdot\text{cm}^{-2}$ , and pressing time of 30 min (Figures 4.9a–c). Different experimental conditions with fine-tuning yielded similar results, allowing short-time consumption and room-temperature fabrication.

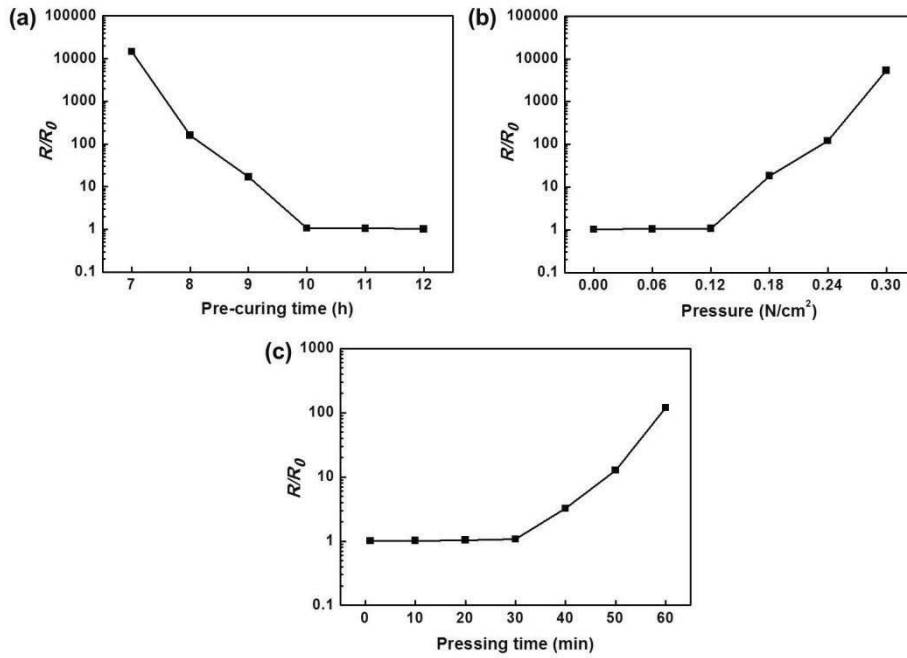


**Figure 4.9** Relative resistance ( $R/R_0$ ) of CCN thin films after transfer to the PU matrix with (a) different pre-curing times at a pressure of  $0.12 \text{ N}\cdot\text{cm}^{-2}$  and a pressing time of 30 min, (b) different pressures at a pre-curing time of 10 h and a pressing time of 30 min, and (c) different pressing times at a pre-curing time of 10 h and a pressure of  $0.12 \text{ N}\cdot\text{cm}^{-2}$ .

### 4.3.6 Flexible transparent conductive electrode

The transmittance and sheet resistance of the CCN thin film were slightly enhanced after the transfer process because several unconnected CCNs remained owing to their strong bonds with the PI substrate. Typically, the CCN thin film partially embedded into the PU matrix exhibited a low sheet resistance of  $53.48 \Omega \cdot \square^{-1}$  at a high transparency of 85.71% and a low root-mean-square surface roughness ( $R_{rms}$ ) of 14.36 nm (Figures 4.10a and b). An AFM image showing the surface topography of a CCN-based FTCE for the full data range at  $15 \mu\text{m} \times 15 \mu\text{m}$  is presented in Figure 4.10b. The highly percolated CCN network was strongly grasped by the PU matrix, enhancing the robustness. To demonstrate the high adhesion resistance, the CCN-based FTCE was stuck to adhesive tape and peeled off 10 times. As shown in the inset images of Figure 4.10c, the CCN network was not removed from the PU matrix even after being peeled from the tape 10 times. However, a small fraction of the weak NWs or partially welded junctions was unable to endure the adhesion force and broke during the repeated tape testing. Although the  $R/R_0$  increased slightly with the successive tape tests, it remained below 1.10 at the 10<sup>th</sup> peeling repetition, indicating sufficient mechanical stability against adhesion (Figure 4.10c). More interestingly,

this fabrication method for FTCEs was also applied to a patterned CCN thin film through the aforementioned patterning process. The OM images shown in Figure 4.10d clearly indicate the 20- $\mu\text{m}$  line-space patterned CCN network (80.88% *T* of sample, after washing) partially embedded into the PU substrate through the consecutive processes of synthesis, coating, patterning, welding, and transfer.

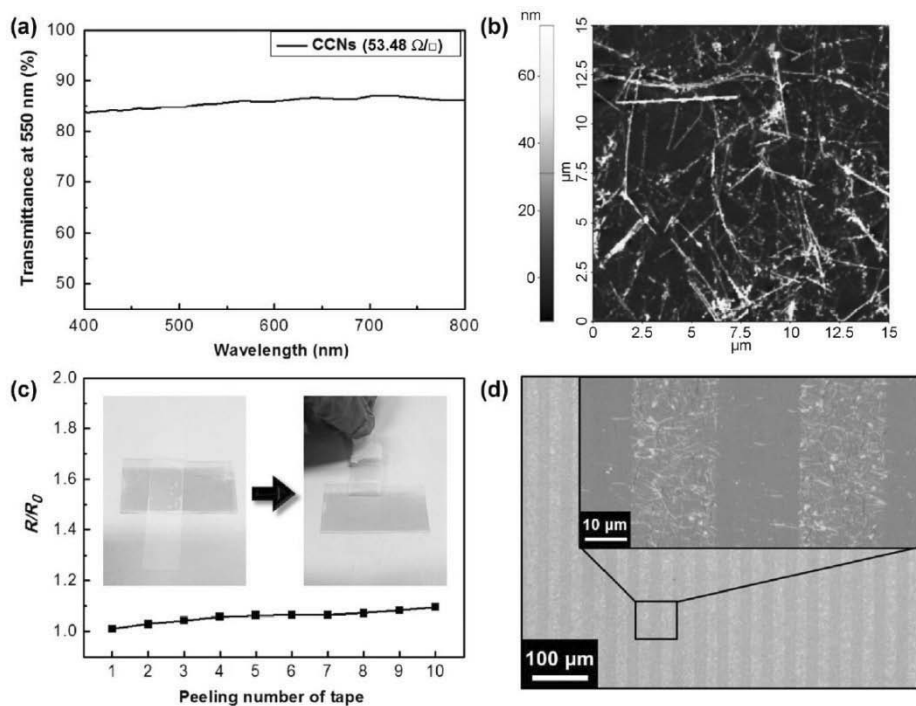


**Figure 4.10** (a) UV-vis transmission spectrum and (b) AFM image of the CCN thin film ( $T = 85.71\%$ ,  $R_s = 53.48 \Omega \cdot \square^{-1}$ , and  $R_{rms} = 14.36 \text{ nm}$ ) on a PU matrix. (c) Relative resistance of the CCN thin film embedded on the PU matrix with 10 tape-peeling repetitions. (d) OM images of a 20- $\mu\text{m}$  line-space patterned CCN thin film (80.88%  $T$  of the sample, after washing) embedded on a PU matrix.

The smooth, robust, and patternable FTCE was finally completed using the all-solution method and exhibited an excellent transparency, a low sheet resistance, and high flexibility (Figure 4.11a). To understand the relationship between the electrical performance and the flexibility, the CCNs/PU composites on the PET substrate were investigated using a self-designed bending machine. The bending-motion speed was fixed at  $50 \text{ mm}\cdot\text{s}^{-1}$  for a 5-mm bending radius and 1 to 1,000 bending cycles. Normally, the CCNs/PU composites were freestanding after being peeled from the flexible transparent substrate (Scheme 4.1). However, the PU was not suitable for repeated flexibility tests, because its high elastic modulus easily induced plastic deformation. Therefore, PET, which has a relatively low elastic modulus, was used as a supporting substrate to enhance the flexibility for a successful test. Figure 4.11b shows the resistance change that occurred when the CCN-based FTCE was bent with radii of 20, 15, 10, and 5 mm in the first cycle. According to previous research, CCN thin films on a PET substrates exhibit a very small resistance change under tensile or compressive bending owing to their self-bendable structure and high softness. However, in the present study, the variation in  $R/R_0$  increased to 1.85 and 2.13 under tensile and compressive bending, respectively, with a bending radius of 5 mm. In the absence of the PU matrix that immobilized

the CCNs, the free space was sufficient to release the bending strain by extending the curved shape of NWs and the random network structure of the FTCE. In contrast, when the CCN film was partially embedded into the PU matrix, the bending of the FTCE deformed the surface area of the PU matrix with the fixed CCNs, maintaining the neutral axis of the matrix. The strain of the entire film was uniformly diffused by the stretching of the PU matrix, and it was difficult to expand the curved shape of the NWs efficiently and the random network of the electrode, resulting in a decrease of the CCN concentration and a decrease of the current density in some regions. Therefore, the  $R/R_0$  changed significantly during the bending process, especially at a high transparency. Although the homogeneous stress induced by the PU matrix obstructed the release of the curved shape, the structural advantages of the CCNs were observed in the bending tests. As shown in Figure 4.11c, the change in  $R/R_0$  was negligible ( $< 1.02$ ) after 1,000 cycles of tensile bending, indicating that the CCN-based FTCEs were highly mechanically stable against the bending.

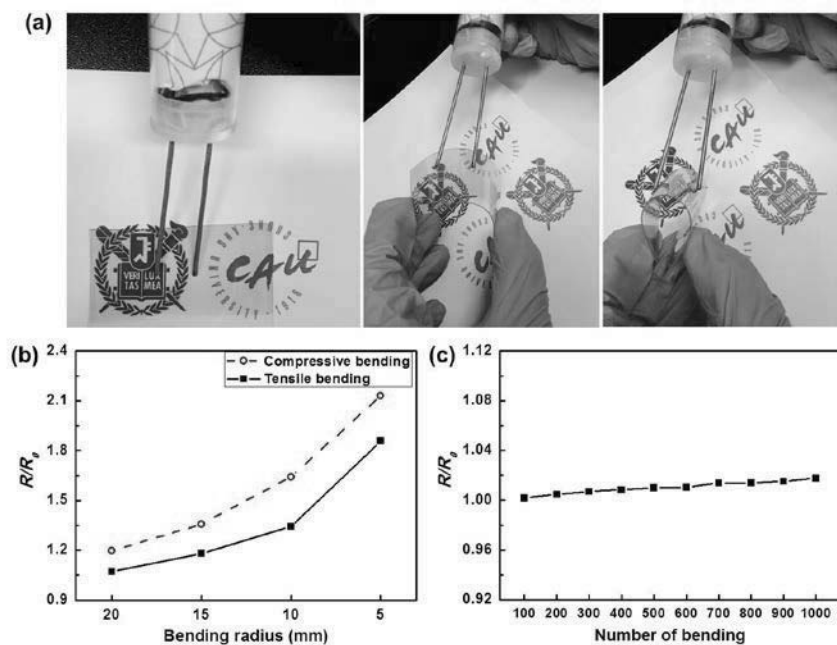


**Figure 4.11** (a) Lighting images of a light-emitting diode connected by the CCN thin film ( $T = 85.71\%$ ,  $R_s = 53.48 \Omega \cdot \square^{-1}$ ) on PU/PET with an external power supply. The relative resistance of the CCN thin film partially embedded into the PU/PET under bending with radii of (b) 20, 15, 10, and 5 mm and (c) the cycling number of the bending with a 5-mm radius.

## 4.4 Conclusion

We demonstrated a fully solution-processed approach for fabricating robust and patternable CCN-based FTCEs using self-designed innovative techniques, such as multi-polyol synthesis, MDD, PU-stamped patterning, solvent-dipped welding, and PU-embedded transfer. Furthermore, a combination of these methods solved the technical problems faced in the manufacturing of Cu NW-based FTCEs, such as the difficulty of patterning, low robustness, and high roughness. As a prospective FTCE, a uniform and highly percolated CCN thin film embedded on a PU matrix exhibited excellent optoelectrical performance ( $R_s = 53.48 \Omega \cdot \square^{-1}$  at  $T = 85.71\%$ ) and high mechanical stability ( $R/R_0 < 1.02$  at 1,000<sup>th</sup> bending cycle and  $R/R_0 < 1.10$  at 10<sup>th</sup> repetition of tape peeling), along with a low surface roughness ( $R_{rms} = 14.36$  nm). The proposed CCN-based FTCEs are applicable for many advanced flexible electronics.

## References

- [1] S. Ye, A. R. Rathmell, Z. Chen, I. E. Stewart, B. J. Wiley, *Adv. mater.* **2014**, *26*, 6670.
- [2] Z. Zhong, K. Woo, I. Kim, H. Hwang, S. Kwon, Y.-M. Choi, Y. Lee, T.-M. Lee, K. Kim, J. Moon, *Nanoscale* **2016**, *8*, 8995.
- [3] J. Lee, P. Lee, H. B. Lee, S. Hong, I. Lee, J. Yeo, S. S. Lee, T.-S. Kim, D. Lee, S. H. Ko, *Adv. Funct. Mater.* **2013**, *23*, 4171.
- [4] C. Mayousse, C. Celle, A. Carella, J. Simonato, *Nano Res.* **2014**, *7*, 315.
- [5] S. Li, Y. Chen, L. Huang, D. Pan, *Inorg. Chem.* **2014**, *53*, 4440.
- [6] D. S. Hecht, L. Hu, G. Irvin, *Adv. Mater.* **2011**, *23*, 1482.
- [7] J. H. Lee, D. W. Shin, V. G. Makotchenko, A. S. Nazarov, V. E. Fedorov, Y. H. Kim, J. Y. Choi, J. M. Kim, J. B. Yoo, *Adv. Mater.* **2009**, *21*, 4383.
- [8] W. Zhang, Z. Yin, A. Chun, J. Yoo, Y. S. Kim, Y. Piao, *ACS Appl. Mater. Interfaces* **2016**, *8*, 1733.
- [9] J. T. Robinson, F. K. Perkins, E. S. Snow, Z. Q. Wei, P. E. Sheehan, *Nano Lett.* **2008**, *8*, 3137.
- [10] D. T. Pham, T. H. Lee, D. H. Luong, F. Yao, A. Ghosh, V. T. Le, T. H. Kim, B. Li, J. Chang, Y. H. Lee, *ACS Nano* **2015**, *9*, 2018.
- [11] H.-J. Peng, J.-Q. Huang, M.-Q. Zhao, Q. Zhang, X.-B. Cheng, X.-Y. Liu, W.-Z. Qian, F. Wei, *Adv. Funct. Mater.* **2014**, *24*, 2772.
- [12] Y. Kim, T. I. Ryu, K. Ok, M. Kwak, S. Park, N. Park, C. J. Han, B. S. Kim, M. J. Ko, H. J. Son, J. Kim, *Adv. Funct. Mater.* **2015**, *25*, 4580.
- [13] S. Han, S. Hong, J. Ham, J. Yeo, J. Lee, B. Kang, P. Lee,; J. Kwon, S. S. Lee, M.-Y. Yang, S. H. Ko, *Adv. Mater.* **2014**, *26*, 5808.
- [14] H.-G. Im, S.-H. Jung, J. Jin, D. Lee, J. Lee, D. Lee, J.-Y. Lee, I.-D. Kim, B.-S. Bae, *ACS Nano* **2014**, *8*, 10973.
- [15] W. Hu, R. Wang, Y. Lu, Q. Pei, *J. Mater. Chem. C* **2014**, *2*, 1298.
- [16] S. Nam, M. Song, D.-H. Kim, B. Cho, H. M. Lee, J.-D. Kwon, S.-G.

- Park, K.-S. Nam, Y. Jeong, S.-H. Kwon, Y. C. Park, S.-H. Jin, J.-W. Kang, S. Jo, C. S. Kim, *Sci. Rep.* **2014**, *4*, 4788.
- [17] A. R. Rathmell, B. J. Wiley, *Adv. Mater.* **2011**, *23*, 4798.
- [18] C. R. Chu, C. Lee, J. Koo, H. M. Lee, *Nano Res.* **2016**, *9*, 2162.
- [19] Z. Yin, S. K. Song, D. J. You, Y. Ko, S. Cho, J. Yoo, S. Y. Park, Y. Piao, S. T. Chang, Y. S. Kim, *Small* **2015**, *11*, 4576.
- [20] S. Ding, J. Jiu, Y. Gao, Y. Tian, T. Araki, T. Sugahara, S. Nagao, M. Nogi, H. Koga, K. Suganuma, H. Uchida, *ACS Appl. Mater. Interfaces* **2016**, *8*, 6190.
- [21] D. Zhang, R. Wang, M. Wen, D. Weng, X. Cui, J. Sun, H. Li, Y. Lu, *J. Am. Chem. Soc.* **2012**, *134*, 14283.
- [22] Z. Yin, C. Lee, S. Cho, J. Yoo, Y. Piao, Y. S. Kim, *Small* **2014**, *10*, 5047.
- [23] H. Z. Guo, Y. Z. Chen, H. M. Ping, J. R. Jin, D.-L. Peng, *Nanoscale* **2013**, *5*, 2394.
- [24] H. Z. Guo, Y. Z. Chen, M. B. Cortie, X. Liu, Q. S. Xie, X. Wang, D.-L. Peng, *J. Phys. Chem. C* **2014**, *118*, 9801.
- [25] Y. J. Zhan, Y. Lu, C. Peng, J. Lou, *J. Cryst. Growth* **2011**, *325*, 76.
- [26] L. Zhou, X.-F. Fu, L. Yu, X. Zhang, X.-F. Yu, Z.-H. Hao, *Appl. Phys. Lett.* **2009**, *94*, 153102.
- [27] S. Bhanushali, P. Ghosh, A. Ganesh, W. Cheng, *Small* **2015**, *11*, 1232.
- [28] A. R. Rathmell, M. Nguen, M. Chi, B. J. Wiley, *Nano Lett.* **2012**, *12*, 3193.
- [29] G. Christensen, H. Younes, H. Hong, P. Smith, *J. Appl. Phys.* **2015**, *118*, 214302.
- [30] Y. Ko, S. K. Song, N. H. Kim, S. T. Chang, *Langmuir* **2016**, *32*, 366.
- [31] Y. U. Ko, S.-r. Cho, K. S. Choi, Y. Park, S. T. Kim, N. H. Kim, S. Y. Kim, S. T. Chang, *J. Mater. Chem. C* **2012**, *22*, 3606.
- [32] L. Hu, H. S. Kim, J. Lee, P. Peumans, Y. Cui, *ACS Nano* **2010**, *4*, 2955.
- [33] T. Kitano, Y. Maeda, T. Akasaka, *Carbon* **2009**, *47*, 3559.
- [34] S. Park, G. Pitner, G. Giri, J. H. Koo, J. Park, K. Kim, H. Wang, R.

- Sinclair, H.-S. P. Wong, Z. Bao, *Adv. Mater.* **2015**, *27*, 2656.
- [35] D. Y. Choi, H. W. Kang, H. J. Sung, S. S. Kim, *Nanoscale* **2013**, *5*, 977.
- [36] E. Y. Jang, T. J. Kang, H. W. Im, D. W. Kim, Y. H. Kim, *Small* **2008**, *4*, 2255.
- [37] S. K. Duan, Q. L. Niu, J. F. Wei, J. B. He, Y. A. Yin, Y. Zhang, *Phys. Chem. Chem. Phys.* **2015**, *17*, 8106.
- [38] H. Dai, R. Ding, M. Li, J. Huang, Y. Li, M. Trevor, *Sci. Rep.* **2014**, *4*, 6742.
- [39] Y. Ko, N. H. Kim, N. R. Lee, S. T. Chang, *Carbon* **2014**, *77*, 964.
- [40] L. Landau, B. Levich, *Acta Physicochim. URSS* **1942**, *17*, 42.
- [41] D. White, J. Tallmadge, *Chem. Eng. Sci.* **1965**, *20*, 33.
- [42] R. Wang, H. Zhai, T. Wang, X. Wang, Y. Cheng, L. Shi, J. Sun, *Nano Res.* **2016**, *9*, 2138.
- [43] G.-H. Lim, N.-E. Lee, B. Lim, *J. Mater. Chem. C* **2016**, *4*, 5642.
- [44] J. Lee, I. Lee, T.-S. Kim, J.-Y. Lee, *Small* **2013**, *9*, 2887.
- [45] C. Sachse, N. Weiß, N. Gaponik, L. Müller-Meskamp, A. Eychmüller, K. Leo, *Adv. Energy Mater.* **2014**, *4*, 1300737.
- [46] Y. Won, A. Kim, D. Lee, W. Yang, K. Woo, S. Jeong, J. Moon, *NPG Asia Mater.* **2014**, *6*, e105.
- [47] H. Y. Yang, H.-W. Park, S. J. Kim, J.-M. Hong, T. W. Kim, D. H. Kim, J. A. Lim, *Phys. Chem. Chem. Phys.* **2016**, *18*, 4627.
- [48] H. Guo, N. Lin, Y. Chen, Z. Wang, Q. Xie, T. Zheng, N. Gao, S. Li, J. Kang, D. Cai, D.-L. Peng, *Sci. Rep.* **2013**, *3*, 2323.
- [49] Y. Tang, S. Gong, Y. Chen, L. W. Yap, W. Cheng, *ACS Nano* **2014**, *8*, 5707.
- [50] A. R. Rathmell, S. M. Bergin, Y.-L. Hua, Z.-Y. Li, B. J. Wiley, *Adv. Mater.* **2010**, *22*, 3558.
- [51] U. J. Kim, I. H. Lee, J. J. Bae, S. Lee, G. H. Han, S. J. Chae, F. Günes, J. H. Choi, C. W. Baik, S. Kim, J. M. Kim, Y. H. Lee, *Adv. Mater.* **2011**, *23*, 3809.

# **Chapter 5. Bridging Oriented Copper Nanowire-Graphene Composites for Solution-Processable, Annealing-Free, and Air-Stable Flexible Electrodes**

## **5.1 Introduction**

Solution-processable, flexible, and durable conductive electrodes have been widely researched because of the stringent requirements for the rapid development of wearable electronic devices, such as smart clothes, wearable energy-storage devices, and epidermal medical devices.<sup>[1, 2]</sup> Compared with conventional conducting electrodes, next-generation wearable electrodes must be designed for high electrical conductivity and mechanical durability under human motional deformation.<sup>[2-4]</sup> Currently, solution processes as one of best choices have been widely used in the fabrication of wearable devices because of their convenience and low cost.<sup>[5]</sup> <sup>6]</sup> In general, these novel electrodes have been based on polymers and carbon materials that can be directly knitted into different types of fabrics,

which has attracted interest from people. Recently, conductive fiber based poly(3,4-ethylenedioxythiophene) and poly-(styrenesulfonate) were prepared by the wet spinning method,<sup>[7]</sup> and these polymers were easily solution-processed into conductive fibers with good mechanical properties. However, these materials typically have low conductivity and poor durability, resulting in their limited application to wearable electronic devices. Therefore, how to decrease the electrical resistance of the fiber electrode is still a big challenge currently.<sup>[8, 9]</sup> Conductive carbon materials, such as carbon nanotubes and graphene, are viable for use as wearable electronics because of their low sheet resistance ( $\sim 1 \text{ } \Omega \cdot \square^{-1}$ ) and good mechanical properties. In spite of their processability and conductivity, the large-scale production of carbon nanomaterials requires a complicated process with a high cost.<sup>[10]</sup> Although many composites have been prepared to address these shortcomings,<sup>[11-13]</sup> their conductivities are still much lower than those of metals. To address the urgent requirements for high-performance electrical devices, much research effort is currently focused on areas such as low-cost manufacturing techniques and their application to cheap wearable electronics. Therefore, both academic and industrial laboratories are researching a solution-processable way to prepare conductive metal electrodes.<sup>[14]</sup>

To date, most solution-processable metallic electrodes reported are composed of conductive metallic nanoparticles (NPs) and nanowires (NWs) of silver or copper, which are promising for the development of wearable and portable electronics.<sup>[15, 16]</sup> These nanocomposite electrodes show low sheet resistance ( $\sim 0.01 \Omega \cdot \square^{-1}$ ), facile manufacturability, and superior mechanical performance compared to carbon, polymers, and other conductive materials.<sup>[17–19]</sup> Currently, Ag NW-based percolation networks have shown promise in flexible electronics.<sup>[2, 20]</sup> Although Ag NWs have excellent electrical conductivity and flexibility,<sup>[21]</sup> the scarcity and high cost of silver are difficult to address. Cu NWs with high-temperature treatment are as electrically conductive as Ag, and thus, Cu, which is cheaper, has gained more attention than Ag recently.<sup>[22–25]</sup> Our previous studies focused on the novel synthesis and low-temperature treatment of oxidation-resistant Cu NW electrodes by straightforward solution methods.<sup>[26, 27]</sup> Unfortunately, the excessive post-treatment process of Cu nanomaterials is still an obstacle for many applications for wearable electronics. In addition, the problems with Cu NWs, including easy oxidation and harsh preparation, must be resolved.

The invention of lightweight and wearable electrodes with a convergence of high conductivity, high machinability, and high flexibility with low cost

materials and scalable manufacturing processes is still a challenge.<sup>[28-30]</sup> In this work, we designed low-cost reduced graphene oxide (RGO)-Cu NW composite electrodes using a one-pot solvothermal method that led to high-performance flexible electrodes. After deposition on polyester cloths, the Cu NWs in the composites maintained their high intrinsic conductivity and flexibility, while the RGO nanosheets connecting the oriented Cu NWs not only provided remarkable pathways for charge transfer but also acted as an antioxidation layer to protect the Cu NWs from harsh environments.

## 5.2 Experimental section

### 5.2.1 Reagents

CuCl, NH<sub>4</sub>Cl, oleylamine, ethylene glycol (EG), and graphite (< 20 μm) were purchased from Sigma-Aldrich. All chemicals were of analytic grade and used as received without further purification. Deionized water was filtered by using a water-purification system (UP90 model, Seoul, South Korea). GO was prepared from graphite powder by an improved Hummers method.<sup>[31, 32]</sup>

### 5.2.2 Apparatus

Sample morphologies were characterized by field emission scanning electron microscopy (SEM, Hitachi S-4800). A transmission electron microscope (TEM) equipped with a field emission gun was used for HR-TEM measurements (JEOL, JEM-2010) at 200 kV. The powder X-ray diffraction spectra (XRD) were measured by XRD (Bruker, D8-Advance) with Cu K $\alpha$  radiation at  $\lambda = 1.542 \text{ \AA}$ .

### **5.2.3 Preparation of Cu NW-RGO composites**

Cu NW-RGO composites were successfully synthesized by the solvothermal method. Typically, CuCl (0.006 mol), GO (0.075 g), oleylamine (0.01 mol), and NH<sub>4</sub>Cl (0.001 mol) were dissolved in 0.1 L of EG by stirring for 2 h. Then, the mixture was sealed in a Teflon-lined autoclave and maintained at 180 °C for 10 h. When the synthesis was finished, the products were rapidly washed with hexane four times. Finally, the composite was preserved in hexane.

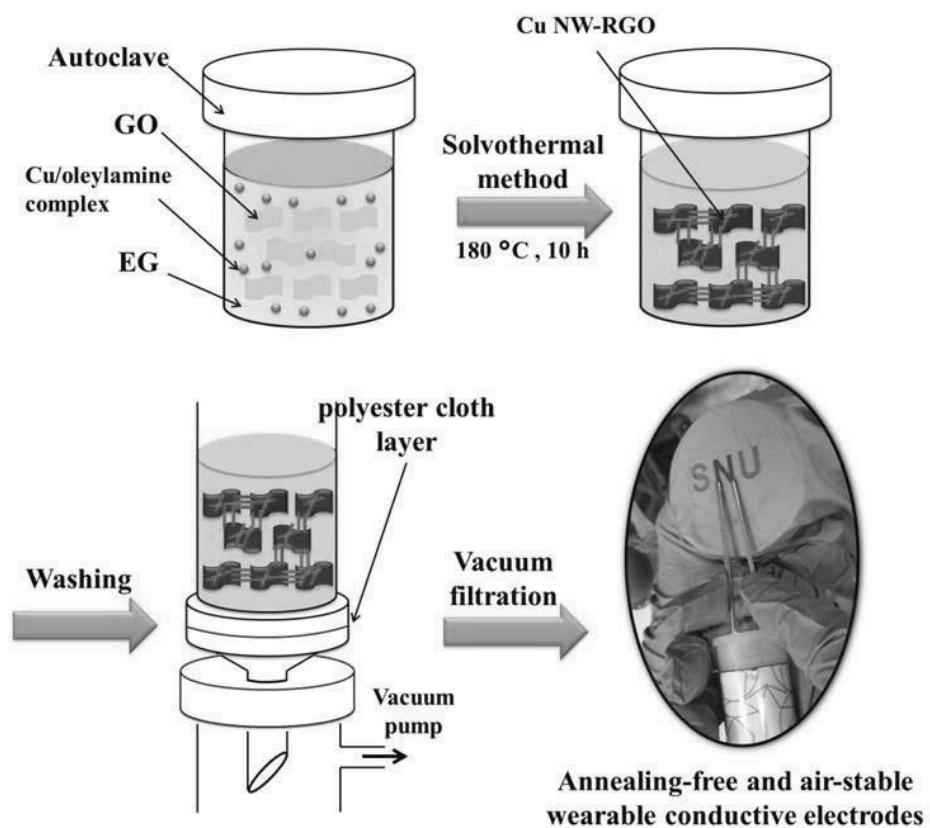
### **5.2.4 Fabrication of electrodes**

Typically, well-dispersed Cu NW-RGO composites were straight filtered on a filter paper (pore size: 3 μm) to prepare highly conductive, flexible, and durable Cu NW-RGO electrodes. Electrodes were also obtained with a polyester fabric substrate without any other treatment. The composites with various contents were directly deposited on polyester cloths by vacuum filtration. For the conductive patterning, Cu NW-RGO composites were filtered on a polyester cloth which was covered on a polymer patterning template to prepare conductive patterning electrodes on a cloth.

## **5.3 Results and discussion**

### **5.3.1 Solvothermal synthesis of CuNW-RGO composites**

As shown in Scheme 5.1, the Cu NW-RGO composites were synthesized by the GO-assisted polyol solvothermal procedure by controlling the structure-induced factors, such as the concentration of GO, capping ratio, and nucleation rate. On the basis of the previous synthetic process of Cu NWs,<sup>[26, 27]</sup> the reactions between capping agents and the nucleation rate were the two key factors to control the shape of nanowires. Here, good control depended on the interaction of GO with surfactants such as oleylamine and ammonium chloride (NH<sub>4</sub>Cl), which could form RGO-oriented Cu NWs.



**Scheme 5.1** Fabrication of Cu NW-RGO composite wearable electrode.

Figure 5.1a shows scanning electron microscopy (SEM) images of Cu NW-RGO composites. Uniform Cu NWs (average diameter:  $\sim 70$  nm, average lengths:  $\sim 30$   $\mu\text{m}$ ) were Cu NWs bridged adjacent RGO islands, which appeared relatively oriented and extended up to more than  $15$   $\mu\text{m}$ , as shown in Figure 5.1b. The TEM image (Figure 5.1c) also shows a representative Cu NW-RGO. Figure 5.1d presents the X-ray diffraction (XRD) pattern of the Cu NW-RGO composites. The peaks at  $2\theta = 43.4$ ,  $50.4$ , and  $74.2^\circ$  corresponded to the (111), (200), and (220) planes of face-centered cubic (fcc) Cu (JCPDS # 03-1018), indicating the pure phase of Cu NWs. Moreover, a broad diffraction peak appeared around  $24^\circ$  corresponding to the C (002) reflection of RGO.<sup>[33]</sup>

HR-TEM was performed to study the nanostructure and crystal structure of the Cu NWs in the composite. Figures 5.2a and c show HR-TEM images of the Cu NWs on the RGO. The fringe lattice spacing of  $0.21$  and  $0.18$  nm corresponding to the (111) and (200) planes, respectively, was clearly found, and the thin oxide layer appeared in Figure 5.2a, which suggested that RGOs did not stop the oxidation of Cu NWs fully. In addition, the corresponding fast Fourier transform patterns (FFT) in Figures 5.2b and d show two different diffraction patterns of Cu NWs, which means the 5-fold twinned structure.<sup>[34, 35]</sup> The reflection pattern in Figure 5.2b is one of the

typical cases for 5-fold twinned Cu NWs, while the electron beam is parallel to one of the exposed surfaces. The spots of  $(\bar{2}20)$  and  $(2\bar{2}0)$  are located at the growth orientation of the  $[1\bar{1}0]$  direction, which is perpendicular to  $[001]$  direction, because the beam was parallel to the  $[110]$  zone axis and penetrated the opposite side of two symmetrical surfaces with reverse angle. When the electron beam was perpendicular to one of the exposed planes, the other complicated diffraction pattern was generated by a mixture of  $[001]$  and  $[112]$  zone axis of Cu NWs in Figure 5.2d, which was overlapped in the  $(2\bar{2}0)$  diffraction spot. The observation of FFT analysis clearly demonstrated that the Cu NW is a 5-fold twinned structure, due to growth from decahedral seeds by the  $[1\bar{1}0]$  direction. The results are consistent with previous results in the literature.<sup>[35, 36]</sup> It is suggested that the Cu NWs prepared by the GO-assisted method could have good resistance to oxidation, which hindered the spontaneous formation of copper oxides on the surfaces of the Cu NWs.

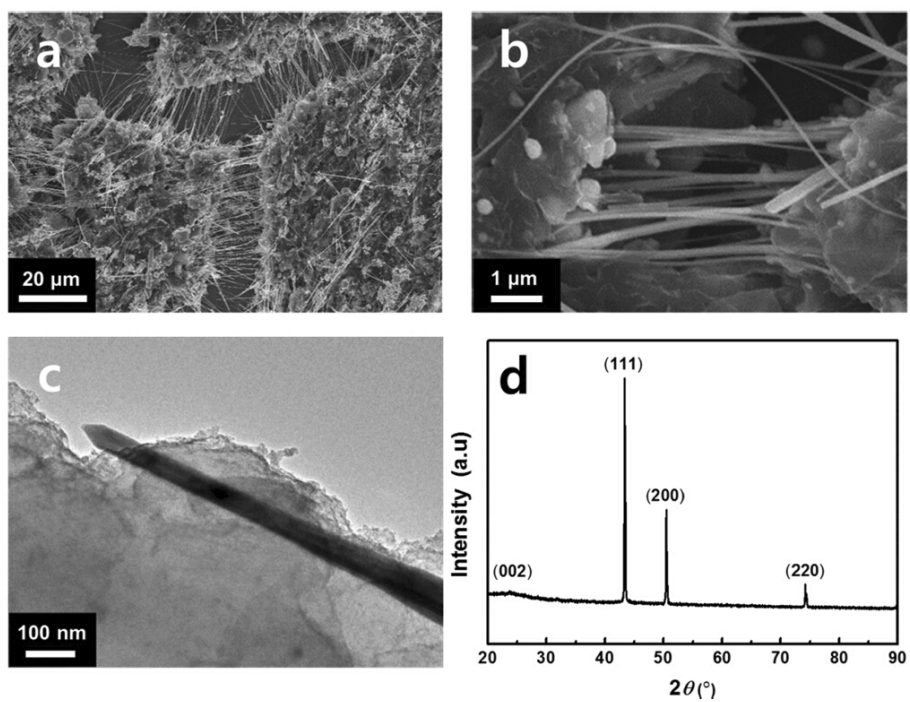


**Figure 5.1** (a, b) SEM images of Cu NW-RGO composites. (c) TEM image of Cu NW-RGO composites. (d) XRD pattern of Cu NW-RGO composites.

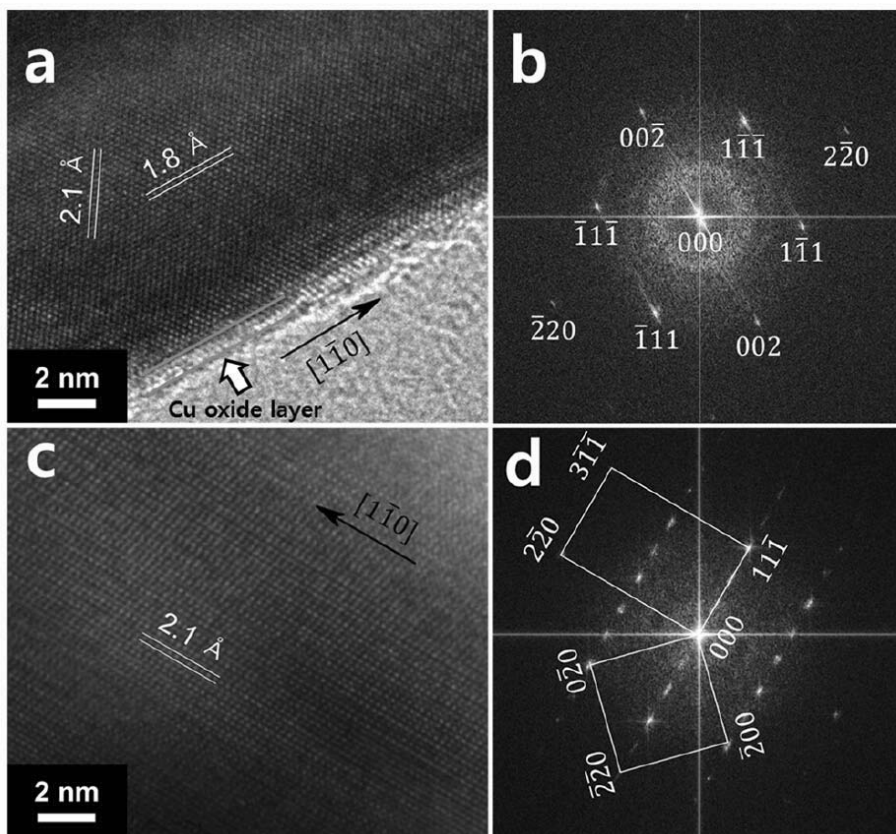


**Figure 5.2** (a, c) HR-TEM images and (b, d) corresponding FFT patterns of the Cu NW on composites with different incident electron beam.

When the pure Cu NWs prepared by the solvothermal method without GO, they were found to be extremely straight and inflexible and tended to form bundles aligned in parallel, although they were uniform in diameter. In order to uncover the GO-assisted growth mechanism of Cu NW-RGO composites, the structural transmutations of composites prepared with different concentrations of GO were investigated, as shown in Figure 5.3. When GO ( $0.25 \text{ g}\cdot\text{L}^{-1}$ ) was added, highly flexible Cu NWs grew and covered the surface of the RGO (Figure 5.3a) and showed the good bending property without breaking. This significant change indicated that Cu NW-RGO composites would have better elastic properties for the application of flexible electrodes than Cu NWs. Figure 5.3b shows Cu NW-RGO composites synthesized with  $0.75 \text{ g}\cdot\text{L}^{-1}$  GO, which possessed a unique RGO boundary containing 1D ordered Cu NWs without bundles. These unprecedented 2D tangled embedded nets could tailor the properties of Cu NW-RGO composites with unique combinations of flexibility and conductivity. As the concentration of GO increased to  $1.25 \text{ g}\cdot\text{L}^{-1}$ , the RGO boundaries gradually vanished, and irregular Cu NWs appeared on the surface of the RGO in Figure 5.3c. When the concentration of GO reached  $1.75 \text{ g}\cdot\text{L}^{-1}$ , as shown in Figure 5.3d, only a few Cu NWs with abnormal Cu particles aggregated on the edges of the RGO.

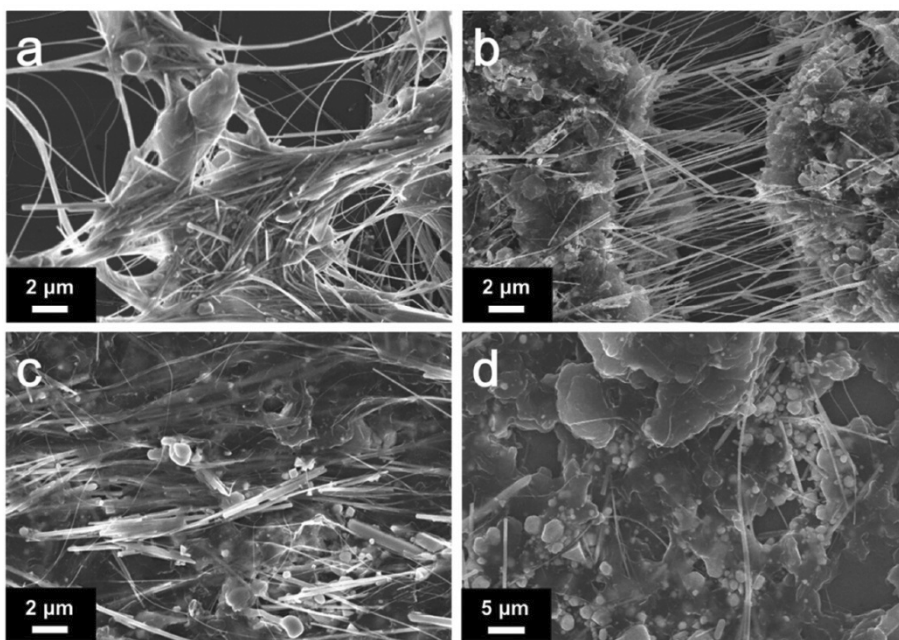


**Figure 5.3** SEM images of Cu NW-RGO composites prepared by different concentrations of GO: (a) 0.25, (b) 0.75, (c) 1.25, and (d) 1.75  $\text{g}\cdot\text{L}^{-1}$ . Other conditions: 0.06  $\text{mol}\cdot\text{L}^{-1}$  CuCl, 0.1  $\text{mol}\cdot\text{L}^{-1}$  oleylamine, 0.01  $\text{mol}\cdot\text{L}^{-1}$   $\text{NH}_4\text{Cl}$ , 180 °C, 10 h.

In the solvothermal process without GO, the Cu-amine complex was formed because of the interaction between CuCl and oleylamine, and then the complex was reduced with ethylene glycol (EG) solution as a reducing agent. In general, the surface energies of fcc Cu are  $\{110\} > \{100\} > \{111\}$ ,<sup>[37]</sup> and the shape of seeds was closely related to the crystal planes, which exposed the crystal surface with the lowest surface energy.<sup>[38]</sup> The capping effect of NH<sub>4</sub>Cl changed the surface energy and induced the exposure of the relatively stable (100) plane of Cu on the surface. As a result, the seed grew along the  $[1\bar{1}0]$  direction, forming straight Cu NWs. In the solvothermal system, GO was not only adsorbed on oleylamine because of electrostatic interaction but also aggregated Cu<sup>+</sup> by the coordination between Cu<sup>+</sup> and oxygen groups on GO. The synergistic effect induced the formation of the ternary complex of oleylamine-GO-Cu<sup>+</sup>, resulting in the growth of Cu NWs. When the concentration of GO was low, the interaction between GOs and a sufficient amount of Cu<sup>+</sup> caused the crumpled GO sheets.<sup>[39]</sup> Consequently, the steric hindrance of GO actuated the formation of arc-shaped Cu NWs instead of straight Cu NWs. Under the optimized reaction conditions, first, a sufficient amount of oxygen groups bonded to the edges of GO and could effectively stabilize the Cu seeds. Then, under the confluence of the capping and reducing agents, the regular

Cu NWs were reduced, and the nanostructures were elongated in the  $[1\bar{1}0]$  direction to connect the RGO nanosheets, which assembled 2D Cu NW-RGO embedded nets with oriented Cu NWs bridging RGOs. However, excess GOs could not only promote the reduction of  $\text{Cu}^+$ , but also prevent the capping effect of oleylamine.<sup>[33]</sup> Therefore, the growth of Cu NWs was blocked and stopped midway through the reaction, while irregularly shaped Cu NPs with a few Cu NWs were formed.

Moreover, the addition of oleylamine to the reaction was an essential factor in the formation of Cu NW-RGO composites. When oleylamine was not used in the reaction, only irregular polyhedrons with diameters ranging from 1 to 10  $\mu\text{m}$  were present (Figure 5.4a). At a low concentration of oleylamine ( $0.05 \text{ mol}\cdot\text{L}^{-1}$ ), Cu NWs gradually started to appear from the RGO edge and nearly grew across the RGO boundary (Figure 5.4b), which suggested that the amine groups of oleylamine were bound to the surface of copper nanostructures in the reaction.<sup>[27, 40]</sup> When Cu complexes enriched the edge of GO because of its plentiful oxygen groups, oleylamine could preferentially bind to the side facets of the Cu complexes, which caused preferential growth of Cu NWs along the axial  $[1\bar{1}0]$  direction from the edge of the GO. Increasing the amount of oleylamine to  $0.1 \text{ mol}\cdot\text{L}^{-1}$  led to further growth of the Cu NWs along the parallel axis, which formed 2D

embedded nets with RGOs (Figure 5.4c). Interestingly, increasing the amount of oleylamine further ( $0.15 \text{ mol}\cdot\text{L}^{-1}$ ) resulted in the formation of ultralong Cu NWs covering the RGOs in a disordered manner (Figure 5.4d). Although higher concentrations of oleylamine caused the capping effect of Cu NWs, which more easily formed longer wires with larger diameters, excessive oleylamine also led to the aggregation of RGOs accompanied by the disappearance of the RGO boundary containing 1D ordered Cu NWs.

In addition to the conditions above, the nucleation rate with different heating rates was another important condition in the preparation of Cu NW-RGO composites. Heating from 25 to 180 °C at different rates (6 and 3 °C·min<sup>-1</sup>) was performed under the optimum conditions of 0.1 L of EG, 0.006 mol of CuCl, 0.075 g of GO, 0.01 mol of oleylamine, and 0.001 mol of NH<sub>4</sub>Cl. When the heating rate was 6 °C·min<sup>-1</sup>, the precursor was quickly reduced by EG before the formation of oriented Cu NWs on RGO. As a result, few Cu NWs emerged in spite of the connected edges of RGO (Figure 5.5a). Otherwise, at the slow heating rate of 3 °C·min<sup>-1</sup> (Figure 5.5b), oriented Cu NW bridging RGOs were assembled because the precursor had sufficient time to form quasi-stable decahedral-shaped Cu, and the Cu seeds grew along the  $[1\bar{1}0]$  direction to form the nanowires.<sup>[26]</sup>

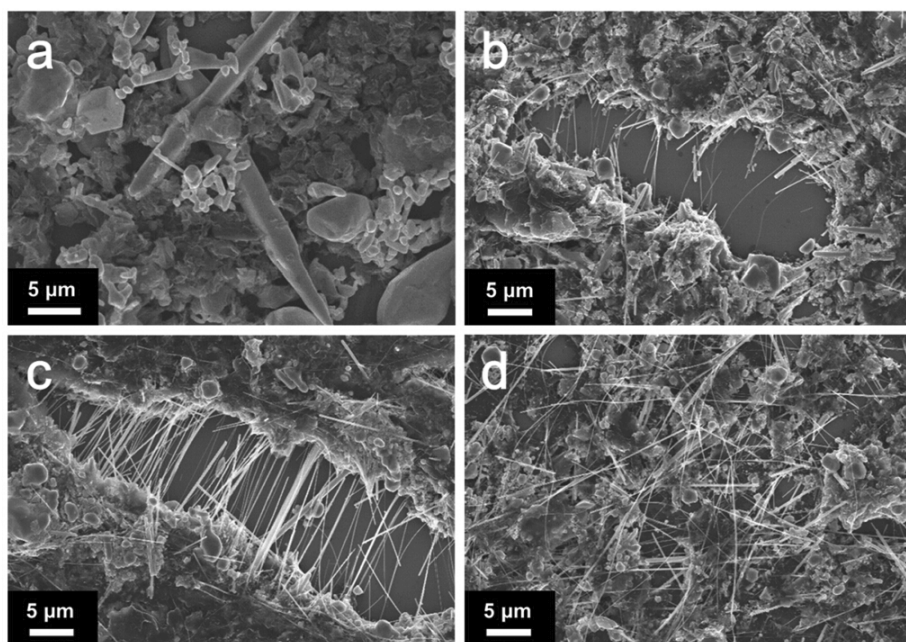


**Figure 5.4** SEM images of Cu NW-RGO composites prepared by the different concentrations of oleylamine: (a) 0, (b) 0.05, (c) 0.1, and (d) 0.15 mol·L<sup>-1</sup>. Other conditions: 0.06 mol·L<sup>-1</sup> CuCl, 0.75 g·L<sup>-1</sup> GO, 0.01 mol·L<sup>-1</sup> NH<sub>4</sub>Cl, 180 °C, 10 h.

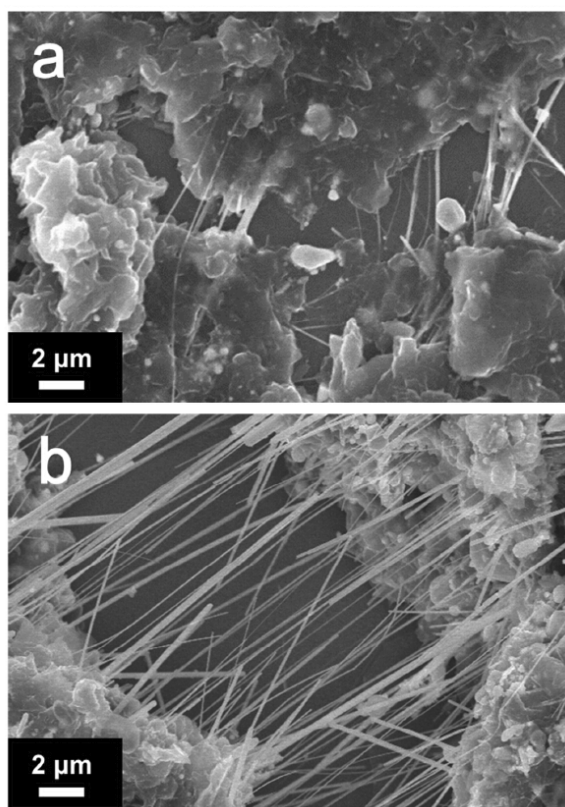


**Figure 5.5** SEM images of Cu NW-RGO composites prepared by the different heating rate: (a) 6 and (b) 3 °C·min<sup>-1</sup>. Other conditions: 0.75 g·L<sup>-1</sup> GO, 0.06 mol·L<sup>-1</sup> CuCl, 0.1 mol·L<sup>-1</sup> oleylamine, 0.01 mol·L<sup>-1</sup> NH<sub>4</sub>Cl, 180 °C, 10 h.

### 5.3.2 Unique properties of Cu NW-RGO composites

High-quality Cu NW-RGO composites offer ideal building blocks for wearable electrodes. The sheet resistances of Cu NW-RGO composite films prepared with different concentrations of GO are listed in Figure 5.6a. The sheet resistance of the Cu NW-RGO composite film decreased significantly from nearly  $10,000 \Omega \cdot \square^{-1}$  to less than  $1 \Omega \cdot \square^{-1}$  when the concentration of GO increased from 0 to  $0.75 \text{ g} \cdot \text{L}^{-1}$  GO. In general, the oxidation of Cu NWs could strongly militate against the conductivity. To achieve the ideal performance, high-temperature sintering or acid washing of Cu NW films is indispensable,<sup>[26, 41]</sup> but these methods are difficult to apply to wearable substrates such as polyester and nylon. In this system, the addition of a small amount of GO (no more than  $0.75 \text{ g} \cdot \text{L}^{-1}$ ) not only led to excellent electrical conductivity and flexibility without any added treatment but also led to durability attributed to the nanostructure. When the concentration of GO reached  $1 \text{ g} \cdot \text{L}^{-1}$ , the sheet resistance of the Cu NW-RGO composite films increased because the excessive GO restricted the growth of the Cu NWs. By optimizing the experimental conditions above, the ideal synthetic conditions for preparing Cu NW-RGO composite films were confirmed as follows: 0.006 mol of CuCl, 0.075 g of GO, 0.01 mol of oleylamine, 0.001

mol of  $\text{NH}_4\text{Cl}$ , 0.1 L of EG, and a heating rate of  $3\text{ }^\circ\text{C}\cdot\text{min}^{-1}$  from 25 to  $180\text{ }^\circ\text{C}$ .

In Figure 5.6b, the sheet resistance of the Cu NW-RGO composite film was controlled by varying the concentration of the deposition, which led to the formation of continuous nanowire networks. The sheet resistance decreased significantly ( $0.808\ \Omega\cdot\text{sq}^{-1}$  at  $5\ \text{mg}\cdot\text{cm}^{-2}$ ) with the concentration of Cu NW-RGO composites because a greater number of contact points between the Cu NWs and RGO were generated at higher concentrations. Normally, nanoscale Cu-based electrodes have plenty point-to-point contacts that serve as current pathways through partial sintering at a temperature greater than  $180\text{ }^\circ\text{C}$ .<sup>[26, 42]</sup> However, the Cu NW-RGO composites had outstanding structural advantages without sintering. A film of overlapped and stacked RGO platelets as large as several micrometers can provide a growth platform for Cu NWs and bridge initially unconnected Cu NWs, which provide two-dimensional conductive platforms for charge delivery and decrease the contact resistance compared to that of Cu NW films. Furthermore, every RGO platelet separated laterally by 1D ordered Cu NWs showed unique boundaries. This might have resulted in the higher electrical conductivity of the hybrid films due to the absence of the interplatelet junction resistances of RGO. The results suggested that the

cooperative interaction between Cu NWs and RGO led to the annealing-free fabrication of hybrid films with better electrical conductivity than pure Cu NW films.

For the further discussion of the RGO effect in the composite, we compared the sheet resistances of Cu NW-RGO, Cu NW/RGO (physical mixed), Cu NW without annealing, and Cu NW with annealing at 200 °C with different surface density (1–5 mg·cm<sup>-2</sup>), which was listed in Table 5.1. For the Cu NW-RGO by the solvothermal method and Cu NW/RGO (physical mixed), the RGO concentration was the same (0.75 g·L<sup>-1</sup>). The densities of Cu NWs in Cu NW-RGO and Cu NW/RGO (physical mixed) were a little less than those of the pure Cu NW films (annealing or without annealing) due to small amounts of RGO in the composites. In Table 5.1, the sheet resistance of every sample decreased with the increasing surface density because a greater number of contact points in the composites were generated at higher concentrations. In addition, the sheet resistance of Cu NW-RGO prepared by the solvothermal method without annealing was close to that of pure Cu NW annealing at 200 °C.

Sample	Sheet resistances ( $\Omega \cdot \text{sq}^{-1}$ ) in different surface density				
	1 $\text{mg} \cdot \text{cm}^{-2}$	2 $\text{mg} \cdot \text{cm}^{-2}$	3 $\text{mg} \cdot \text{cm}^{-2}$	4 $\text{mg} \cdot \text{cm}^{-2}$	5 $\text{mg} \cdot \text{cm}^{-2}$
Cu NW/RGO physical mixture <sup>a</sup>	$3.09 \times 10^5$	$2.24 \times 10^5$	$1.54 \times 10^5$	$7.68 \times 10^4$	$3.38 \times 10^4$
Cu NW without annealing	$2.18 \times 10^4$	$9.47 \times 10^3$	$6.47 \times 10^3$	$4.25 \times 10^3$	$1.83 \times 10^3$
Cu NW with annealing <sup>b</sup>	5.12	1.28	$9.29 \times 10^{-1}$	$5.30 \times 10^{-1}$	$1.14 \times 10^{-1}$
Cu NW-RGO without annealing <sup>c</sup>	$4.90 \times 10^2$	6.01	4.33	2.61	$8.08 \times 10^{-1}$

<sup>a</sup> The mixture is without annealing, and the RGO concentration was same to that of Cu NW-RGO prepared with  $0.75 \text{ g} \cdot \text{L}^{-1}$  GO.

<sup>b</sup> Annealing temperature was  $200 \text{ }^\circ\text{C}$

<sup>c</sup> The Cu NW-RGO was prepared with  $0.75 \text{ g} \cdot \text{L}^{-1}$  GO.

**Table 5.1** Sheet resistances in the different surface density.

Usually, Cu NW electrodes with annealing at a temperature greater than 180 °C have many contacts as electron pathways.<sup>[26]</sup> However, the Cu NW-RGO composites obtain good conductivity without sintering due to the outstanding structural advantages, as shown in Scheme 5.2a. Actually, the exposed parts of Cu NWs were oxidized, but the contact parts of Cu NWs that connected on the graphene sheets could not be oxidized. RGOs as antioxidation layers protected the contact parts of Cu NWs, which were connected on the graphene surfaces, from harsh environment. The electrons could be transported between Cu NWs and graphene by the protection of graphene leading to less junction resistance of the composite.

The resistance of Cu NW-RGO films was mainly determined by the contact resistance of junctions between Cu NWs and RGOs. For pure Cu NWs without any treatment, the oxide layer could quickly generate and tightly cover the surface of Cu NWs in air conditioning, which was attributed to high resistance due to the barrier of contacts between nanowires.<sup>[26, 43, 44]</sup> However, in the preparation of Cu NW-RGO, RGOs offered large platforms that helped the Cu NWs to grow on the surface of RGOs, resulting in the formation of close contacts between them. The firm contacting parts provided antioxidation layers for the Cu NW bridging RGOs, similar to the acid treatment and annealing method of Cu NWs,<sup>[26, 41]</sup>

which was expected to facilitate the electron transfer between Cu NWs and RGOs. Furthermore, the filtration transfer process applied the external pressure to make direct and tight contacts in the composites. For those reasons, the Cu NW-RGO composite films achieved a low contact resistance by RGO.

Compared to Cu NW/RGO (physical mixed) and Cu NW without annealing, the Cu NW-RGO also showed excellent conductivity. Without annealing, the surface on the Cu NWs could form a Cu oxide layer, which hindered electron transference between nanowires due to the high junction resistance, as shown in Figure 5.6c.

The RGOs also improved the stability of the Cu NW-RGO in air conditioning. Figures 5.6c1, c2, and c3 show the change of the relative resistance over time of pure Cu NWs and Cu NW-RGO films under ambient conditions at room temperature, 60, and 100 °C, respectively. The room-temperature resistance ratio ( $R/R_0$ ) of Cu NW films increased to 6 after 30 days; the  $R/R_0$  of the samples at 60 °C increased to 19.4 after 5 h; and the  $R/R_0$  of the samples at 100 °C increased to 38.6 after 150 min; this is because Cu is more sensitive to oxygen and moisture than other noble metals, and the faster kinetics of oxidation at higher temperatures gave rise to a more rapid increase in  $R/R_0$ .<sup>[45]</sup> However, the  $R/R_0$  of the Cu NW-RGO

composite films showed no significant change in Figure 5.6c, which indicates the extraordinary oxidation resistance of Cu NW-RGO composites. The  $R/R_0$  of the Cu NW-RGO composites only increased to 3.8 after 150 min at 100 °C due to the irreversible nature of Cu. Without RGO, the Cu NWs were generally prepared surrounded by residual oleylamine, and the oxides/hydroxides on their surface critically obstructed the electron mobility between the Cu NWs. During the addition of GO in the reaction, these Cu NWs could grow on the overlapped and stacked RGOs, which acted as a diffusion barrier to air, water, and oleylamine to protect the surface of Cu NWs from oxidation,<sup>[46]</sup> as shown in Scheme 5.2. Furthermore, the subtle change of Cu NW-RGO composites found that the  $R/R_0$  was increased in the shorter time when the temperature was higher. This meant that RGOs could not cover the Cu NWs fully as shown in Figure 5.1, leading to the surface oxidation not being suppressed completely. If the temperature was high in air conditioning, the Cu NWs in the Cu NW-RGO composite would be oxidized, which was similar to the pure Cu NWs.

In Table 5.2, the film thickness, sheet resistance, and electrical conductivity and resistivity of the Cu NW/RGO physical mixture and Cu NW-RGO composite films with different GO concentration were listed. It was found that the electrical conductivity reached the maximum without

additional posttreatments when the GO concentration was increased to 0.75 g·L<sup>-1</sup>, which suggested that RGOs partially prevented oxidation leading to the slight surface oxide involved in composite materials.

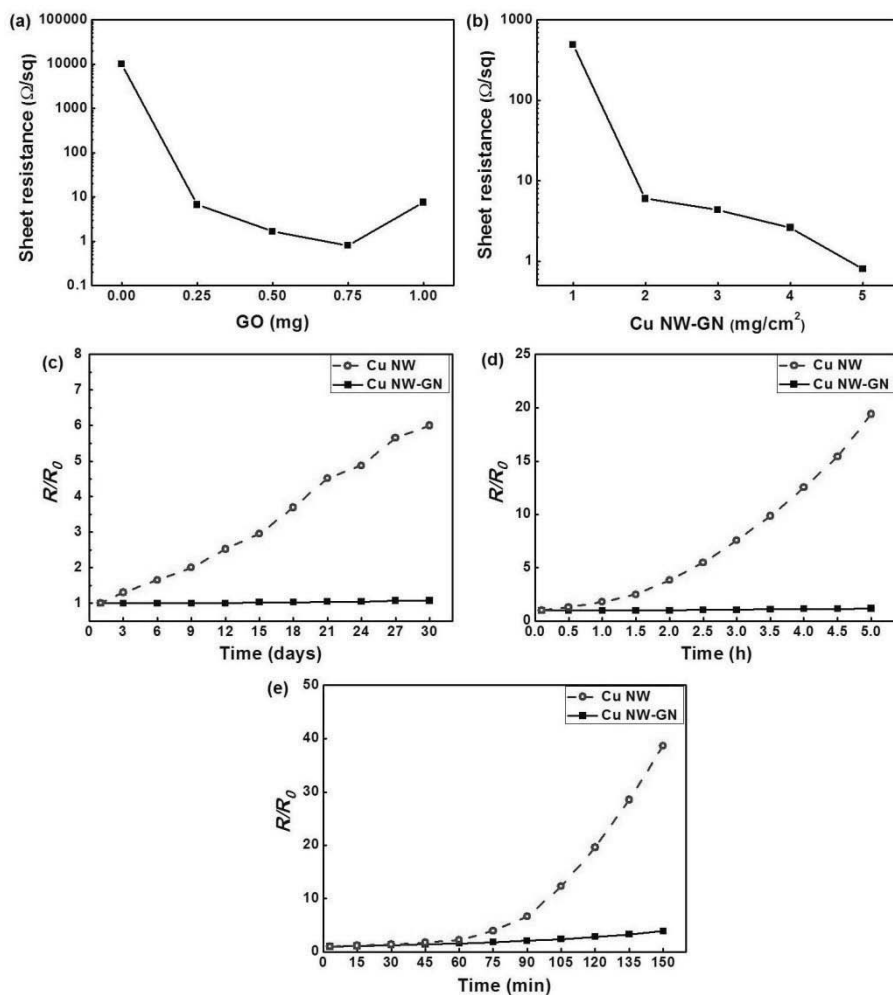
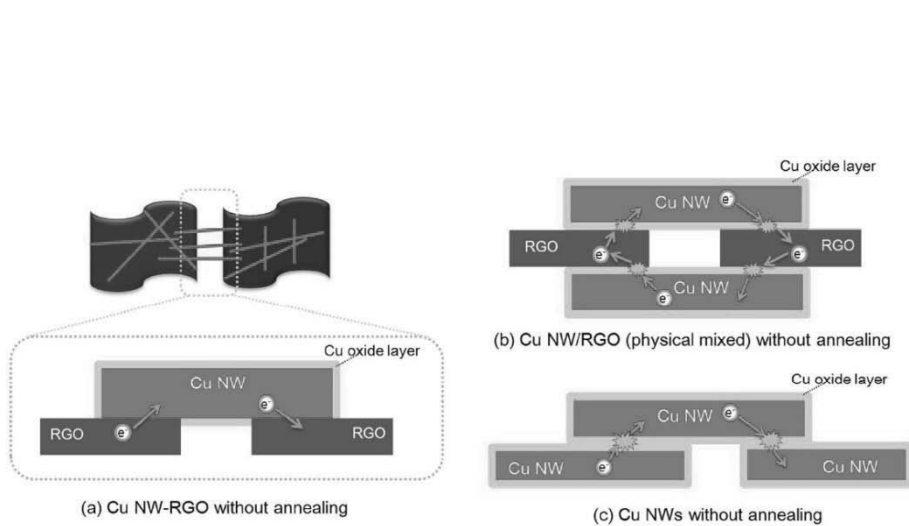


**Figure 5.6** (a) Sheet resistance of Cu NW-RGO composite films ( $5 \text{ mg} \cdot \text{cm}^{-2}$ ) with different GO concentration: 0, 0.25, 0.5, 0.75, and 1.00  $\text{g} \cdot \text{L}^{-1}$ . (b) The sheet resistance of Cu NW-RGO composite films with different surface density: 1, 2, 3, 4, and 5  $\text{mg} \cdot \text{cm}^{-2}$ . (c) Changes in the resistance ratio of pure Cu NW films and Cu NW-RGO films kept at (c1) room temperature for 30 days, (c2) 60 °C for 5 h, and (c3) 100 °C for 150 min.



**Scheme 5.2** Schematic illustration of the electron transference in (a) Cu NW-RGO composites without annealing, (b) Cu NW/RGO physical mixture without annealing and (c) Cu NWs without annealing.

Sample <sup>a</sup>	Sheet thickness (m)	Sheet resistance ( $\Omega \cdot \text{sq}^{-1}$ )	Electric conductivity ( $\text{S} \cdot \text{m}^{-1}$ )	Resistivity ( $\Omega \cdot \text{m}$ )
Cu NW without annealing	$1.456 \times 10^{-5}$	$1.83 \times 10^3$	$3.75 \times 10^1$	$2.66 \times 10^{-2}$
Cu NW-RGO with $0.25 \text{ g} \cdot \text{L}^{-1}$ GO	$1.471 \times 10^{-5}$	6.69	$1.02 \times 10^4$	$9.84 \times 10^{-5}$
Cu NW-RGO with $0.5 \text{ g} \cdot \text{L}^{-1}$ GO	$1.537 \times 10^{-5}$	1.66	$3.91 \times 10^4$	$2.55 \times 10^{-5}$
Cu NW-RGO with $0.75 \text{ g} \cdot \text{L}^{-1}$ GO	$1.512 \times 10^{-5}$	<b><math>8.08 \times 10^1</math></b>	<b><math>8.19 \times 10^4</math></b>	<b><math>1.22 \times 10^{-5}</math></b>
Cu NW-RGO with $1 \text{ g} \cdot \text{L}^{-1}$ GO	$1.576 \times 10^{-5}$	7.55	$8.40 \times 10^3$	$1.19 \times 10^{-4}$
Cu NW/RGO physical mixture <sup>b</sup>	$1.458 \times 10^{-5}$	$3.38 \times 10^4$	2.03	$4.93 \times 10^{-1}$

<sup>a</sup> All samples were without annealing.

<sup>b</sup> The RGO concentration was same to that of Cu NW-RGO prepared with  $0.75 \text{ g} \cdot \text{L}^{-1}$  GO.

**Table 5.2** The film thicknesses, sheet resistances, and electrical conductivities and resistivities of Cu NW/RGO physical mixture and Cu NW-RGO composite films with different GO concentration: 0, 0.25, 0.5, 0.75, and  $1.00 \text{ g} \cdot \text{L}^{-1}$ . (Surface density:  $5 \text{ mg} \cdot \text{cm}^{-2}$ ).

### 5.3.3 Flexible and wearable electrodes

Compared with conventional metal wires, wearable conducting materials must have excellent mechanical and electrical properties and are lightweight. Currently, wearable conducting devices are fabricated from an extensive variety of nanomaterials, including carbon nanotubes (CNTs), Ag NWs, aligned-CNT/Ag, and Ni-coated cotton composites.<sup>[2, 28, 47, 48]</sup> However, most of these strategies require many complicated and high-cost production processes (such as coating, assembling, and weaving), and the productions are easily damaged under bending, folding, or other deformations that often occur during daily use, resulting in equipment malfunctions.<sup>[49]</sup> Although the Cu NW cost per gram was nearly 1,000 times the cost of bulk Cu and the cost of our production was a little higher than the reference,<sup>[50]</sup> we chose the cheap CuCl as the Cu source and used the GO by a chemical method in order to control our cost. Furthermore, we only used the filtration process to deposit Cu NW-RGO composites on polyester fabric, which simplified the production process and decreased the expense of wearable electrodes.

In our study, the facile and simple filtration method was exploited to deposit Cu NW-RGO composites on polyester fabric as high-conductivity

electrodes to overcome the abovementioned drawbacks of conventional conducting wearable materials, as shown in Figures 5.7a and b. The Cu NW-RGO composites were also filtered on polyester fabric for a special pattern. The Cu NW-RGO composites deposited on the cloth were strongly dependent on random connections and stacking. In addition, the combination of Cu NWs and RGO maintained a high intrinsic electrical conductivity and fabric-like flexibility. In comparison with metallic wearable materials, Cu NW-RGO-based electrodes prepared with the direct coating method could easily be mended, had no metallic contacts, and were ultraportable as a thin paper. Therefore, the flexible and antioxidant composite has great potential for application to next-generation smart wearable electronics.

The conductivity of the Cu NW-RGO composites remained suitable when the fabric was bended (Figure 5.8), which clearly showed that the electrode was suitable for human motion applications. A laboratory designed bending machine was used to study the flexibility of the Cu NW-RGO composites. The composite was stressed by different bending cycles and a bending radius, which was bent by 5 mm of bending radius under 20  $\text{mm}\cdot\text{s}^{-1}$  of motion speed from 1 to 1,000 cycles. In Figure 5.7c, the resistance ratio still kept below 1.08 after 1,000 bending cycles. The good

durability of Cu NW-RGO film was likely attributed to their stable nanostructure. The Cu NW bridged between RGO nano-sheets to form a continuous conducting network that had the collaborative effect of the intrinsic conductivity and the good durability between RGOs and Cu NWs. The resistance ratio of different bending radius (5, 10, 15, and 20 mm) of Cu NW-RGO composite films is shown in Figure 5.7d, which has a little variation of the resistance ratio ( $R/R_0 < 1.82$ ) at tensile or compressive bending of 5 mm radius. Compared to our previous study,<sup>[26]</sup> it was found that the flexibility and durability (normalized resistance vs. bending radius) of Cu NW-RGO was not better than those of the linear Cu NWs, and the excess graphene hindered the growth of Cu NWs. However, Cu NWs just showed good conductivity after high-temperature annealing ( $> 180$  °C, it cannot be directly coated on polyester cloths), and the extra treatment usually resulted in the brittle Cu NWs with poor mechanical property. Although the addition of graphene affected the flexibility and durability of the Cu NW-RGO, our method overcame the defect of the annealing treatment for directly coating on polyester fabric. As a result, it retained the good mechanical property and simplified the production process, which provided the composite with potential applications in wearable devices.

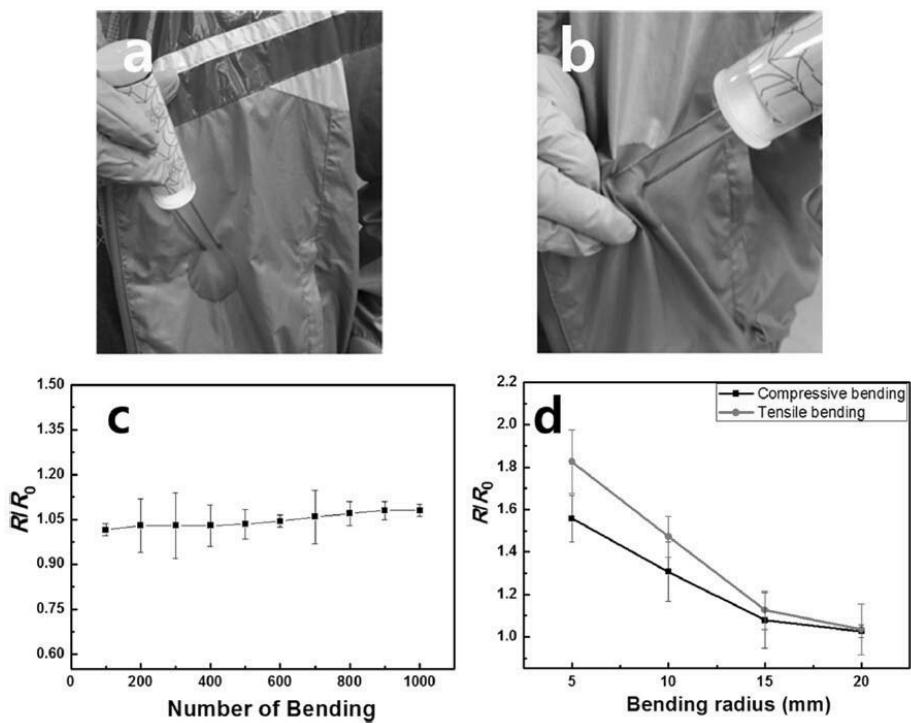


**Figure 5.7** (a) Photograph of the Cu NW-RGO composites filtered on a polyester cloth. (b) Photograph of the Cu NW-RGO composites on a polyester cloth with strong bending and lighting of an LED with an external power supply. (c) The relative resistance of Cu NW-RGO film under 1,000 times of bending cycle. (d) The relative resistance of Cu NW-RGO film under 20, 15, 10, and 5 mm of bending radius.

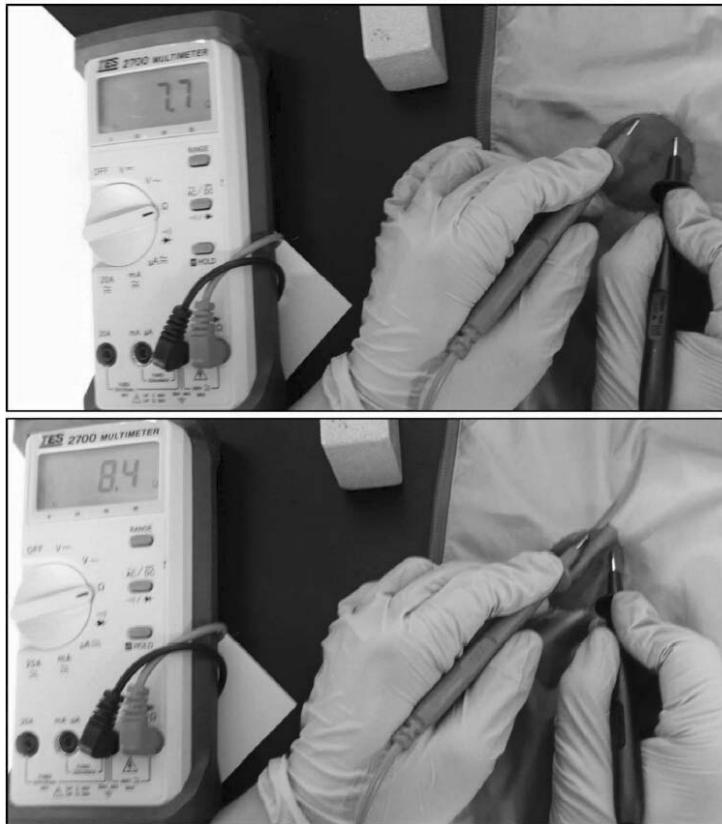


**Figure 5.8** Photographs of Cu NW-RGO composites deposited on polyester fabric for wearable conductive electrode.

## 5.4 Conclusion

In conclusion, we directly synthesized Cu NW-RGO composites for flexible, durable, and air-stable electrodes using the GO-assisted solvothermal method. Furthermore, the Cu NW-RGO composites directly deposited on the polyester cloth by a simple filtration method, and this film showed a low sheet resistance without any extra treatment, such as annealing or acid processes. The aligned Cu NWs can bridge RGO networks and act as significant pathways for charge transfer. The RGO offered an antioxidation layer protecting the Cu NWs from harsh environments. Therefore, the Cu NW-RGO composite film was superior to other flexible materials because of the combination of high conductivity, stable resistance to oxidation, and durable flexibility. We envision that this composite will be applicable to various types of ideal wearable smart clothes.

## References

- [1] S. Choi, J. Park, W. Hyun, J. Kim, J. Kim, Y. B. Lee, C. Song, H. J. Hwang, J. H. Kim, T. Hyeon, D.-H. Kim, *ACS Nano* **2015**, *9*, 6626.
- [2] S. Lee, S. Shin, S. Lee, J. Seo, J. Lee, S. Son, H. J. Cho, H. Algadi, S. Al-Sayari, D. E. Kim, T. Lee, *Adv. Funct. Mater.* **2015**, *25*, 3114.
- [3] B. Y. Ahn, E. B. Duoss, M. J. Motala, X. Guo, S.-I. Park, Y. Xiong, J. Yoon, R. G. Nuzzo, J. A. Rogers, J. A. Lewis, *Science* **2009**, *323*, 1590.
- [4] J. Wu, J. Zang, A. R. Rathmell, X. Zhao, B. J. Wiley, *Nano Lett.* **2013**, *13*, 2381.
- [5] D.-H. Shin, S. Woo, H. Yem, M. Cha, S. Cho, M. Kang, S. Jeong, Y. Kim, K. Kang, Y. Piao, *ACS Appl. Mater. Interfaces* **2014**, *6*, 3312.
- [6] H.-J. Yang, S.-Y. He, H.-L. Chen, H.-Y. Tuan, *Chem. Mater.* **2014**, *26*, 1785.
- [7] M. Z. Seyedin, J. M. Razal, P. C. Innis, G. G. Wallace, *Adv. Funct. Mater.* **2014**, *24*, 2957.
- [8] J. Ren, W. Bai, G. Guan, Y. Zhang, H. Peng, *Adv. Mater.* **2013**, *25*, 5965.
- [9] H. Sun, X. You, J. Deng, X. Chen, Z. Yang, J. Ren, H. Peng, *Adv. Mater.* **2014**, *26*, 2868.
- [10] L. Hu, M. Pasta, F. L. Mantia, L. Cui, S. Jeong, H. D. Deshazer, J. W. Choi, S. M. Han, Y. Cui, *Nano Lett.* **2010**, *10*, 708.
- [11] Z. Yang, H. Sun, T. Chen, L. Qiu, Y. Luo, H. Peng, *Angew. Chem. Int. Ed.* **2013**, *125*, 7693.
- [12] C. S. Boland, U. Khan, C. Backes, A. O'Neill, J. McCauley, S. Duane, R. Shanker, Y. Liu, I. Jurewicz, A. B. Dalton, J. N. Coleman, *ACS Nano* **2014**, *8*, 8819.
- [13] X. Zhao, B. Zheng, T. Huang, C. Gao, *Nanoscale* **2015**, *7*, 9399.
- [14] S. Yao, Y. Zhu, *Adv. Mater.* **2015**, *27*, 1480.
- [15] Y. Atwa, N. Maheshwari, I. A. Goldthorpe, *J. Mater. Chem. C* **2015**, *3*,

3908.

- [16] S. Hong, H. Lee, J. Lee, J. Kwon, S. Han, Y. D. Suh, H. Cho, J. Shin, J. Yeo, S. H. Ko, *Adv. Mater.* **2015**, *27*, 4744.
- [17] M. Park, J. Im, M. Shin, Y. Min, J. Park, H. Cho, S. Park, M.-B. Shim, S. Jeon, D.-Y. Chung, J. Bae, J. Park, U. Jeong, K. Kim, *Nat. Nanotechnol.* **2012**, *7*, 803.
- [18] S. Ye, A. R. Rathmell, Z. Chen, I. E. Stewart, B. J. Wiley, *Adv. Mater.* **2014**, *26*, 6670.
- [19] J. Song, H. Zeng, *Angew. Chem. Int. Ed.* **2015**, *54*, 9760.
- [20] J. Liang, L. Li, K. Tong, Z. Ren, W. Hu, X. Niu, Y. Chen, Q. Pei, *ACS Nano* **2014**, *8*, 1590.
- [21] J. Ge, H.-B. Yao, X. Wang, Y.-D. Ye, J.-L. Wang, Z.-Y. Wu, J.-W. Liu, F.-J. Fan, H.-L. Gao, C.-L. Zhang, S.-H. Yu, *Angew. Chem. Int. Ed.* **2013**, *52*, 1654.
- [22] S. Bhanushali, P. Ghosh, A. Ganesh, W. Cheng, *Small* **2015**, *11*, 1232.
- [23] J. W. Borchert, I. E. Stewart, S. Ye, A. R. Rathmell, B. J. Wiley, K. I. Winey, *Nanoscale* **2015**, *7*, 14496.
- [24] N. N. Jason, W. Shen, W. Cheng, *ACS Appl. Mater. Interfaces* **2015**, *7*, 16760.
- [25] S. Han, S. Hong, J. Ham, J. Yeo, J. Lee, B. Kang, P. Lee, J. Kwon, S. S. Lee, M.-Y. Yang, S. H. Ko, *Adv. Mater.* **2014**, *26*, 5808.
- [26] Z. Yin, C. Lee, S. Cho, J. Yoo, Y. Piao, Y. S. Kim, *Small* **2014**, *10*, 5047.
- [27] Z. Yin, S. K. Song, D.-J. You, Y. Ko, S. Cho, J. Yoo, S. Y. Park, Y. Piao, S. T. Chang, Y. S. Kim, *Small* **2015**, *11*, 4576.
- [28] L. Liu, Y. Yu, C. Yan, K. Li, Z. Zheng, *Nat. Commun.* **2015**, *6*, 7260.
- [29] H. Xu, H. Wang, C. Wu, N. Lin, A. M. Soomro, H. Guo, C. Liu, X. Yang, Y. Wu, D. Cai, J. Kang, *Nanoscale* **2015**, *7*, 10613.
- [30] I. N. Kholmanov, S. H. Domingues, H. Chou, X. Wang, C. Tan, J.-Y. Kim, H. Li, R. Piner, A. J. G. Zarbin, R. S. Ruoff, *ACS Nano* **2013**, *7*, 1811.

- [31] S. Stankovich, D. A. Dikin, R. D. Piner, K. A. Kohlhaas, A. Kleinhammes, Y. Jia, Y. Wu, S. T. Nguyen, R. S. Ruoff, *Carbon* **2007**, *45*, 1558.
- [32] W. S. Hummers, R. E. Offeman, *J. Am. Chem. Soc.* **1958**, *80*, 1339.
- [33] W. Zhang, B. Quan, C. Lee, S.-K. Park, X. Li, E. Choi, G. Diao, Y. Piao, *ACS Appl. Mater. Interfaces* **2015**, *7*, 2404.
- [34] M. Jin, G. He, H. Zhang, J. Zeng, Z. Xie, Y. Xia, *Angew. Chem. Int. Ed.* **2011**, *50*, 10560.
- [35] H.-J. Yang, S.-Y. He, H.-Y. Tuan, *Langmuir* **2014**, *30*, 602.
- [36] F. Meng, S. Jin, *Nano Lett.* **2012**, *12*, 234.
- [37] D. Zhang, R. Wang, M. Wen, D. Weng, X. Cui, J. Sun, H. Li, Y. Lu, *J. Am. Chem. Soc.* **2012**, *134*, 14283.
- [38] H. Guo, Y. Chen, H. Ping, J. Jin, D.-L. Peng, *Nanoscale* **2013**, *5*, 2394.
- [39] S.-T. Yang, Y. Chang, H. Wang, G. Liu, S. Chen, Y. Wang, Y. Liu, A. Cao, *J. Colloid Interf. Sci.* **2010**, *351*, 122.
- [40] A. R. Rathmell, S. M. Bergin, Y.-L. Hua, Z.-Y. Li, B. J. Wiley, *Adv. Mater.* **2010**, *22*, 3558.
- [41] Y. Won, A. Kim, D. Lee, W. Yang, K. Wo, S. Jeong, J. Moon, *NPG Asia Mater.* **2014**, *6*, e105.
- [42] T. Ishizaki, R. Watanabe, *J. Mater. Chem.* **2012**, *22*, 25198.
- [43] H. Wu, D. Kong, Z. Ruan, P.-C. Hsu, S. Wang, Z. Yu, T. J. Carney, L. Hu, S. Fan, Y. Cui, *Nat. Nanotechnol.* **2013**, *8*, 421.
- [44] S. Ding, J. Jiu, Y. Tian, T. Sugahara, S. Nagao, K. Suganuma, *Phys. Chem. Chem. Phys.* **2015**, *17*, 31110.
- [45] A. R. Rathmell, M. Nguyen, M. Chi, B. J. Wiley, *Nano Lett.* **2012**, *12*, 3193.
- [46] D. Kang, J. Y. Kwon, H. Cho, J.-H. Sim, H. S. Hwang, C. S. Kim, Y. J. Kim, R. S. Ruoff, H. S. Shin, *ACS Nano* **2012**, *6*, 7763.
- [47] N. Behabtu, C. C. Young, D. E. Tsentelovich, O. Kleinerman, X. Wang, A. W. K. Ma, E. A. Bengio, R. F. ter Waarbeek, J. J. de Jong, R. E.

- Hoogerwerf, S. B. Fairchild, J. B. Ferguson, B. Maruyama, J. Kono, Y. Talmon, Y. Cohen, M. J. Otto, M. Pasquali, *Science* **2013**, 339, 182.
- [48] H. Sun, X. You, Y. Jiang, G. Guan, X. Fang, J. Deng, P. Chen, Y. Luo, H. Peng, *Angew. Chem. Int. Ed.* **2014**, 53, 9526.
- [49] H. Sun, X. You, J. Deng, X. Chen, Z. Yang, P. Chen, X. Fang, H. Peng, *Angew. Chem. Int. Ed.* **2014**, 126, 6782.
- [50] Y. Wei, S. Chen, Y. Lin, Z. Yang, L. Liu, *J. Mater. Chem. C* **2015**, 3, 9594.

# **Chapter 6. Copper Nanowire/Multi-walled Carbon Nanotube Composites as All-nanowire Flexible Electrode for Fast-Charging/Discharging Lithium-ion Battery**

## **6.1 Introduction**

When internal combustion-powered vehicles were first invented, few predicted that they would become part of regular transportation. However, after only 13 years, carriages were replaced by vehicles. Thereafter, the internal combustion engine (ICE) was dominant in vehicles for almost 100 years, exemplifying how technology can completely alter the human lifestyle. Another example of this is autonomous vehicles (AVs). Many futurologists anticipate that AVs will become generalized within 10 years.<sup>[1]</sup>

<sup>2]</sup> With the rapid development of AVs, the electric-vehicle (EV) market has grown significantly, as EVs were selected as the preferred system for AVs. Compared with conventional ICE vehicles, EVs not only provide many advantages, such as zero air pollution and less noise and vibrations, but are

also operated by simple electric motors with an energy-conversion efficiency of 80~90%. In addition, EVs have great energy resilience, as they can be charged using various energy sources, including renewable energy, regenerative braking energy, and typical power-plant energy. However, EVs have limitations, such as the mileage, cost, safety, restricted lifetime, lack of power grid for charging, and long charging time.<sup>[3-5]</sup> These issues typically lead to the development of power systems with Li-ion batteries (LIBs). To overcome the mileage and cost problems, the energy density of LIBs must be increased. The best way to enhance the energy density is to develop new active materials with a high theoretical capacity for both the cathodes and the anodes.<sup>[6-10]</sup>

Unfortunately, even if high-capacity materials are successfully applied to LIBs, LIBs take a long time to charge because of their low power densities. Although fast chargers with pulse power have been developed, these cannot avoid energy-density fading during high-current charge/discharge, owing to the limitation in the energy-conversion reaction of LIBs. Recently, Tesla Inc. constructed supercharger stations that can charge the LIBs of EVs in 40 min to the 80% level.<sup>[11]</sup> The charging time of superchargers is shorter than that of public charging stations by a factor of approximately 17. However, 40 min is too long relative to gas charging times. To reduce the charging time,

the total resistances of LIBs must be decreased. The cell resistance is affected by the intrinsic resistance of the active materials and electrolytes. Furthermore, the contact resistance between the current collector and the active materials, the particle-interconnection resistance within the active materials, and the interfacial resistance between the electrode and the electrolyte are critical. Among these, the intrinsic resistance of the materials is difficult to reduce. The rest of resistance factors can be tuned by changing the cell design and electrode slurry composition, e.g., by using additional binders and conductive agents. However, fast-chargeable LIBs with a high energy density have numerous obstacles for conventional cell design because of the limitations in the contact-resistance reduction

Herein, we propose a novel all-nanowire electrode structure for fast-charging/discharging LIBs (both half-cell and full-cell) using Cu nanowires (CuNWs) and multi-walled C nanotubes (MWCNTs) without binders or conductive agents. The MWCNTs are the representative one-dimensional (1D) C-based nanostructure and provide pathways for the efficient transport of both electrons and ions because of their unique structures, which have a high aspect ratio and large surface area.<sup>[12]</sup> Although many researchers have reported MWCNTs as anode active materials for half-cell LIBs, MWCNTs have not been applied for full-cell LIBs, owing to their highly irreversible

Li-ion capacity and the lack of a stable voltage range (voltage plateau) caused by the spatial non-uniformity derived from their morphology.<sup>[13, 14]</sup> For these reasons, in recent years, MWCNTs have been extensively explored as current collectors for composite materials in LIBs.<sup>[12–15]</sup> Interestingly, MWCNTs with superior properties are still expected to be used for LIB anodes because super-lightweight flexible LIBs with a high energy density can be attained without conductive agents and current-collecting metal foils. Therefore, we propose a new approach different from cell design and use MWCNTs as active materials for the original role, rather than their conventional role of simple current collectors.

## 6.2 Experimental section

### 6.2.1 Synthesis of CuNWs

The CuNWs were synthesized via the salt-assisted polyol method. First, 2 mmol of CuCl (95%, Junsei) as the precursor, 0.3 mmol of NH<sub>4</sub>Cl (99.5%, Daejung) as the capping agent, and 6 mmol of oleylamine (70%, Sigma Aldrich) as the capping agent were added to 30 mL of ethylene glycol (99%, Daejung) with vigorous stirring in a 100-mL round-bottom flask. The temperature was increased to 110 °C to form the Cu<sup>+</sup>-amine complex, which was the intermediate product. After another 20 min of stirring to complete the formation, the temperature was increased to 198 °C at a heating rate of 9 °C·min<sup>-1</sup>. When the temperature reached approximately 180 °C, the CuNWs were synthesized and changed to a red-brown colour. To increase their length, the synthesized CuNWs were refluxed and kept at 198 °C for 20 min. After the reaction was complete, the products were quenched with cold water to room temperature. Finally, the CuNWs were washed with n-hexane (95%, Daejung) and centrifuged for 5 min at 8,000 rpm. After the washing step was repeated three times, the CuNWs were dispersed in isopropyl alcohol (IPA) (99.5%, Daejung) to form the composite anode film.

## **6.2.2 Fabrication of CNMC anodes**

The MWCNTs (95%, CM-95) were purchased from Hanwha Chemical Co., Ltd. and were 20  $\mu\text{m}$  long and 10 nm wide. They were dispersed in IPA and mixed with CuNWs/IPA dispersions with various composite ratios (CuNW:MWCNT = 1:1, 3:1, 5:1, and 7:1, w/w). All of the MWCNT and CNMC samples were fabricated with the same amount of MWCNTs. After 30 s of sonication, the composite dispersion was filtered using a cellulose acetate (CA) membrane (0.2  $\mu\text{m}$  pore, Advantec). Then, the CNMC films were easily peeled from the CA membrane and sintered at 180  $^{\circ}\text{C}$  for 30 min under glycerol reducing conditions. Finally, the highly conductive CNMC electrodes for use as battery anodes were fabricated.

## **6.2.3 Material characterizations**

The CuNW, MWCNT, and CNMC electrodes were characterized via field-emission scanning electron microscopy (Hitachi, S-4800), high-resolution transmission electron microscopy (JEM-2100F, JEOL), and X-ray diffraction analysis (Bruker, D8 DISCOVER). A conductivity meter

with a four-point probe (AIT Co., Ltd CMT-SR2000N) was used to measure the sheet resistance of the electrode films.

## 6.2.4 Electrochemical measurements

CR-2032 coin cells were assembled to investigate the electrochemical properties. The half cell comprised a CNMC electrode, a separator (polypropylene, PP; Celgard 2300) with a liquid electrolyte (1 M LiPF<sub>6</sub> in EC/DMC/DEC, 1:1:1 volume ratio, Panax E-Tec), and a 150- $\mu$ m-thick Li foil. The full-cell assembly was characterized in an Ar atmosphere with the LiFePO<sub>4</sub> (99.9%, MTI Korea) and MWCNT (95%, CM-95, Hanwha chemical Co., Ltd.) composite cathode at a weight ratio of 1:2, which was also prepared via the aforementioned filtration method. The full cell was assembled with an N/P ratio of 1:1.5. In the case of bare MWCNTs, the theoretical full-cell capacity is 66.41 mAh·g<sup>-1</sup>. The half cells were characterized from 0.02 to 2.4 V, and the full cells were analyzed in the potential range of 0.02–2.5 V.

The cell resistance was evaluated via an alternating-current (AC) impedance test involving electrochemical cells. AC impedance spectroscopy (CHI660E, CH Instruments) was performed from 0.1 HZ to 1

MHz at room temperature with an amplitude of 5 mV. The manufactured cells were characterized according to their capacity, cyclability, and rate capability under charging/discharging in a battery cycler system (WBCS 3000L, WonATech).

## **6.3 Results and discussion**

### **6.3.1 Preparation and characterization of CNMC anode**

To stabilize the irregularly shaped MWCNTs and improve the anode resistance, we employed CuNWs as a new type of current collector. As a highly conductive 1D metal nanostructure, the CuNWs exhibited tremendous potential for developing battery performances with a strong contact to the active materials, which is a same ingredient with the conventional current collector of LIB anodes. Because of the excellent electrical conductivity, high aspect ratio, and large surface area of CuNWs, the three-dimensional (3D) percolated network provides better conducting pathways and ion diffusion for fast-charging/discharging LIBs.<sup>[16, 17]</sup> For the traditional anode, various compositions of active materials, binders, and conductive agents were homogenously mixed to form a slurry, which was coated on Cu foil. In addition to active materials containing a significant cell capacity, other materials are needed during this process to obtain the proper slurry composition. However, these extra materials and this troublesome process increase the overall price of the battery. In this study, the advanced CNMC film as a freestanding anode for LIBs was fabricated

via a simple filtration method. The composite anodes were called CNMC1, CNMC3, CNMC5, and CNMC7 and had different composition mass ratios (CuNW:MWCNT = 1:1, 3:1, 5:1 and 7:1, w/w). Figures 6.1a and b show the two types of 1D structural nanomaterials; the CuNWs (80 nm in width and 30  $\mu\text{m}$  in length) and the MWCNTs (10 nm in width and 20  $\mu\text{m}$  in length) with a high aspect ratio. Although the thinner CuNWs may yield higher battery performance, considering the oxidation problem, structural stability, and electron mean free path in NWs, we employed 80-nm stable CuNWs in this study, which were modified from a reported method.<sup>[16]</sup> Generally, large surface areas and peripheral Cu atoms with a nanoscale radius induce a high surface energy. To reach a steady state, the CuNWs reduce their surface energy through surface passivation or mutual aggregation.<sup>[16-18]</sup> Therefore, the MWCNTs were strongly adsorbed on the surface of the CuNWs via hydrophobic interaction and electrostatic attraction when the CNMC electrode was prepared (Figure 6.1c).<sup>[19, 20]</sup> Furthermore, the random CuNW network with 3D structure provided a rigid framework to effectively prevent the shrinkage and expansion of active materials which caused by the aggregation and swelling. The X-ray diffraction (XRD) patterns of CNMCs with different mixing ratios are shown in Figure 6.1d. In the presence of bare MWCNTs, the broad C peak

is located near  $26^\circ$  because of the diffraction of the  $\{002\}$  plane. By increasing the CuNW content, the three representative Cu peaks are more clearly observed at  $2\theta = 43.4^\circ$ ,  $50.4^\circ$ , and  $74.2^\circ$ , which correspond to the diffractions of the  $\{111\}$ ,  $\{200\}$ , and  $\{220\}$  planes, respectively, of Cu (JCPDS # 03-1018).

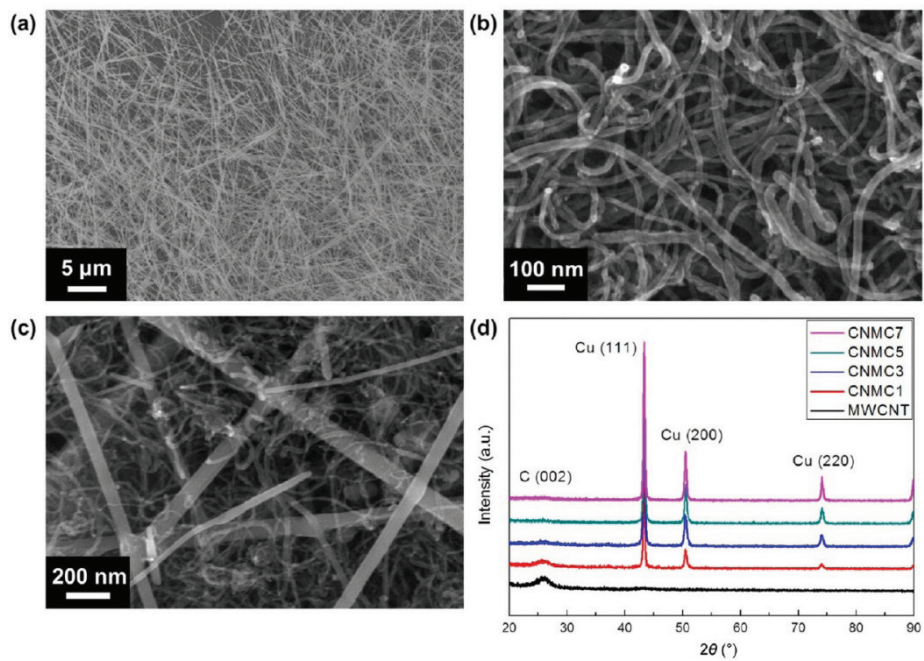


**Figure 6.1** Scanning electron micrographs of two types of proposed 1D nanomaterials and their composite: (a) CuNWs, (b) MWCNTs, and (c) CNMC7. (d) X-ray diffraction patterns of MWCNTs and CNMCs.

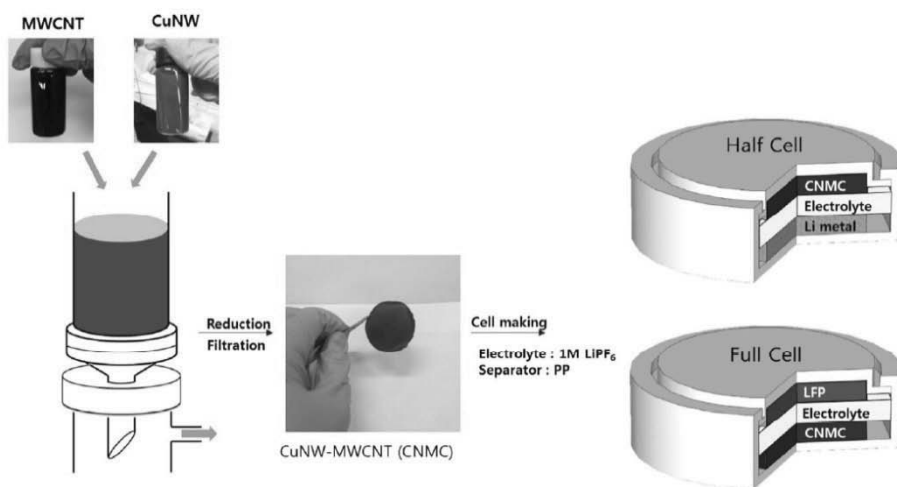
### 6.3.2 Properties and merits of CNMC anode

We prepared a 3D structural anode with two types of 1D nanomaterials and cell structures, as described in Figure 6.2a and Scheme 6.1. This cell structure does not require a current-collecting metal foil, conductive agents, or binders. Additionally, the CNMC electrode thickness was freely controlled up to 647  $\mu\text{m}$  using a simple filtration method (Figure 6.3). Therefore, the cell was made lighter and smaller by adopting the suggested electrode system. Furthermore, the 3D structural anode had a great advantage with regard to the resistance. To demonstrate this, we observed the effect of the resistance difference using various measurements when comparing the CNMCs with MWCNT anodes. All of the MWCNT and CNMC samples were fabricated with the same amount of MWCNTs, and the mass of the bare CuNW films was equal to that of CNMC7 for comparison. The loading mass of active materials (MWCNT) was fixed as 1.15 mg when applied to the 10-mm coin-cell anodes. Furthermore, because of the difference in the CuNW contents, the thickness of the MWCNT and CNMC1, CNMC3, CNMC5, and CNMC7 anodes were 61, 56, 69, 98, and 126  $\mu\text{m}$ , respectively. Generally, the oxide layers on the CuNW surface as the contact barrier prevents the electron transport and enhances the

resistance of the composite anodes.<sup>[21]</sup> In this study, the natural oxide layers were reduced, and the network was percolated in the glycerol reducing condition at 200 °C, which provides more surface energy than is needed to cause the CuNWs welding. As shown in Figure 6.2b, the sheet resistance of the CNMC films decreased dramatically when the CuNWs were added and annealed. Although both CuNWs and MWCNTs are conductive 1D nanomaterial, they have a large contact resistance when the film is formed. This contact resistance is more clearly observed for a large area.<sup>[22]</sup> However, the contact resistance of the CuNWs can be reduced via the aforementioned welding process, which is not applicable to MWCNTs. As a highly conductive framework for current pathways, the random CuNW network with 3D structure was directly connected to MWCNTs, which effectively transported the electrons during the charge/discharge process. Therefore, the CuNW content can easily affect the overall resistance of the composite films, and the resistance of the bare MWCNT network is far higher than that of the CuNW network. The cell resistances also matched the sheet resistance of the MWCNTs and CNMCs, where PP, LiPF<sub>6</sub>, and Li metal were used as the separator, electrolyte, and reference and counter electrodes, respectively. Figure 6.2c shows the charge-transport conductivities of various types of CNMCs according to the half-cell test.

The charge-transport resistance increased with the CuNW ratio, which ranged from 167.85  $\Omega\cdot\text{cm}$  for the bare MWCNTs to 103.94  $\Omega\cdot\text{cm}$  at high CuNW contents. These tendencies were also observed for the full cell with the  $\text{LiFePO}_4/\text{MWCNT}$  cathode, as shown in Figure 6.4. To achieve full-cell and flexible batteries, the  $\text{LiFePO}_4$ -MWCNT composites were used as the cathode without metal foils. Because of the high resistivity of  $\text{LiFePO}_4$ , the MWCNT as the current collector was added at a weight ratio of 1:2 to improve the conductivity of the cathode for better electrochemical performance. Additionally, the highly conductive CuNWs affected the internal resistance of the half cells shown in Figure 6.2d, which is the galvanostatic intermittent titration technique (GITT) analysis examined at 1C rate.<sup>[23, 24]</sup> As a result, the CNMC7 exhibited the most excellent conductive characteristics, along with the aforementioned tendencies. In addition, the Li-cation diffusion coefficients were inversely proportional to the voltage change under a constant current; thus, CNMC7 had a highest Li-cation diffusion rate, which was caused by the low resistance of the CuNWs. Generally, most of the LIBs are not fully charged and discharged, for their safety and durability—they are used from 20~30% to 70~80% according to the state of the charge.<sup>[25]</sup> The resistance change of CNMC7 was smaller than that of the MWCNTs, which means that CNMC7 was a more stable

anode material because of the welded CuNW network. As described in Figure 6.5, the CuNW network is percolated at the contact point, resulting in a rigid 3D framework that finely controls the MWCNT volume change via lithiation/delithiation during operation and effectively inhibits the Li-dendrite growth.<sup>[26,27]</sup>



**Scheme 6.1** Schematic illustration of the CNMC anode film preparation and their application in battery cells (half cell and full cell).

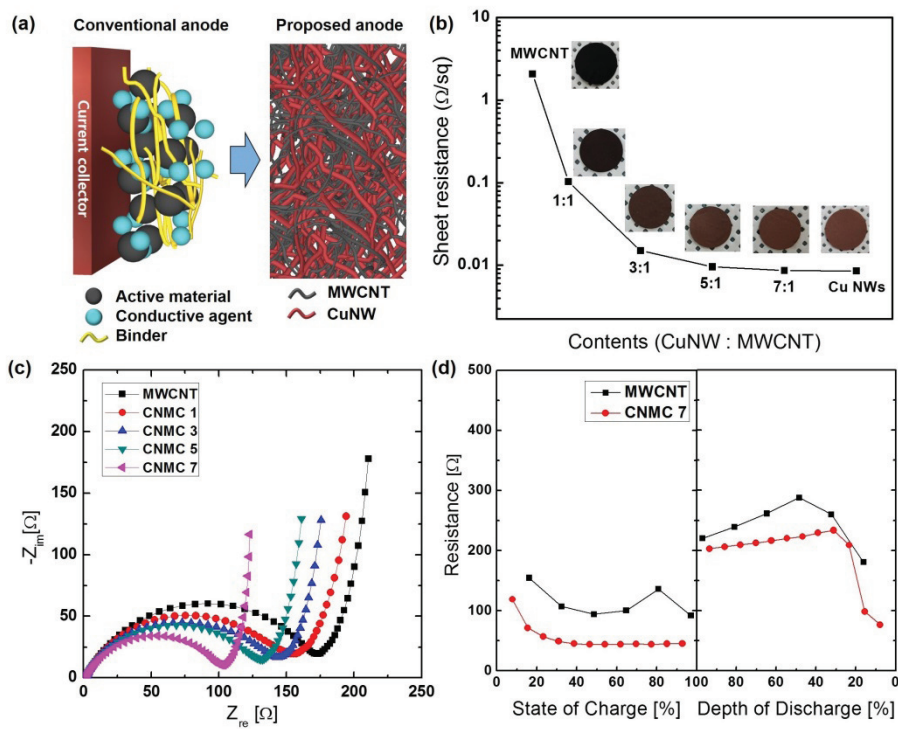


**Figure 6.2** (a) Schematic illustration of the conventional anode and proposed CNMC anode. (b) Sheet resistance of CNMC, MWCNT, and CuNW films. (c) Electrochemical impedance spectra of the half cells using CNMC7 and MWCNT as the anode in the frequency range of 1 MHz to 0.1 Hz. (d) Internal resistance of half cells with respect to the state of charge and the depth of discharge. The inset graphs show the GITT analysis, with CNMC7 and MWCNT as the anode.

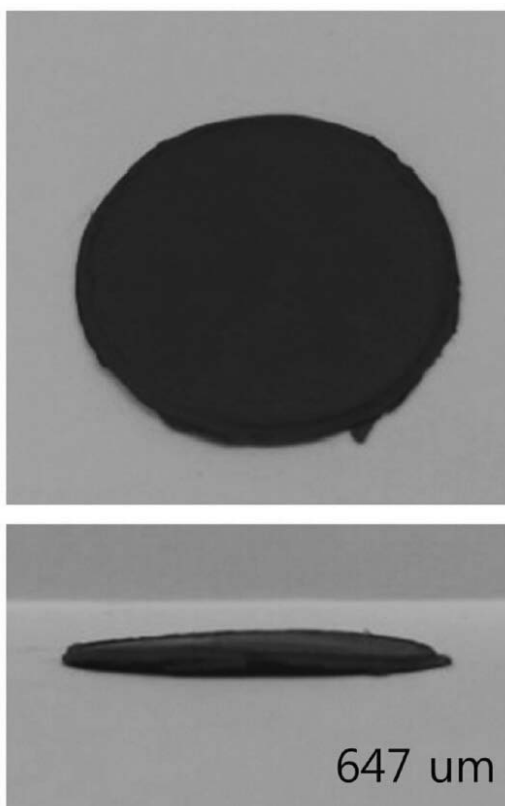


**Figure 6.3** The photographs of 647  $\mu\text{m}$  of thick CNMC7 electrode, fabricated by a simple filtration method.

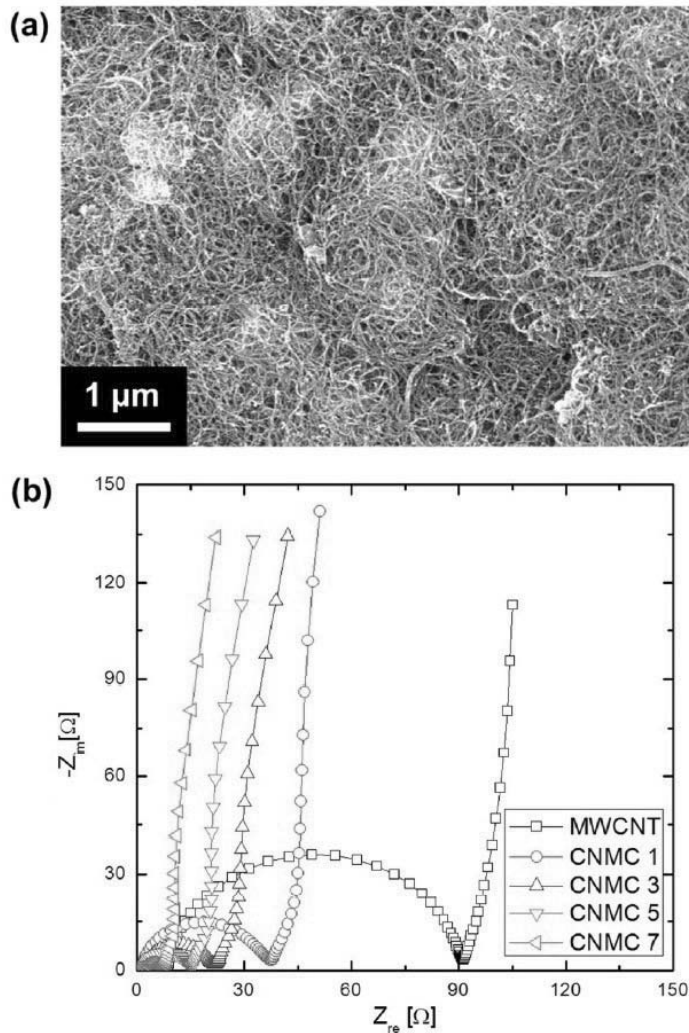


**Figure 6.4** (a) The SEM image of the full-cell cathode of  $\text{LiFePO}_4/\text{MWCNT}$  composites (1:2 of weight ratio). (b) Impedance analysis of the full cells using CNMCs and MWCNT as the anodes in frequency from 1 MHz to 0.1 Hz, where employed PP separator,  $\text{LiPF}_6$  of electrolyte and  $\text{LiFePO}_4/\text{MWCNT}$  of cathode, as described in Scheme 6.1.

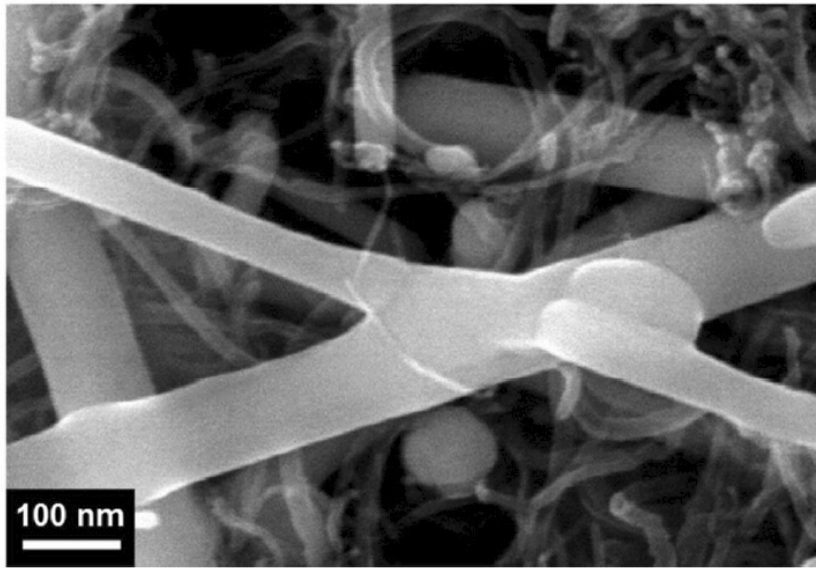


**Figure 6.5** SEM image of CuNWs welding in CNMC7 anode.

These phenomena were confirmed by the tap density and normalized Li-ion diffusion coefficient, as described in Figure 6.6. The tap density of the composite films increased with the CuNW content, as shown in Figure 6.6a, because the relative atomic mass of Cu is far greater than that of C and the solid nanowire structure is far denser than the hollow nanotube structure.<sup>[28,</sup>  
<sup>29]</sup> The most significant problem regarding the use of pure MWCNTs in battery anodes is the expansion of the anode film when the electrolytes are encountered. Generally, the MWCNT film shrinks during the drying process owing to the formation of a stable structure after agglomeration. Therefore, the porous MWCNT film significantly swells after absorbing the solvent. This decreases the tap density of the MWCNT film and enhances the contact resistance between the MWCNT junctions, because of their weak Van der Waals forces.<sup>[30]</sup> The resulting unstable structure is liable to cause short-circuit problems in the assembly process and the charge/discharge process of cells. During the volume expansion induced by Li-cation intercalation, the weak Van der Waals forces cannot withstand the expansion pressure, causing the MWCNTs to break away from the film. However, the stable structure of the CNMC film is effective for preventing the shrinkage and expansion of MWCNTs because of the rigid framework of the welded CuNW network. Consequently, the CNMC film exhibited no

change, and the bare MWCNT film was expanded by approximately 16% when wetted by the electrolyte (Figure 6.6b). As is well known, highly packed electrodes normally interfere in ion transport; thus, a high tap density means low Li-ion diffusion. However, CNMC7 has high Li-ion diffusion even though it is denser than MWCNTs, because of the outstanding conductivity provided by the welded CuNW network (Figures 6.6c and d). Therefore, the additional binder and conductive agents are unnecessary in this system, which can be easily applied to lightweight LIBs with a high energy density and power density.

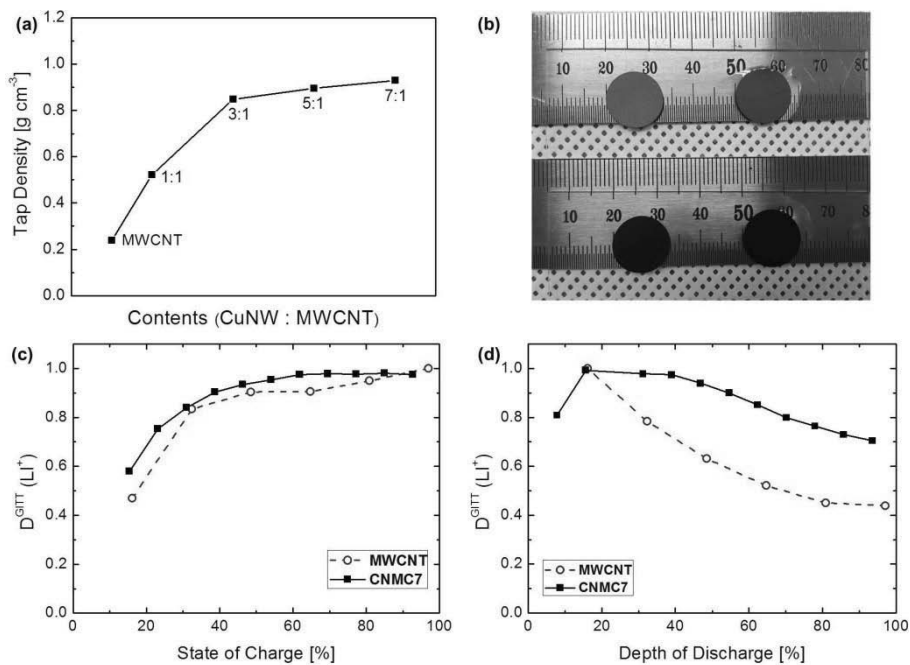


**Figure 6.6** (a) Tap density of anodes with different composite ratios (w/w). (b) Photograph of the swelling test of the CNMC7 and MWCNT electrodes. After wetting with the electrolyte (1 M  $\text{LiPF}_6$  in EC/DMC/DEC = 1:1:1, v/v/v), the CNMC7 film exhibited no change, but the area of the MWCNT film was expanded by approximately 16%. (c, d)  $\text{Li}^+$  diffusion coefficient of half cells using CNMC7 and MWCNT anodes with respect to the state of charge and the depth of discharge, calculated from the GITT measurement.

### 6.3.3 Electrochemical analysis of CNMC anode

The superior characteristics of CNMCs were demonstrated via chronopotentiometry. Each tested sample was examined after aging at 0.2C for 1 cycle. Figures 6.7a and b show the capacity rate performance determined via the galvanostatic charge/discharge method. We assumed that the theoretical capacity of MWCNTs is  $400 \text{ mAh}\cdot\text{g}^{-1}$ .<sup>[31, 32]</sup> As shown in Figure 6.7a, rates of 0.2C, 0.5C, 1C, 5C, 10C, and 0.2C were applied to observe the capacity retention. The capacity decreased in the initial three cycles because of the aging effect but thereafter maintained a stable performance at each rate. Furthermore, the capacity increased with the addition of CuNWs, and CNMC7 exhibited the highest value. Compared with reported results, the CNMC7 anodes in this study exhibited excellent electrochemical performance, with high-current operation (Table 6.1). Although the addition of CuNW increased the overall weight of the electrode, the reduction of the internal resistance was significant, as shown in Figure 6.2, allowing rapid charging and discharging. The main reason for the selection of CNMC7 is its high volumetric capacity, which is key factor for practical applications (Figure 6.8). These tendencies agree with the aforementioned results for the anode resistance, which is the main reason

for the high capacity. As shown in Figure 6.7c, the voltage difference of the anode between the charging curve and the discharging curve appears to decrease with an increasing CuNW content. This voltage gap is strongly related to the conductivity of the working electrode, and the narrow voltage gap indicates a large capacity.<sup>[25]</sup> Additionally, the irreversible capacities were decreased by increments of the CuNW contents, as shown in Figure 6.9. As a result, there was a difference of 8.31% in the irreversible capacity between the MWCNTs and CNMC7, although the initial capacity of CNMC7 was higher than that of the MWCNTs.

The final capacities at 0.2C were significantly increased compared with the initial value, depending on the CuNW content (Figure 6.7a). The pure MWCNTs only recovered 76.62% of the capacity, and CNMC7 was improved to 104.89% of the capacity. Although the CuNW network was welded in the reducing condition before the cell assembly, the contact resistance still existed in the junction parts. In the charging/discharging process, these contact resistances in the electrode were efficiently decreased by the joule-heated welding with a current flow.<sup>[33]</sup> Therefore, the specific capacity was increased by the welding effect of the CuNWs, and the increment was strongly dependent on the CuNW content. The capacity increment was confirmed by the cycle stabilities, as shown in Figure 6.7b.

The rate of 0.5C was applied for the initial and final 100 cycles, whereas 5C was applied for the 300 cycles following the initial 100 cycles. The capacity was retained during the cycling and recovered to 89.75% of the initial value, even under repeated charging and discharging with harsh electrical conditions at 5C. In particular, the CNMC7 maintained a high capacity of 215 mAh·g<sup>-1</sup> at 5C, indicating that the LIBs prepared with the CNMC7 anode charged 55.78% of the capacity within 12 min, repeatedly. The excellent capacitive properties of CNMC anodes were confirmed by testing full-cell LIBs, as shown in Figure 6.7d, where rates of 0.2C, 0.5C, 1C, 5C, and 0.2C were applied. In the cathode part, we used commercial LiFePO<sub>4</sub> (EQ-Lib-LFPO, MTI Korea) which have a low conductivity to fabricate the LIBs without any treatment. By controlling the MWCNT content and N/P ratio, the difference in electrochemical performances was accurately reflected in the battery tests (Figure 6.7d). A capacity far higher than the theoretical full-cell capacity (66.41 mAh·g<sup>-1</sup>) was achieved, which is mainly attributed to the highly conductive CNMC7 anode. The MWCNTs exhibited the lowest capacity because the capacity was provided by the double-layer capacitance and not intercalation, as shown in Figure 6.10a. These behaviors are attributed to the intrinsic properties of MWCNTs, such as the large voltage gap between charging and discharging, because of the

inadequate conductivity of anode materials without an additional conductive agent (Figure 6.10b). For this reason, MWCNTs have not been used as anode materials in full-cell LIBs. However, CNMC7 exhibits a reasonable capacity with a narrow voltage gap, which arises from the enhanced anode conductivity due to the highly conductive CuNW framework. Hence, we overcame the limitation of MWCNTs as anode materials for fast-charging/discharging half-cell and full-cell LIBs by employing CuNWs.

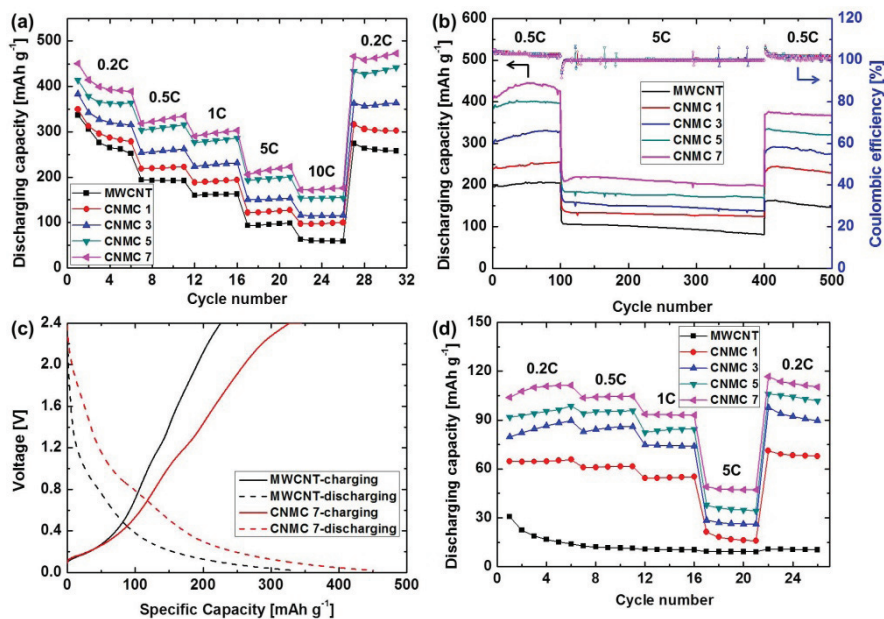


**Figure 6.7** (a) Rate capability of various CNMC and MWCNT anodes. (b) Cycling performance and Coulombic efficiency of various CNMC and MWCNT anodes (after 31<sup>st</sup> cycle of rate-capability test). (c) Charge-discharge curves of anodes made by CNMC7 and MWCNT at 0.2 C-rate in the 1<sup>st</sup> cycle. (d) Rate capability of CNMC and MWCNT anodes in the full cell with a PP separator, LiPF<sub>6</sub> electrolyte, and LiFePO<sub>4</sub>/MWCNT cathode.

Anode materials	Half cell		Full cell (LFP//CNMC)		Reference
	Current density [mA g <sup>-1</sup> ]	Specific capacity [mAh g <sup>-1</sup> ]	Current density [mA g <sup>-1</sup> ]	Specific capacity [mAh g <sup>-1</sup> ]	
CNMC7	80 (0.2C)	466	34 (0.2C)	113	This work
	200 (0.5C)	327	63 (0.5C)	104	
	400 (1C)	297	170 (1C)	93	
	2000 (5C)	215	850 (5C)	48	
	4000 (10C)	174	---	---	
3-D CNT-graphene	63 (0.17C)	250	---	---	<i>Carbon</i> <b>2014</b> , 68, 493
	632 (1.7C)	59			
Graphene wrapped CNT	100	373	---	---	<i>Electrochim. Acta</i> <b>2015</b> , 186, 142
	250	229			
	500	136			
3-D CNT	74.4 (0.2C)	312	---	---	<i>J. Power Sources</i> <b>2015</b> , 229, 465
	186 (0.5C)	251			
	372 (1C)	211			
	1116 (3C)	155			
Vertical-aligned MWNT array	100	350	---	---	<i>J. Power Sources</i> <b>2016</b> , 311, 42–48
1200 °C heated CNT film	100 (0.5C)	446	---	---	<i>J. Power Sources</i> <b>2015</b> , 279, 495
	2000 (10C)	136			
MWCNT Paper Anodes	74.4	340	---	---	<i>J. Nanosci. Nanotechnol.</i> <b>2009</b> , 9, 3406
	372	225			
3D free-standing CNTs	37.2 (0.1C)	374	---	---	<i>Nanotechnology</i> <b>2016</b> , 27, 105402
	372 (1C)	248			
	1116 (3C)	147			

**Table 6.1** The comparison of electrochemical performances with other CNT-based anodes.

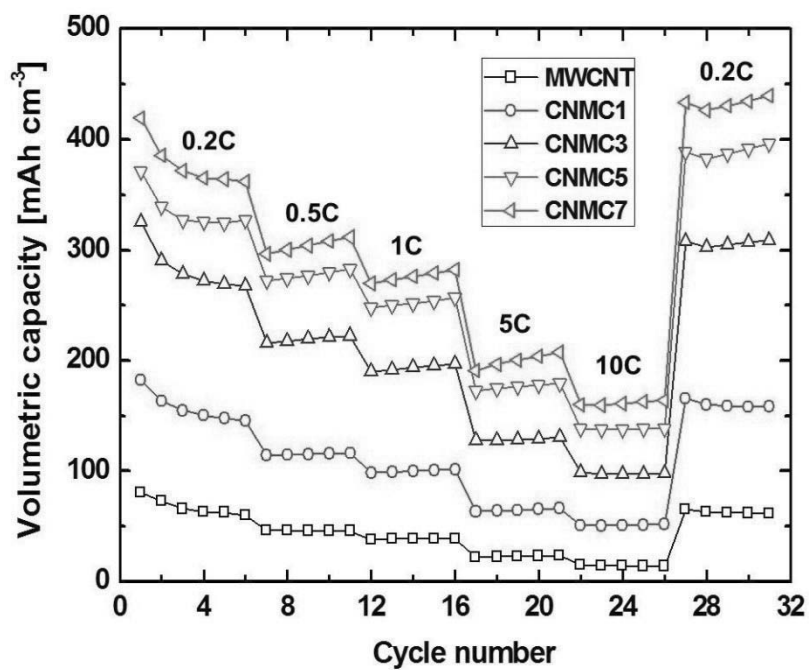


**Figure 6.8** Volumetric capacities of MWCNT and CNMC anodes with rate performance.

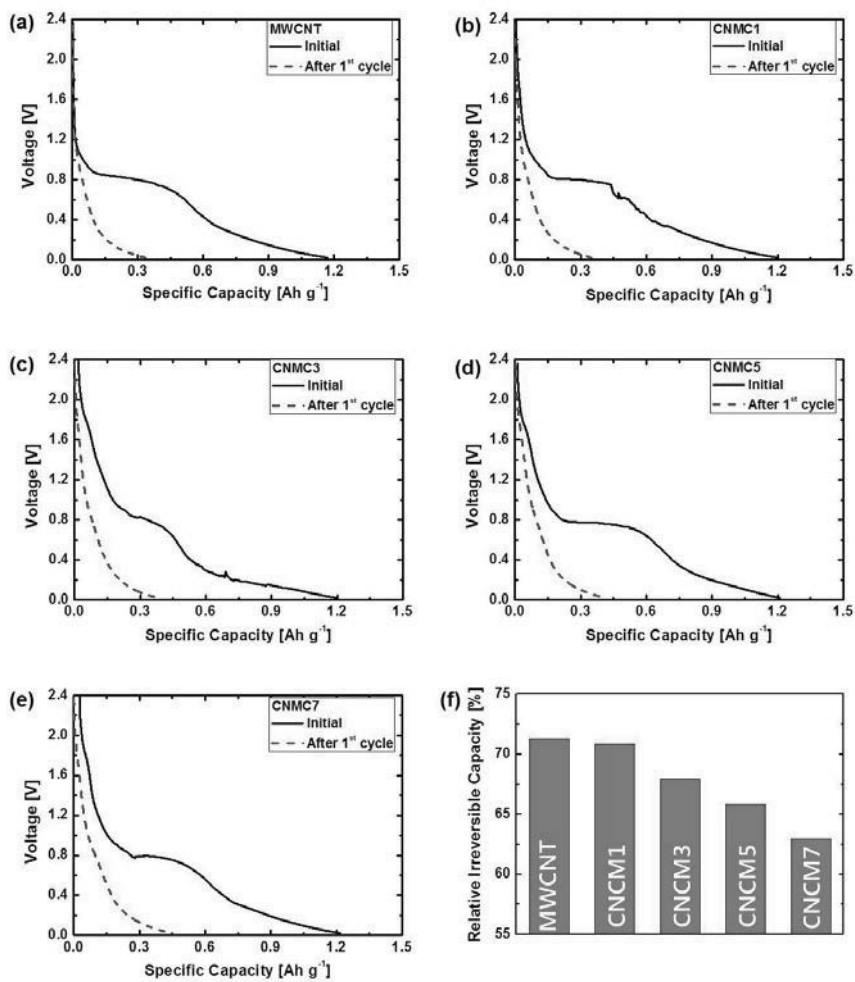


**Figure 6.9** (a–e) The discharge curves of half cells at 0.2 C rate in initial cycle and 1<sup>st</sup> cycle, which made by CNMC and MWCNT anodes. (f) A diagram of relative reversible capacity ( $C_I/C_0$ ) of half cells in 1<sup>st</sup> cycle, comparing the CNMC and MWCNT anodes.

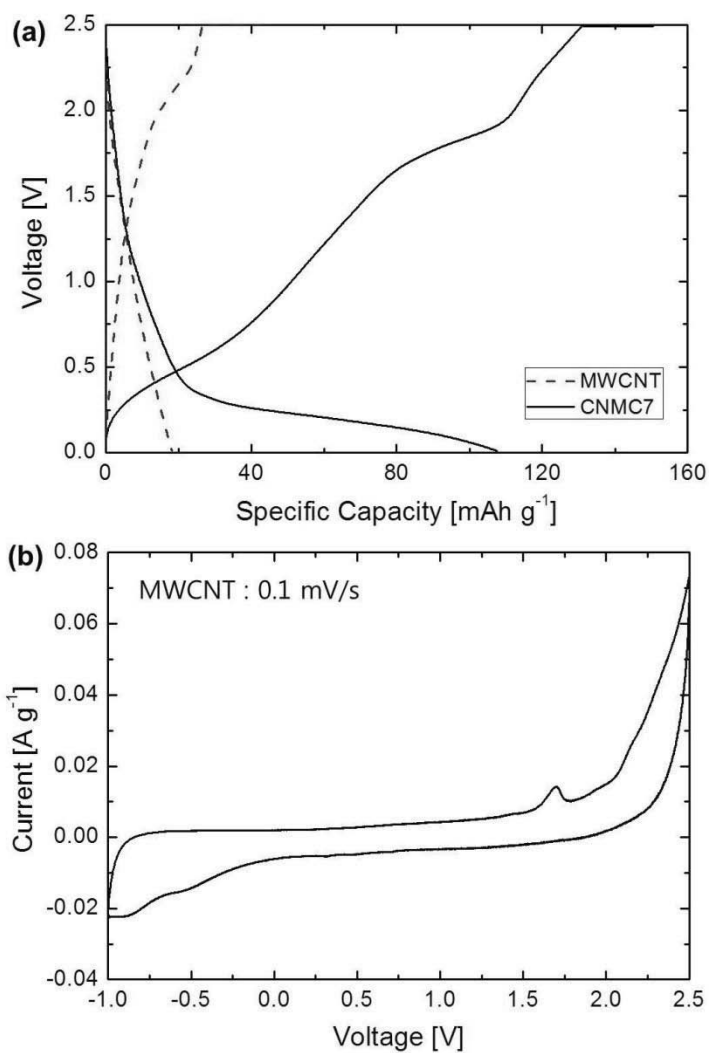


**Figure 6.10** (a) Charge/discharge curves of the full cells at 0.2 C in the 1<sup>st</sup> cycle, with anodes made of CNMC7 and MWCNT. (b) Cyclic voltammogram of an MWCNT electrode at a scan rate of 0.1 mV·s<sup>-1</sup> from -1.0 to 2.5 V (vs. Li/Li<sup>+</sup>).

### 6.3.4 Flexible lithium-ion battery

Because MWCNTs and CuNWs are flexible 1D nanomaterials, flexible LIBs can be developed using the proposed CNMC electrode system without conventional metal foil current collectors or binders. To fabricate binder-free flexible LIBs, we selected the  $\text{LiFePO}_4/\text{MWCNT}$  composite as the cathode. In contrast to their function in the anode, the MWCNTs function as a current collector in the cathode.  $\text{LiFePO}_4$  was used as the active material. Figures 6.11a–d show photographs of a flexible CNMC7 film and a red LED powered by a flexible LIB comprising a  $\text{LiFePO}_4/\text{MWCNT}$  composite cathode, a Poly(vinylidene fluoride-co-hexafluoropropylene) (PVDF-HFP)-based gel polymer electrolyte, and a CNMC7 anode. Ni-coated fiber tape was used as current-collecting leads in both electrodes, and polyurethane was used as the substrate and sealant. To demonstrate the discharge capacity and flexibility, the flexible LIB was measured after aging for 1 cycle and bent with a bending radius of 10 mm under a motion speed of  $25 \text{ mm}\cdot\text{s}^{-1}$  from 1 to 1,000 cycles using a lab-designed bending machine. The flexible LIB retained  $> 92.8\%$  of its capacity after 1,000 cycles of bending (Figure 6.11e). Compared with other flexible batteries, it exhibited high retention performance with a little degradation.<sup>[34–37]</sup>

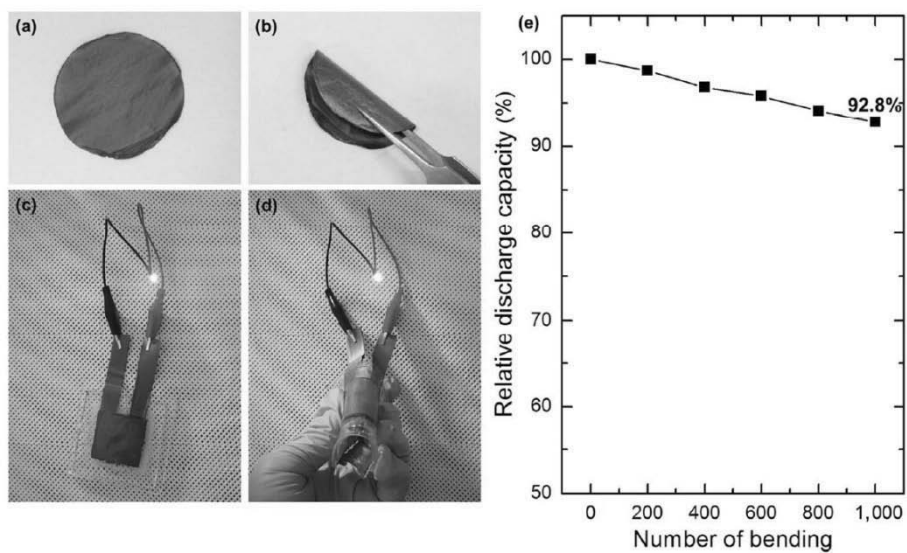


**Figure 6.11** (a, b) Photographs of a flexible CNMC7 anode film. (c, d) Red LED powered by a flexible LIB. (e) Relative discharge capacity ( $C/C_i$ ) of the flexible LIB after numerous bending cycles.

## 6.4 Conclusion

In summary, we demonstrated a new type of 3D structural composite anode to be applied for fast-charging/discharging LIBs without binders or conductive agents. The CuNWs used as the current collector and MWCNTs used as the active material provided significant advantages for improving the LIB performances, such as fast electron transport, efficient ion diffusion, thick electrode formation, and lightweight flexible cell design. Furthermore, the random CuNW network with 3D structure functioned as a rigid framework closely connected to the MWCNTs, not only preventing the shrinkage and expansion of the MWCNTs but also minimizing the effect of the volume change of the MWCNTs during the charging/discharging process. The CNMC7 anode effectively decreased the voltage range between the charging and discharging curves by reducing the anode resistance and was successfully used for full-cell LIBs. The CNMC7 anode for LIBs exhibited a high specific capacity and improved capacity retention with a high Coulombic efficiency even during high-C-rate operation. In addition, 92.8% of the capacity of a flexible LIB was retained after 1,000 cycles of bending. The proposed 3D conductive all-nanowire structure is a promising anode for LIBs for various electronic devices and EVs.

## References

- [1] T. Seba, *Clean Disruption of Energy and Transportation: How Silicon Valley Will Make Oil, Nuclear, Natural Gas, Coal, Electric Utilities and Conventional Cars Obsolete by 2030*, Silicon Valley: Clean Planet Ventures, California, USA **2014**.
- [2] L. D. Burns, *Nature* **2013**, 497, 181.
- [3] L. Li, C. Gao, A. Kovalchuk, Z. Peng, G. Ruan, Y. Yang, H. Fei, Q. Zhong, Y. Li, J. M. Tour, *Nano Res.* **2016**, 9, 2904.
- [4] X. Jia, Y. Lu, F. Wei, *Nano Res.* **2016**, 9, 230.
- [5] C. Kim, J. W. Jung, K. R. Yoon, D. Y. Youn, S. Park, I. D. Kim, *ACS Nano* **2016**, 10, 11317.
- [6] W. Liu, P. Oh, X. Liu, M.-J. Lee, W. Cho, S. Chae, Y. Kim, J. Cho, *Angew. Chem. Int. Ed.* **2015**, 54, 4440.
- [7] J. Xu, S. Dou, H. Liu, L. Dai, *Nano Energy* **2013**, 2, 439.
- [8] X. Chang, T. Wang, Z. Liu, X. Zheng, J. Zheng, X. Li, *Nano Res.* **2017**, 10, 1950.
- [9] W.-S. Kim, J. Choi, S.-H. Hong, *Nano Res.* **2016**, 9, 2174.
- [10] M.-S. Balogun, W. Qiu, Y. Luo, H. Meng, W. Mai, A. Onasanya, T. K. Olaniyi, Y. Tong, *Nano Res.* **2016**, 9, 2823.
- [11] M. Longo, D. Zaninelli, F. Viola, P. Romano, R. Miceli, M. Caruso, F. Pellitteri, "Recharge stations: A review" in *2016 Eleventh International Conference on Ecological Vehicles and Renewable Energies (EVER)*, **2016**, 1.
- [12] A. Thess, R. Lee, P. Nikolaev, H. Dai, P. Petit, J. Robert, C. Xu, Y. H. Lee, S. G. Kim, A. G. Rinzler, D. T. Colbert, G. E. Scuseria, D. Tomanek, J. E. Fischer, R. E. Smalley, *Science* **1996**, 273, 483.
- [13] L.-F. Cui, Y. Yang, C.-M. Hsu, Y. Cui, *Nano Lett.* **2009**, 9, 3370.
- [14] C. de las Casas, W. Li, *J. Power Sources* **2012**, 208, 74.

- [15] S. Ko, J.-I. Lee, H. S. Yang, S. Park, U. Jeong, *Adv. Mater.* **2012**, *24*, 4451.
- [16] Z. Yin, C. Lee, S. Cho, J. Yoo, Y. Piao, Y. S. Kim, *Small* **2014**, *10*, 5047.
- [17] Z. Yin, S. K. Song, D. J. You, Y. Ko, S. Cho, J. Yoo, S. Y. Park, Y. Piao, S. T. Chang, Y. S. Kim, *Small* **2015**, *11*, 4576.
- [18] Z. Yin, S. K. Song, S. Cho, D. J. You, J. Yoo, S. T. Chang, Y. S. Kim, *Nano Res.* **2017**, *10*, 3077.
- [19] J.-J. Sun, H.-Z. Zhao, Q.-Z. Yang, J. Song, A. Xue, *Electrochim. Acta* **2010**, *55*, 3041.
- [20] Q. Mu, D. L. Broughton, B. Yan, *Nano Lett.* **2009**, *9*, 4370.
- [21] Y. Won, A. Kim, D. Lee, W. Yang, K. Woo, S. Jeong, J. Moon, *NPG Asia Mater.* **2014**, *6*, e105.
- [22] W. Zhang, Z. Yin, A. Chun, J. Yoo, Y. S. Kim, Y. Piao, *ACS Appl. Mater. Interfaces* **2016**, *8*, 1733.
- [23] S.-J. Cho, K.-H. Choi, J.-T. Yoo, J.-H. Kim, Y.-H. Lee, S.-J. Chun, S.-B. Park, D.-H. Choi, Q. Wu, S.-Y. Lee, S.-Y. Lee, *Adv. Funct. Mater.* **2015**, *25*, 6029.
- [24] D. W. Dees, S. Kawauchi, D. P. Abraham, J. Prakash, *J. Power Sources* **2009**, *189*, 263.
- [25] D. Doughty, E. P. Roth, *Electrochem. Soc. Interface* **2012**, *21*, 37.
- [26] C. Hwang, T.-H. Kim, Y.-G. Cho, J. Kim, H.-K. Song, *Sci. Rep.* **2015**, *5*, 8623.
- [27] L.-L. Lu, J. Ge, J.-N. Yang, S.-M. Chen, H. Yao, F. Zhou, S.-H. Yu, *Nano Lett.* **2016**, *16*, 4431.
- [28] S.-H. Yu, S. H. Lee, D. J. Lee, Y.-E. Sung, T. Hyeon, *Small* **2016**, *12*, 2146.
- [29] G. Qin, Q. Ma, C. Wang, *Electrochim. Acta* **2014**, *115*, 407.
- [30] S. Luo, Y. Luo, H. Wu, M. Li, L. Yan, K. Jiang, L. Liu, Q. Li, S. Fan, J. Wang, *Adv. Mater.* **2017**, *29*, 1603549.
- [31] S. Yoon, S. Lee, S. Kim, K.-W. Park, D. Cho, Y. Jeong, *J. Power*

- Sources* **2015**, 279, 495.
- [32] L.-F. Cui, L. Hu, J. W. Choi, Y. Cui, *ACS Nano* **2010**, 4, 3671–3678.
- [33] T.-B. Song, Y. Chen, C.-H. Chung, Y. Yang, B. Bob, H.-S. Duan, G. Li, K.-N. Tu, Y. Huang, *ACS Nano* **2014**, 8, 2804.
- [34] Z. Pan, J. Ren, G. Guan, X. Fang, B. Wang, S. G. Doo, I. H. Son, X. Huang, H. Peng, *Adv. Energy Mater.* **2016**, 6, 1600271.
- [35] K. Fu, O. Yildiz, H. Bhanushali, Y. Wang, K. Stano, L. Xue, X. Zhang, P. D. Bradford, *Adv. Mater.* **2013**, 25, 5109.
- [36] M.-S. Balogun, C. Li, Y. Zeng, M. Yu, Q. Wu, M. Wu, X. Lu, Y. Tong, *J. Power Sources* **2014**, 272, 946.
- [37] J. G. Wang, D. Jin, R. Zhou, X. Li, X.-R. Liu, C. Shen, K. Xie, B. Li, F. Kang, B. Wei, *ACS Nano* **2016**, 10, 6227.

## Chapter 7. Conclusion

The synthesis and applications of copper nanowires (Cu NWs) and their nanocomposite are the critical issues, which have a great potential in functional electrodes development, such as solution-processable electrode, flexible electrode, foldable electrode, transparent electrode, annealing-free electrode, air-stable electrode and the combined electrode. However, the practical applications of Cu NWs and their nanocomposite have been strongly hindered by the various problems of difficult synthetic process, intrinsic materials properties, incompatible manufacturing conditions and complicated manufacturing steps. Therefore, the research that effectively solve these technical problems and successfully applied for various functional electrodes are extremely important.

Here, we focused the research on Cu NWs and their nanocomposites synthesis, included shape control, dispersibility and stabilization. Also, the fabrication process and device applications for special functional electrodes were investigated for next generational electronics, involving flexible transparent conductive electrode, wearable electrode and 3D current-collecting electrode. Furthermore, we put forward a lot of novel ways to solve several important technical issues in the electrode manufacturing

process. As a result, the functional electrodes with Cu NWs and their nanocomposites proposed in this dissertation substantially exhibited low sheet resistance, remarkable flexibility and excellent stability with simple solution-process ability.

We believe that the Cu NWs and their nanocomposites should be of interest to many researchers, and play a significant role for future device development.

# **(Appendix) Chapter 8. Rose Rock-shaped Nano Cu<sub>2</sub>O anchored Graphene for High-Performance Supercapacitors via Solvo-thermal Route**

## **8.1 Introduction**

Graphene (GN), a marvelous two-dimensional carbon nanomaterial with one-atom thickness, has a great promise for potential applications in batteries, sensors, and supercapacitors because of its ultra-thin nanostructure, excellent electronic and mechanical properties.<sup>[1-3]</sup> Recently, many researchers have focused on researching the electrochemical GN-based materials with high specific surface area and superior conductivity.<sup>[1, 4-10]</sup> Particularly, the GN-based materials have been designed for high-performance supercapacitors to enhance the power capability.<sup>[11]</sup> However, the exceptional inherent properties of GN are often declined by GN aggregation and stacking, which is driven by the strong pep interactions between individual GN sheets.<sup>[12]</sup> In addition, the quality of GN is hardly

controllable due to abundant chemical defects formed in the synthetic process. Therefore, the prevention of restacking and the reduction of chemical defects from GN has been a significant issue in developing GN-based electrochemical materials. The adding extra additives during the GN preparation process have been reported, which are demonstrated to overcome the above mentioned issues. Thus, various GN-based composites have been widely reported in the electrochemical application, such as transition metal oxide nanoparticles/GN,<sup>[4-6, 13, 14]</sup> carbon nanomaterials/GN,<sup>[15-17]</sup> conducting polymer/GN,<sup>[18]</sup> and etc. Actually, the extra additive deposited on the surface of GN as a nanospacer can restrain the restacking of GN during the reduction of GO. Moreover, GN not only offers a 2D conductive backbone for the rapid electron transport, but also allows the decoration by uniform additives to facilitate the utilization of electrode materials.

Among the transition metal oxides, Cuprous oxide ( $\text{Cu}_2\text{O}$ ) has the unique optical and good electrochemical properties,<sup>[19-21]</sup> which makes it a promising candidate in many applications, such as supercapacitors,<sup>[22]</sup> solar-energy conversion devices,<sup>[23]</sup> and lithium-ion batteries,<sup>[24]</sup> etc. Furthermore, the shape-controlled syntheses of various nanostructured  $\text{Cu}_2\text{O}$ , including nanoparticles,<sup>[25]</sup> nanocubes,<sup>[26]</sup> nanocages,<sup>[20]</sup> nanowires,<sup>[27]</sup> and poly-

hedrons,<sup>[28]</sup> have been achieved by abundant routes.<sup>[29, 30]</sup> Therefore, different nanostructures of Cu<sub>2</sub>O furnish the feasibility of their application in supercapacitors, because the nanostructure can improve the electrochemical performance. The Cu<sub>2</sub>O/CuO/RGO composites with high capacity (173.4 F·g<sup>-1</sup> at 1 A·g<sup>-1</sup>) was one-step synthesized through a hydrothermal-assisted reaction between Cu and GO. In addition, its capacity retained 98.2% after 100,000 cycles at 10 A·g<sup>-1</sup>.<sup>[31]</sup> Dong et al. reports the 3D binder-free Cu<sub>2</sub>O nanoneedle on a Cu foil for an asymmetric supercapacitor with an 862 F·g<sup>-1</sup> specific capacitance.<sup>[22]</sup>

However, most of the morphology controlled synthetic routes are usually limited to the framework of “ion-by-ion” nanocrystal growth, and surfactants play a complicated factor in the shape control of Cu<sub>2</sub>O by versatile soft templates and self-assembly.<sup>[32]</sup> Moreover, fabrication of higher ordered three-dimensional (3D) nanostructures and simplification of the synthetic process are still imperative solved issues for current synthesis of Cu<sub>2</sub>O. Recently, some studies have reported ordered Cu<sub>2</sub>O nanomaterial-GN with novel physiochemical properties due to the structural directing effect of GO for preparing Cu<sub>2</sub>O nanocomposites.<sup>[33-35]</sup> Deng et al. utilized GO as molecular templates to form uniformly GN-conjugated nanowire mesocrystals under hydrothermal conditions.<sup>[33]</sup> Cu<sub>2</sub>O mesocrystals on the

large GN sheets were consisted of highly anisotropic nanowires with a distinct octahedral morphology. Especially, the GN-based  $\text{Cu}_2\text{O}$  nanocomposites exhibited excellent electrochemical performance with the synergistic effect between GN and transition metal oxides. For example,  $\text{Cu}_2\text{O}$  nanoparticle@GN, which was prepared by using glucose as reducing agent, showed a good capacity value ( $31.0 \text{ F}\cdot\text{g}^{-1}$  at  $0.1 \text{ A}\cdot\text{g}^{-1}$ ) and stable cycling behavior.<sup>[36]</sup> However, these mentioned methods still have the unsolved problems for regarding nano- $\text{Cu}_2\text{O}$  decoration of GN: (1) the adopted chemical ways are usually complicated using numerous reducing, precipitating, and stabilizing agents.<sup>[37-39]</sup> (2) The growth of uniform nanomaterials on GN often lacks for favorable control in the whole reaction process. (3) It is still a challenge to achieve the convenient production of GN-based  $\text{Cu}_2\text{O}$  composites.

To overcome these shortcomings, we used a one-pot solvothermal method to prepare rose rock-shaped  $\text{Cu}_2\text{O}$  anchored GN nanocomposites ( $\text{Cu}_2\text{O}$ -GN) with the presence of copper (II) chloride, sodium acetate (NaAc) and GO. Solvothermal processes are one of the best ways to fabricate nanomaterials for the convenient operation, mild synthetic conditions, and low cost.<sup>[40]</sup> Moreover solvothermal reactions often provide a direct way for the fabrication of a wide diversity with different morphology and

crystallinity. Because variation of the reaction conditions drastically affects the process of the reactions and the structure of the resulting products.

In this work, the rose rock-shaped  $\text{Cu}_2\text{O}$  formed on GN had distinct crystal faces and was constituted by highly anisotropic nanoflakes as building blocks. A simple and convenient route to non-surfactant assisted growth of uniform nano- $\text{Cu}_2\text{O}$  was proposed by GO, which would be more efficient controllable for the formation of ordered nano- $\text{Cu}_2\text{O}$ . The role of GO in the transformation of  $\text{Cu}_2\text{O}$  nanostructure from 0D to 3D was evaluated. In addition, the effects of GO, precursor, precipitating agent, and heating rate in the solvothermal process were also investigated, which revealed the formation mechanism of the product. As supercapacitor materials, the  $\text{Cu}_2\text{O}$ -GN nanocomposites possessed a good electrical capacitance because of the synergistic combination of highly conductive GN and well capacitive  $\text{Cu}_2\text{O}$ . The study aims were to provide a model to adequately account for the formation mechanism of ordered nano  $\text{Cu}_2\text{O}$  at the assistance of GO, and to exploit new possibilities for nano  $\text{Cu}_2\text{O}$  as electrode materials for supercapacitors

## 8.2 Experimental section

### 8.2.1 Reagents

$\text{CuCl}_2 \cdot 2\text{H}_2\text{O}$ , sodium acetate (NaAc), ethylene glycol, and graphite (<20  $\mu\text{m}$ ) were purchased from Sigma-Aldrich. All chemicals were of analytic grade and used as received without further purification. Deionized water was filtered by using a water-purification system (UP90 model, Seoul, South Korea). Graphene oxide (GO) and graphene (GN) was prepared from graphite powder by an improved Hummers method.<sup>[41, 42]</sup>

### 8.2.2 Apparatus

Sample morphologies were characterized by carrying out field emission scanning electron microscopy (SEM, Hitachi S-4800). A Transmission electron microscopy (TEM) instrument equipped with a field emission gun and was used for high-resolution TEM measurements (JEOL, JEM-2010) at 200 kV. The powder X-ray diffractions of spectra (XRD) were measured by X-ray diffraction (Bruker, D8-Advance) with Cu K $\alpha$  radiation,  $\lambda = 1.542 \text{ \AA}$ . X-ray photoelectron spectroscopy (XPS) experiments were performed by a

Sigma Probe (KRATOS, AXIS-HSi) with a monochromatic Al K $\alpha$  (1486.6 eV) X-ray source at a constant power of 100 W (15 kV and 10 mA) and beam diameter of 400  $\mu$ m. Electrochemical tests were performed on an electrochemical workstation (CH Instruments, 660E), and the electrolyte used was 6 mol·L<sup>-1</sup> aqueous KOH solution.

### **8.2.3 Preparation of Cu<sub>2</sub>O-GN composite**

The Cu<sub>2</sub>O-GN nanocomposite was successfully synthesized through the solvothermal method. The optimized preparation was as follows: 0.0006 mol CuCl<sub>2</sub>·2H<sub>2</sub>O, 0.03 g of GO, and 0.05 g of NaAc were dissolved into 0.01 L of ethylene glycol by stirring for 12 h. The mixture was sealed in a Teflon-lined autoclave and maintained at 160 °C for 20 h. Solid precipitates were collected by centrifugation (8000 rpm) after the end of the reaction. To remove the residual metal ions and organic moiety, the products were washed 3 times by using ethanol. Finally, the product was dried in vacuum at 60 °C for 24 h. To explore the formation mechanism of Cu<sub>2</sub>O-GN, several synthetic parameters were changed in a series of parallel experiments, including the concentrations of NaAc, GO, CuCl<sub>2</sub>, and heating rate.

## 8.2.4 Electrochemical testing

An electrode was fabricated by mixing 70 wt% of Cu<sub>2</sub>O-GN, 15 wt% acetylene black, and 15 wt% of polyvinylidene difluoride in N-methyl-2-pyrrolidinone. The weight of active materials was 3 mg. Then, the slurry was coated on a pretreated battery-grade polished Ni foil (area of coating: 1 cm<sup>2</sup>, and foil thickness: 0.2 mm) for electrical conductivity and vacuum-dried at 60 °C for 24 h. An Hg/HgO electrode as the reference electrode, the asprepared electrode as the working electrode, and a platinum wire electrode as the counter electrode were used in a three-electrode cell. Cyclic voltammetry (CV) and charge-discharge were tested by various scan rates and current densities, respectively.

## 8.3 Results and discussion

### 8.3.1 Characterization of Cu<sub>2</sub>O-GN composite

One-step solvothermal synthesis was used to design rose rock-shaped Cu<sub>2</sub>O-GN composite with the reaction of GO, CuCl<sub>2</sub>, and NaAc in ethylene glycol. In previous research,<sup>[6, 13]</sup> the similar method was successfully utilized for preparing the metal oxide-GN nanocomposites with simultaneous reduction of GO and formation of nanoparticles. It not only avoided the aggregation of GN in the reduction process but also obtained well-dispersed GN-nanoparticle composite conveniently. Therefore, we tried to prepare the Cu<sub>2</sub>O-GN composites by solvothermal process.

Figure 8.1a shows the XRD profile of the Cu<sub>2</sub>O-GN composite. The position and relative intensity of diffraction peaks matched well with standard XRD data for Cu<sub>2</sub>O (JCPDS 00-005-0667), and no peaks of copper oxide (CuO) were observed. The peaks at  $2\theta = 36.3, 42.3,$  and  $61.4^\circ$  were ascribed to the (111), (200), and (220) reflections of Cu<sub>2</sub>O, respectively. Moreover, the XRD pattern of Cu<sub>2</sub>O-GN showed a broad diffraction peak appeared around  $23^\circ$ , corresponding to the C (002) reflection, which was consistent with GN and indicated GO reduction in the reaction process.<sup>[43, 44]</sup>

These appearing XRD peaks confirmed that  $\text{Cu}_2\text{O}$  was formed on GN by the solvothermal method. In addition, two peaks at about  $43.3^\circ$  and  $50.4^\circ$  were ascribed to Cu (JCPDS 00-004-0836), because a small amount of copper was formed by the reduction of ethylene glycol.<sup>[13]</sup>

The morphology of the rose rock-shaped  $\text{Cu}_2\text{O}$ -GN was characterized by TEM and fast Fourier transform (FFT) patterns. In Figure 8.1b, a low magnification TEM image was clearly observed that  $\text{Cu}_2\text{O}$  anchored on the surface of the GN with a rose rock-shaped structure. The average size of composite is about 400 nm without the aggregations of  $\text{Cu}_2\text{O}$  and large vacancies on GN. The TEM image of the rose rock-shaped  $\text{Cu}_2\text{O}$  on GN with a high magnification was shown in Figure 8.1c. The thin nanoflakes (about 10 nm thick, 150 nm wide and 150 nm long) as petals constituted the rose rock-shaped  $\text{Cu}_2\text{O}$ . The result showed that GN could furnish an ideal surface for anchoring electrochemical molecules, while  $\text{Cu}_2\text{O}$  provided a high accessible surface area with many chemical active sites for rapid mass transfers. The high magnification TEM image was seen to further understand the dimensionality of  $\text{Cu}_2\text{O}$ -GN morphologies. Figure 8.1d exhibits clear lattice fringes with  $d$  spacings of 2.12, 2.46, and 3.02 Å, corresponding to the (200), (111), and (110) planes of  $\text{Cu}_2\text{O}$ , respectively.<sup>[45]</sup> Figure 8.1e shows the ring patterns of FFT, indicating the polycrystalline

nature of rose rock-shape. The rings in the pattern were indexed as the (110), (111), (200), and (220) rings of  $\text{Cu}_2\text{O}$ , in agreement with the above results. The content of  $\text{Cu}_2\text{O}$  in  $\text{Cu}_2\text{O}$ -GN was calculated as 33 wt% by TG measurement.

The XPS is one of best methods to investigate the chemical composition and electronic structure of the  $\text{Cu}_2\text{O}$ -GN. Figure 8.2 show the wide scan and deconvoluted XPS spectra of  $\text{Cu}_2\text{O}$ -GN and GO. The elements of Cu, C, and O were clearly observed in Figure 8.2a. Figure 8.2b and c show both the C 1s XPS spectra of GO and  $\text{Cu}_2\text{O}$ -GN, which can be deconvoluted into three peaks: C 1s peak of C–C (284.6 eV), C–O (286.6 eV), and C=O (288.3 eV), respectively. It was found that the C1s intensities of C–O and C=O in  $\text{Cu}_2\text{O}$ -GN composite became weaker dramatically than those of GO, revealing that the deoxygenation process accompanied the reduction of GO in the solvothermal reaction. These change proved that GO was reduced to GN with a small amount of residual oxygen-containing groups when  $\text{Cu}_2\text{O}$ -GN composite was prepared, because ethylene glycol was used as an effective reducing agent.<sup>[46, 47]</sup>

The binding energy values of Cu 2p observed in the high-resolution XPS spectra in Figure 8.2d, which implied that  $\text{Cu}_2\text{O}$  were present in the composite. Two peaks at 933.4 and 953.3 eV were clearly observed

corresponding to the Cu 2p<sub>3/2</sub> and Cu 2p<sub>1/2</sub> peaks of Cu<sup>+</sup>, respectively. The results confirmed the existence of Cu<sub>2</sub>O in the composites.<sup>[48]</sup> Meanwhile, there was an absence of weak satellites on the higher binding-energy side of the Cu 2p<sub>3/2</sub> peak, which further confirmed the absence of Cu<sub>2</sub>O on the surface of GN.<sup>[49]</sup> These results revealed that the one-step solvothermal method featured the reduction of GO as well as formation of Cu<sub>2</sub>O efficiently.

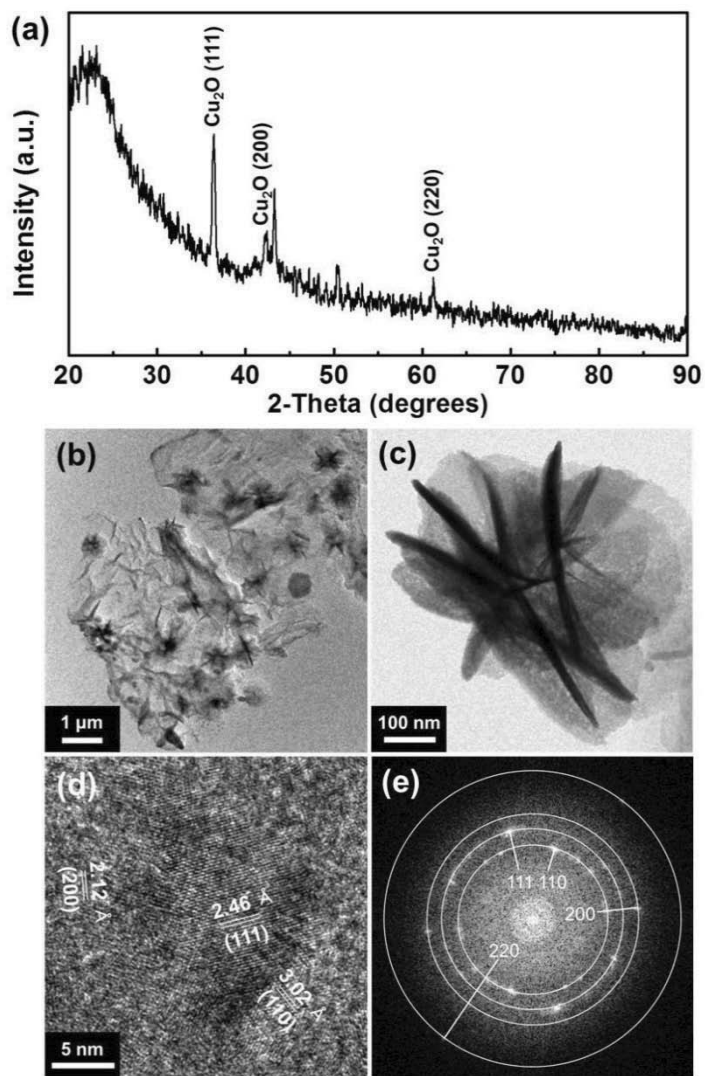


**Figure 8.1** (a) XRD pattern of rose rock-shaped  $\text{Cu}_2\text{O}$ -GN composite. (b) TEM image of rose rock-shaped  $\text{Cu}_2\text{O}$ -GN composite. (c) High magnification TEM image of representative  $\text{Cu}_2\text{O}$ -GN composite. (d) HR-TEM image of  $\text{Cu}_2\text{O}$  surface with three different fringe lattices spacing, and corresponding (e) FFT pattern.

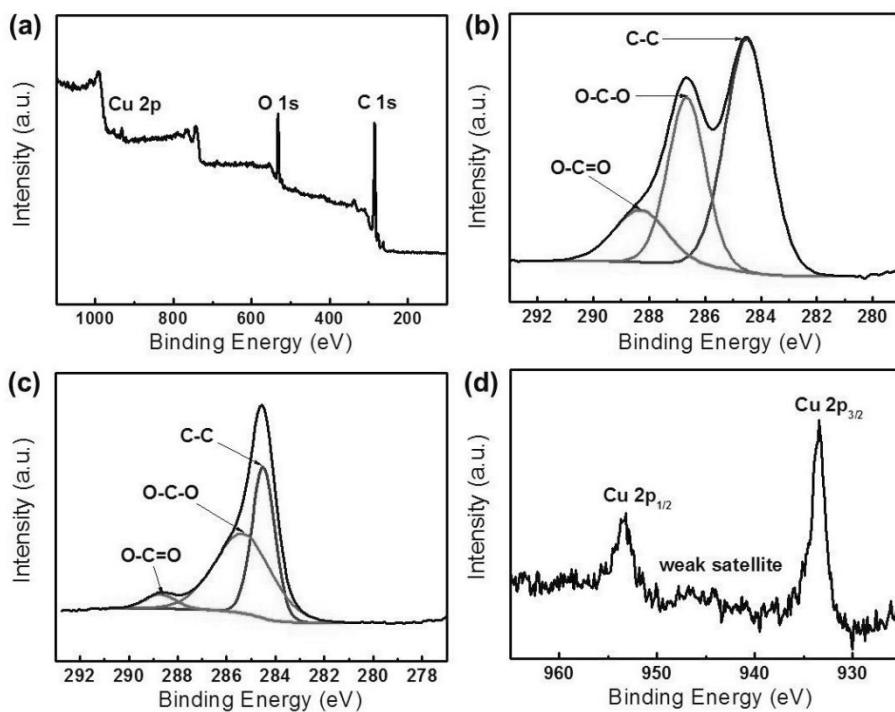


**Figure 8.2** (a) Wide scan XPS spectra of Cu<sub>2</sub>O-GN, deconvoluted XPS spectra of (b) GO and (c, d) Cu<sub>2</sub>O-GN.

### 8.3.2 Formation mechanism of Cu<sub>2</sub>O-GN composite

During the preparation of metal oxide nanostructures by the solvothermal method, we found that the synthetic conditions were the significant factors for the quality of the obtained nanomaterial. For that reason, the potential influencing factors in the process were studied to understand the formation mechanism of Cu<sub>2</sub>O-GN.

First of all, the morphology change of Cu<sub>2</sub>O-GN was studied in the presence and absence of PVP, as shown in Figure 8.3. Other conditions were fixed in 0.06 mol·L<sup>-1</sup> CuCl<sub>2</sub>, 1 g·L<sup>-1</sup> GO, 5 g·L<sup>-1</sup> NaAc, and 10 mL of ethylene glycol at 160 °C for 20 h. When PVP was added, some particles with random large size (from 0.2 to 1 μm) were generated, and the formation of pure copper instead of Cu<sub>2</sub>O. The nanoparticles were difficult to find on the surface of GN in Figure 8.3a and b with a high magnification, which indicated that PVP could not cause decoration of nano Cu<sub>2</sub>O on GN. Moreover, PVP in this system might be form micelles with Cu<sup>2+</sup> ions, resulting in the random metallic copper by the reduction of ethylene glycol. Figure 8.3c and d shows GN sheets covering the dense Cu<sub>2</sub>O nanoparticles with about 15 nm, demonstrating that GO both induce and stabilize the Cu<sup>2+</sup>-GO complexes for subsequent particle-mediated crystallization in the

solvothermal reaction.<sup>[33, 50]</sup> In this system, the surface of GO has a strong affinity to  $\text{Cu}^{2+}$  due to abundant functional groups on quasi-2D GO which has some molecule-colloid properties as well as a surfactant.<sup>[51]</sup> GO could moreover adopt particular crystallographic facets of the growing crystal as a capping agent,<sup>[13]</sup> which impeded the growth of random Cu particles. The results showed that GO was a key factor in promoting the synthesis of nano  $\text{Cu}_2\text{O}$ .

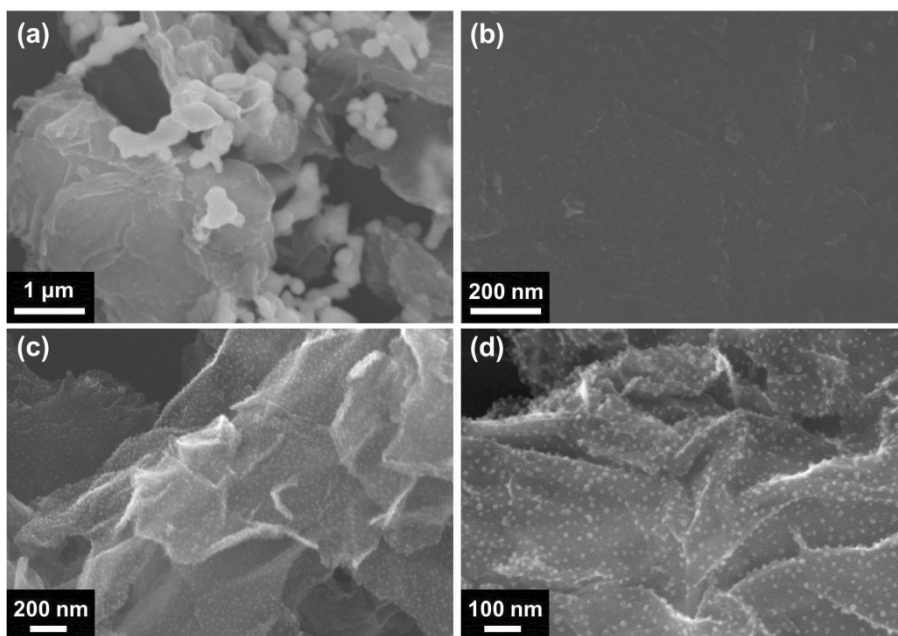


**Figure 8.3** SEM images with low magnification and high magnification of Cu<sub>2</sub>O-GN composite prepared by the different concentrations of PVP (g·L<sup>-1</sup>): (a, b) 10 and (c, d) 0. Other conditions: 0.06 mol·L<sup>-1</sup> CuCl<sub>2</sub>, 5 g·L<sup>-1</sup> NaAc, 1 g·L<sup>-1</sup> GO, 160 °C, 20 h.

To investigate the effect of the concentration of GO on Cu<sub>2</sub>O nanostructures, a series of experiments were carried out by changing the concentration of GO (1–3 g·L<sup>-1</sup>). Other conditions were fixed (0.06 mol·L<sup>-1</sup> CuCl<sub>2</sub>, 5 g·L<sup>-1</sup> NaAc, and 10 mL of ethylene glycol at 160 °C and 20 h). The SEM results are shown in Figure 8.4a–c. When 1.0 g·L<sup>-1</sup> GO was in the initial solution, Cu<sub>2</sub>O was prepared for uniform nanoparticles with an average diameter of 15 nm, and randomly distributed on GN sheets. This implied that Cu<sub>2</sub>O growth rates in various directions were almost similar to that with low concentration of GO. In addition, the concentration of GO was increased to 2.0 g·L<sup>-1</sup>, Cu<sub>2</sub>O nanoflakes as the main products were formed on GN instead of the Cu<sub>2</sub>O nanoparticles, as shown in Figure 8.4b. The variation of the shape might be ascribed to the increasing numbers of oxygen functional group on GO surface,<sup>[52, 53]</sup> which brought about a substantial alteration in the nano Cu<sub>2</sub>O growth process. Figure 8.4c shows a SEM image of Cu<sub>2</sub>O-GN obtained in 3.0 g·L<sup>-1</sup> GO. It was clearly seen that the uniform rose rock-shaped Cu<sub>2</sub>O from the assembled nanoflakes was distributed on GN, which was consistent with the TEM results. Furthermore, the size of nano Cu<sub>2</sub>O became bigger when GO amount enhanced.

On the basis of the experimental results, GO extremely affected the nanostructure of Cu<sub>2</sub>O. In the absence of GO, the growth mechanism

usually followed classical ion-by-ion growth and the surfactant promoted the anisotropic growth of copper.<sup>[54]</sup> When adding GO, a transition from copper to Cu<sub>2</sub>O occurred. GO as a unique material exhibiting molecule-colloid features could control nanostructures of metallic oxides because of its essential single atomic sheet with various functional groups.<sup>[51]</sup> In the synthetic process of nano Cu<sub>2</sub>O, GO was used as a capping agent and hard template. On the one hand, the rich oxygen functional groups suppressed the reduction of copper by ethylene glycol. On the other hand, GO conjugated with copper ions due to the functional group decorating the basal planes and edges of GO, causing the crystal growth of Cu<sub>2</sub>O on its surface. With the concentration of GO increasing, more Cu<sup>2+</sup> and GO could self-assemble and form the complexes due to electrostatic interactions. Thus, the Cu precursor changed into a radial aggregated structure and begun to the growth of Cu<sub>2</sub>O nucleation along the 1D direction on the surface of GN, owing to the anisotropic crystal structure.<sup>[55]</sup> As the reaction proceeded, the nuclei was gradually surrounded to form Cu<sub>2</sub>O nanoflake. If the concentration of GO continued to increase, rose rock-shaped Cu<sub>2</sub>O would be fabricated with the assist of GO. Firstly, Cu<sub>2</sub>O nanoflakes were formed on GN which provided more growth sites for further variation of Cu<sub>2</sub>O. Then, a sufficient amount of GO/Cu<sup>2+</sup> was supplied to enough precursor of

Cu<sub>2</sub>O crystals. Finally, the presynthesized Cu<sub>2</sub>O nanoflake as growth units centralized Cu<sup>2+</sup> precursor in order to form rose rock-shaped Cu<sub>2</sub>O under a large concentration of GO. This was a fascinating phenomenon in our one-step reactions and would give significant implications for preparing uniform nanostructures with GO concentration.

In the synthesis NaAc was a very useful precipitation agent.<sup>[13]</sup> Figure 8.4d–f shows Cu<sub>2</sub>O-GN composite prepared by with different concentrations of NaAc (1, 5 and 10 g·L<sup>-1</sup>). The reaction was based on a mixture of 0.06 mol·L<sup>-1</sup> CuCl<sub>2</sub>, 3 g·L<sup>-1</sup> GO, and 10 mL of ethylene glycol at 160 °C for 20 h. When 1 g·L<sup>-1</sup> NaAc was used, no Cu<sub>2</sub>O nanoparticles were formed on the surface of GN (Figure 8.4d). As the concentration of NaAc increased to 5 g·L<sup>-1</sup>, the composite was mainly composed of rose rock-shaped Cu<sub>2</sub>O-GN, as shown in Figure 8.4e; When the concentration of NaAc was further up to 10 g·L<sup>-1</sup>, random Cu particles with 1.5–4 μm formed on GN without rose rock-shaped Cu<sub>2</sub>O, as see in Figure 8.4f. It was meant that the optimized concentration of NaAc was important for the generation of Cu<sub>2</sub>O nanomaterial in the system.

As a precipitation agent, the NaAc had a significant influence on morphology control of metal oxides because of its regulation to pH and the interaction with metal ion precursors.<sup>[13, 56, 57]</sup> In the solvothermal method,

the formation of Cu<sub>2</sub>O nanomaterial involving three steps (the nucleation, growth, and assembly of nanocrystals) was strongly depended on the solution pH.<sup>[55]</sup> The effect of the NaAc concentration on the morphology of Cu<sub>2</sub>O could be explained as follows. When the amount of NaAc was low, the growth of Cu<sub>2</sub>O nucleation might be prevented. Therefore Cu<sub>2</sub>O were hardly formed on the surface of GN. When the concentration of NaAc was much exceeded to the synthetic condition of nano Cu<sub>2</sub>O, the excess of OH<sup>-</sup> was generated, which would accelerate the dissociation of copper ion/GO complexes. As a result, Cu nanocrystal was agglomerated and formed random copper precipitations by the reduction of ethylene glycol. From the above, the concentration of NaAc that was too high or low could not contribute to the formation of uniform rose rock-shaped Cu<sub>2</sub>O-GN nanocomposites.

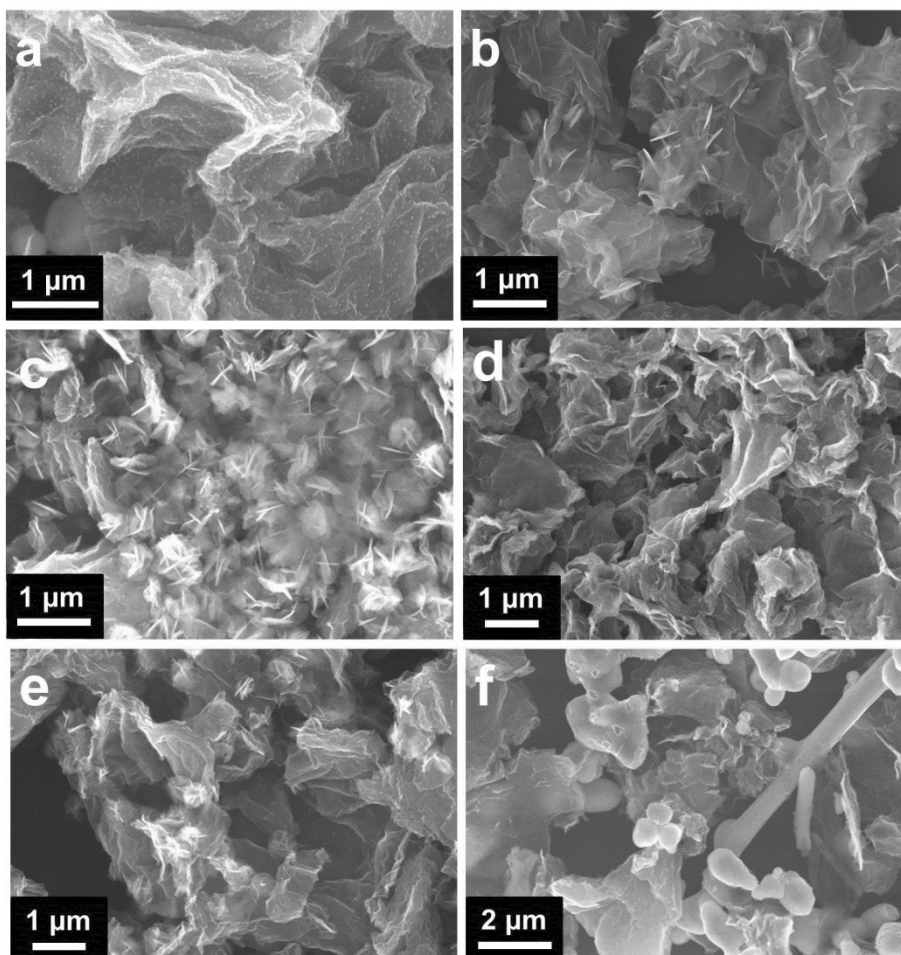


**Figure 8.4** (a–c) SEM images of Cu<sub>2</sub>O-GN composite prepared by the different concentrations of GO (g·L<sup>-1</sup>): (a) 1, (b) 2, and (c) 3. Other conditions: 0.06 mol·L<sup>-1</sup> CuCl<sub>2</sub>, 5 g·L<sup>-1</sup> NaAc, 160 °C, 20 h. Additionally, (d–f) SEM images of Cu<sub>2</sub>O-GN composite prepared by the different concentrations of NaAc (g·L<sup>-1</sup>): (d) 1, (e) 5, and (f) 10. Other conditions: 0.06 mol·L<sup>-1</sup> CuCl<sub>2</sub>, 3 g·L<sup>-1</sup> GO, 160 °C, 20 h.

In the solvothermal process, the initial concentration of the precursor should be another important factor for preparing Cu<sub>2</sub>O-GN. Figure 8.5a and b shows the SEM images of the Cu<sub>2</sub>O-GN composite under precursor concentrations of 0.06 or 0.12 mol·L<sup>-1</sup> CuCl<sub>2</sub>. It was clearly seen that the concentration of the precursor affected the size and dispersion of Cu<sub>2</sub>O-GN. At a low concentration of precursor, regular morphology of Cu<sub>2</sub>O formed on GN (Figure 8.5a). When the more precursors were added, the size of Cu<sub>2</sub>O increased and the shape of Cu<sub>2</sub>O became irregular (Figure 8.5b). The effect of precursor concentration was followed by the theory of Von Weimarn,<sup>[58]</sup> which explained the nucleation and nanocrystal growth in solution system. Firstly, the nucleation occurred within a very limited time, then nanocrystal growth sustained a comparable time. When the concentration of the precipitation agent was retained, the number of the growth nanocrystal was entirely dependent on the concentration of the precursor. It explained that the high precursor concentration leads to more nanocrystal assemble. Hence, the size and shape of samples altered in trend with the concentration of the precursor.

Besides the above conditions, the heating rate was another necessary factor in the synthesis of Cu<sub>2</sub>O-GN. We controlled the heating rate (6 and 3 °C·min<sup>-1</sup>) from 25 to 160 °C in the reaction process. Cu<sub>2</sub>O-GN was obtained

in the optimum condition of 10 mL ethylene glycol,  $0.06 \text{ mol}\cdot\text{L}^{-1}$   $\text{CuCl}_2$ ,  $5 \text{ g}\cdot\text{L}^{-1}$  NaAc,  $3 \text{ g}\cdot\text{L}^{-1}$  GO at  $160 \text{ }^\circ\text{C}$  for 20 h. When the heating rate was  $6 \text{ }^\circ\text{C}\cdot\text{min}^{-1}$ , the precursor was reduced rapidly by EG before the formation of rose rock-shaped nanostructure of  $\text{Cu}_2\text{O}$ . As a result, irregular-shaped  $\text{Cu}_2\text{O}$  structures were obtained on the surface of GN (Figure 8.5c). Otherwise, at the heating rate of  $3 \text{ }^\circ\text{C}\cdot\text{min}^{-1}$ , rose rock-shaped  $\text{Cu}_2\text{O}$ -GN was formed in Figure 8.5d. With the slow heating rate, the precursor had enough time to form the stable state of  $\text{Cu}_2\text{O}$ , because the suitable heating rate was helpful to the nucleation and nanocrystal growth.<sup>[59]</sup> However, too rapid heating rate could inhibit the nucleation rate which was not conducive to formation of rose rock-shaped  $\text{Cu}_2\text{O}$ .

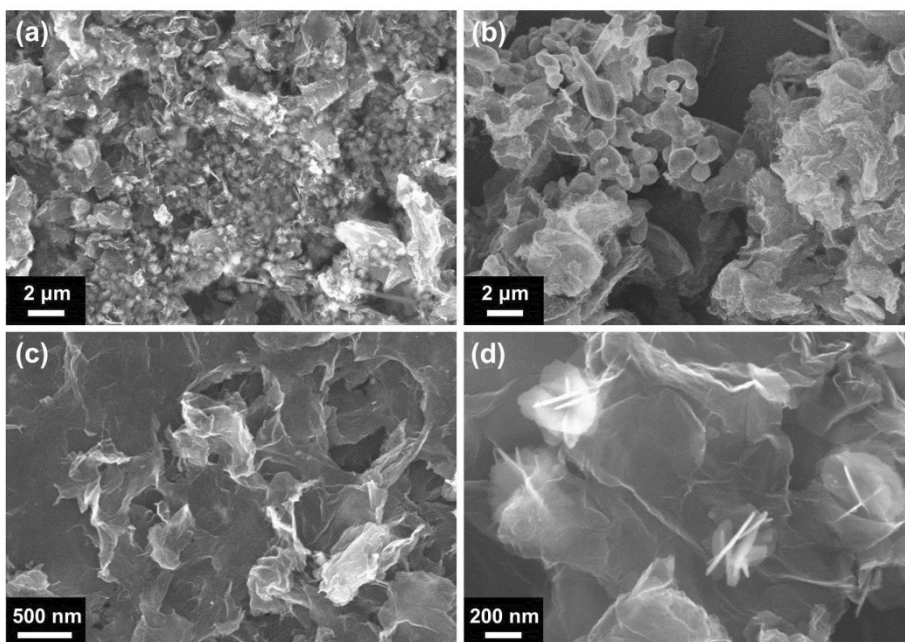
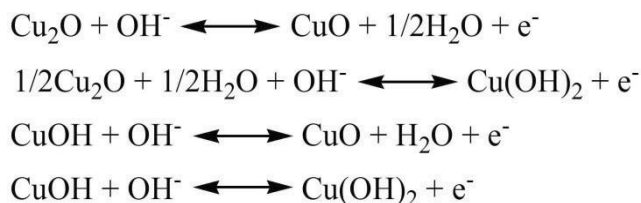


**Figure 8.5** (a, b) SEM images of  $\text{Cu}_2\text{O}$ -GN composite prepared by the different concentrations of  $\text{CuCl}_2$  ( $\text{mol}\cdot\text{L}^{-1}$ ): (a) 0.06 and (b) 0.12. Other conditions:  $3\text{ g}\cdot\text{L}^{-1}$  GO,  $5\text{ g}\cdot\text{L}^{-1}$  NaAc,  $160\text{ }^\circ\text{C}$ , 20 h. Additionally, (c, d) SEM images of  $\text{Cu}_2\text{O}$ -GN composite prepared by the different heating rate ( $^\circ\text{C}\cdot\text{min}^{-1}$ ): (c) 6 and (d) 3. Other conditions:  $0.06\text{ mol}\cdot\text{L}^{-1}$   $\text{CuCl}_2$ ,  $3\text{ g}\cdot\text{L}^{-1}$  GO,  $5\text{ g}\cdot\text{L}^{-1}$  NaAc,  $160\text{ }^\circ\text{C}$ , 20 h.

### 8.3.3 Electrochemical tests

In this work, the electrochemical performance of Cu<sub>2</sub>O-GN was examined by CV and galvanostatic charge-discharge measurements. In the electrochemical tests, 6 mol·L<sup>-1</sup> KOH was chosen as the electrolyte. Figure 8.6a illustrates the CV curves of Cu<sub>2</sub>O-GN composites and GN from -1.0 to 0.0 V vs. Hg/HgO at a scan rate of 0.05 V·s<sup>-1</sup>. The CV curve of GN revealed a rectangle-like shape which was ascribed to the electric double-layer capacitance of GN. However, the CV curve of Cu<sub>2</sub>O-GN clearly showed similar shape accompanied by typical redox peaks of Cu<sub>2</sub>O. It suggested that the capacitances of Cu<sub>2</sub>O-GN originated from both electric double-layer capacitance of GN and pseudocapacitance of Cu<sub>2</sub>O. Compared with GN, a larger encircling area of Cu<sub>2</sub>O-GN meant higher specific capacitance of Cu<sub>2</sub>O-GN. Based on literature,<sup>[53, 60, 61]</sup> the possible reactions of Cu<sub>2</sub>O on GN in alkaline electrolytes are as follow:



In Figure 8.6a the CV curve of Cu<sub>2</sub>O-GN presents two anodic peaks (a1 – 0.42 V and a2 –0.13 V) and a broad cathodic peak (c1 –0.64 V) because of

the high electrolyte concentration of alkaline solution.<sup>[31, 62]</sup> On the one hand, the peak a1 was corresponded to the oxidation of Cu<sub>2</sub>O to CuO, and the peak a2 was attributed due to the oxidation of Cu<sub>2</sub>O to both CuO and Cu(OH)<sub>2</sub>. On the other hand, the cathodic peak may be due to the reduction of CuO and Cu(OH)<sub>2</sub>. The result was similar to the redox of Cu<sub>2</sub>O.<sup>[60, 61, 63]</sup>

The specific capacitances of Cu<sub>2</sub>O-GN with increasing discharge current (1.0, 3.0, and 5.0 A·g<sup>-1</sup>) were also confirmed by Figure 8.6. galvanostatic charge-discharge curves, as shown in Figure 8.6b. The nearly symmetric charge-discharge curves demonstrated the capacitive behavior of electrical double layer capacitance and pseudocapacitance, and definitely showed Cu<sub>2</sub>O-GN had the larger capacity, which was consistent with the CV results. The specific capacitance of the composite was calculated according to the following equation.<sup>[13]</sup>

$$C_s = I \Delta t / (m \Delta E)$$

Where  $I$  (A) was the charge (or discharge) current,  $\Delta t$  (s) referred to the discharge time,  $m$  (g) represented the mass of capacitive material, and  $\Delta E$  (V) was the potential window. The specific capacitance at 1.0, 3.0 and 5.0 A·g<sup>-1</sup> was 416, 300, and 258 F·g<sup>-1</sup>, respectively. The specific capacitances of Cuprous (or Copper) oxide-GN composites were presented in Table 8.1. It was found that Cu<sub>2</sub>O-GN had a high capacitance compared to Cu<sub>2</sub>O and

other related materials.<sup>[31, 53, 64–66]</sup>

In Figure 8.6c, it is shown the charge-discharge curves of Cu<sub>2</sub>O-GN at 1.0 A·g<sup>-1</sup>, which prepared by different concentrations of GO. The specific capacitance of the Cu<sub>2</sub>O-GN electrode was decreased when 4 g·L<sup>-1</sup> GO was used, because excess GO could promote the reduction of copper ion in the synthesis process.<sup>[13,67]</sup> It was suggested that Cu<sub>2</sub>O-GN prepared by 3 g·L<sup>-1</sup> GO had the optimized ratio between Cu<sub>2</sub>O and GN, resulting in the highest capacitive properties. As the GO concentration increased, it was easy to generate Cu particles instead of Cu<sub>2</sub>O. In the case, the Cu<sub>2</sub>O-GN prepared with 4 g·L<sup>-1</sup> GO showed lower specific capacitance than that prepared with 3 g·L<sup>-1</sup> GO. The relation between the specific capacitance and mass normalized current of Cu<sub>2</sub>O-GN prepared with 1, 2, and 3 g·L<sup>-1</sup> GO was plotted as in Figure 8.6d. It was found that the composite which was used by 3 g·L<sup>-1</sup> GO showed the highest capacitance characteristic. In essence, the remarkable improvement of capacitive performance at 3 g·L<sup>-1</sup> GO is attributed to the superior surface characteristics of the rose rock-shaped Cu<sub>2</sub>O structure, as showed in the SEM image. The rose rock-shaped structure is favorable for electron transporting, because it had distinct 3D nanochannels with long diffusion paths. Moreover, the rose rock-shaped Cu<sub>2</sub>O was consisted of so many branched nanoarrays that furnished

numerous active sites for electrochemical reactions and shortened the diffusion distances of ion to the electroactive sites.<sup>[68, 69]</sup> Thus, the rose rock-shaped Cu<sub>2</sub>O acted as an ion-buffering reservoir to preserve more OH<sup>-</sup> ions by high rate insertion and extraction in the redox reaction and provide quicker permeating pathways of electrolyte into every nanoarrays, which enhanced kinetics of the reversible redox process for charge storage. Compared to the rose rock-shaped Cu<sub>2</sub>O-GN, the nanoflake-shaped and nanoparticle-shaped Cu<sub>2</sub>O-GN with lower porous structure were short of electroactive surface sites for the electrolytic contact, resulting in the lower charge storage capacity among the fabricated morphologies

Furthermore, the decreasing current for every sample led to higher specific capacitance, because the lower current increased the diffusing rate of electrolyte anions into the electrode. Notably, the specific capacitance of Cu<sub>2</sub>O-GN prepared with 3 g·L<sup>-1</sup> GO still remained as high as 229.0 F·g<sup>-1</sup> even at a high discharge current of 30 A·g<sup>-1</sup>, which was about 55% of their specific capacitance at 1.0 A·g<sup>-1</sup>. Comparatively, the Cu<sub>2</sub>O-GN composites prepared with 1 g·L<sup>-1</sup> and 2 g·L<sup>-1</sup> GO kept 49% and 44% of their capacitances (112.0 and 50.0 F·g<sup>-1</sup>), respectively. It was suggested that the increasing GO concentration improved the capacitance and rate capability of Cu<sub>2</sub>O-GN.

Such exceptional specific capacitance and excellent rate capability of Cu<sub>2</sub>O-GN with GO concentration could be attributed to the following aspects. Firstly, the increasing proportion of GN significantly facilitate the electrochemical performance of Cu<sub>2</sub>O-GN, which was consistent with the previous report.<sup>[13]</sup> Secondly, such advancement was also ascribed to the formation of nano Cu<sub>2</sub>O induced by GO which was proved in the SEM images. Because nano Cu<sub>2</sub>O growing on GNs could weaken the effect of GN pep interaction resulting in prevention of graphene assemble, thus facilitated the fast ion and electron transport during the charge-discharge processes. Thirdly, rose rock-shaped nano Cu<sub>2</sub>O provided a high accessible surface area with many active sites for rapid mass transfers of electrochemical materials. Therefore, the high ratio of GN could bring benefits to the electrochemical capacity of Cu<sub>2</sub>O-GN.

To evaluate the key parameters of the supercapacitor, the specific energy ( $E_s$ ) and specific power ( $P_s$ ) were calculated by the following equations:<sup>[17]</sup>

$$E_s = \frac{1}{2} C_s \Delta V^2$$

$$P_s = E_s / \Delta t$$

where  $E$  is the specific energy ( $\text{W}\cdot\text{h}\cdot\text{kg}^{-1}$ ),  $C_s$  is the specific capacitance based on the mass of the electroactive material ( $\text{F}\cdot\text{g}^{-1}$ ),  $V$  is the potential

window of discharge ( $V$ ),  $P$  is the specific power ( $\text{W}\cdot\text{kg}^{-1}$ ), and  $\Delta t$  is the discharge time (s). In Figure 8.6e, the Ragone plots of  $\text{Cu}_2\text{O}$ -GN showed that the specific energy of  $\text{Cu}_2\text{O}$ -GN prepared with  $3 \text{ g}\cdot\text{L}^{-1}$  GO was calculated to be much better than the others at the same specific power. It had a good specific energy of  $42 \text{ W}\cdot\text{h}\cdot\text{kg}^{-1}$  at a specific power of  $1500 \text{ W}\cdot\text{kg}^{-1}$  for supercapacitor, which was much higher than the values of other copper-based materials.<sup>[17, 22, 62, 70]</sup> Furthermore, the specific energy of  $\text{Cu}_2\text{O}$ -GN prepared with  $3 \text{ g}\cdot\text{L}^{-1}$  GO still remained at as high as  $31.8 \text{ W}\cdot\text{h}\cdot\text{kg}^{-1}$  even at a specific power of  $15000 \text{ W}\cdot\text{kg}^{-1}$ .

Figure 8.6f exhibits the stability of  $\text{Cu}_2\text{O}$ -GN by continuous charge-discharge measurements at  $1 \text{ A}\cdot\text{g}^{-1}$  for 1000 cycles. In the beginning, there was a little decrease of the capacitance due to the aggregation of the composites and the loss of active surface area. After 180 cycles, the capacitance retention of the composites was 86 % of its initial specific capacitance, suggesting that the  $\text{Cu}_2\text{O}$ -GN electrode had favorable electrochemical recirculating properties for electrochemical capacitors because of the synergistic effect between nano  $\text{Cu}_2\text{O}$  and GN. The good electrochemical performance as well as long cycle stability proved  $\text{Cu}_2\text{O}$ -GN as a promising candidate for supercapacitors in electrochemical energy storage devices for the future.

Sample	C (F·g <sup>-1</sup> )	Potential range (V)	Electrolyte	Current density	Reference
Cu <sub>2</sub> O-RGO	576.6	-1.0–0	6 M KOH	0.5 A·g <sup>-1</sup>	This work
CuO/N-RGO	340	-1.2–0.2	6 M KOH	0.5 A·g <sup>-1</sup>	<i>J. Electroanal. Chem.</i> <b>2014</b> , 727, 154.
Cu <sub>2</sub> O/CuO/RGO-NP	173.4	-0.4–0.4	6 M KOH	1.0 A·g <sup>-1</sup>	<i>Electrochim. Acta</i> <b>2015</b> , 152, 433.
CuO-GNS	331.9	0–0.4	6 M KCl	0.6 A·g <sup>-1</sup>	<i>J. Mater. Chem. A</i> <b>2013</b> , 1, 367.
rGO-Cu <sub>2</sub> O	195	-0.8–0.8	1 M Na <sub>2</sub> SO <sub>4</sub>	2.0 A·g <sup>-1</sup>	<i>Macromol. Res.</i> <b>2014</b> , 22, 809.

**Table 8.1** Comparison of the specific capacitance of some related materials in the literature.

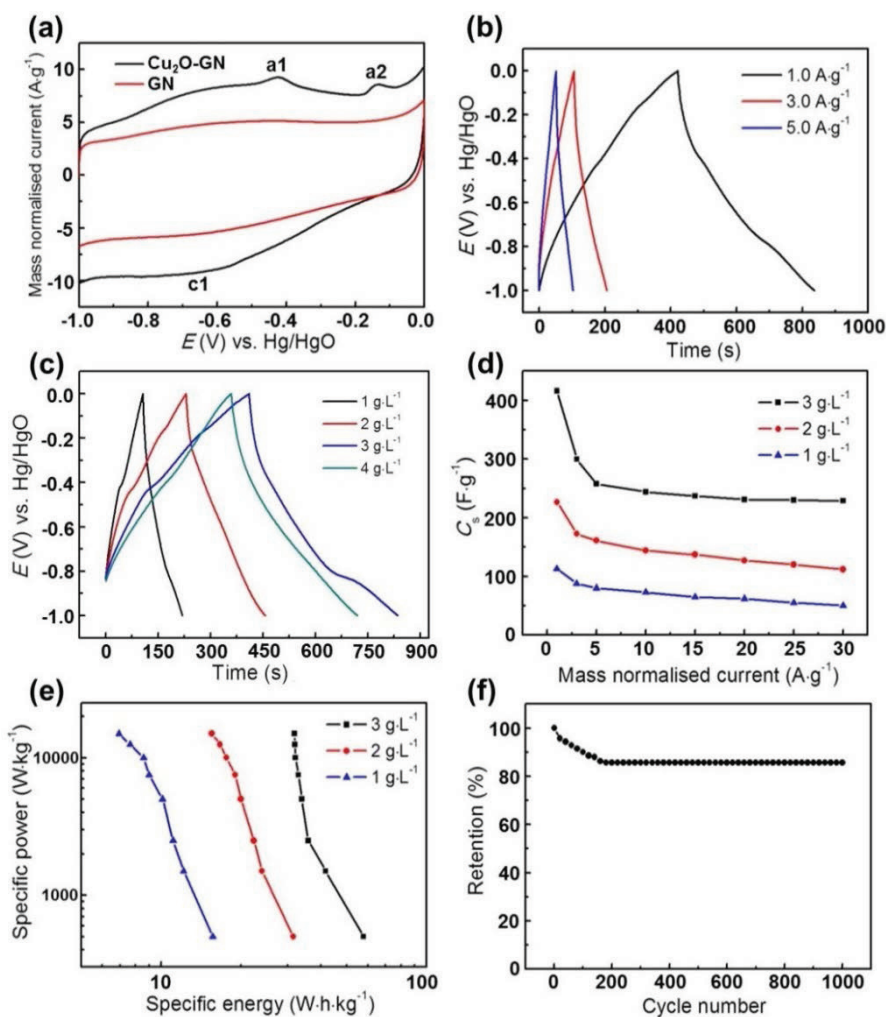


**Figure 8.6** (a) CV curves of  $\text{Cu}_2\text{O-GN}$  and GN in  $6 \text{ mol}\cdot\text{L}^{-1}$  KOH with  $0.05 \text{ V}\cdot\text{s}^{-1}$  at  $25 \text{ }^\circ\text{C}$ . (b, c) Charge-discharge curves of  $\text{Cu}_2\text{O-GN}$  electrode. (d) The relationship between the specific capacitance and the current of  $\text{Cu}_2\text{O-GN}$  prepared at different concentrations of GO. (e) Ragone plots of  $\text{Cu}_2\text{O-GN}$  with different concentrations of GO. (f) Specific capacitance retention of  $\text{Cu}_2\text{O-GN}$  at a constant current of  $1.0 \text{ A}\cdot\text{g}^{-1}$ .

In order to evaluate the Cu<sub>2</sub>O-GN electrode for practical applications, a symmetric capacitor (SC) was prepared by Cu<sub>2</sub>O-GN electrodes coating on nickel foams (6 mol·L<sup>-1</sup> KOH as the electrolyte) and the CV and the galvanostatic charge-discharge tests were used at the 0–1.4 V potential window. In Figure 8.7a, the CV curves were shown by the different scan rate from 0.01 to 0.2 V·s<sup>-1</sup>, which found nearly rectangular shapes indicating the fast charge-discharge properties of the Cu<sub>2</sub>O-GN SC. Figure 8.7b shows the galvanostatic charge-discharge results with different current densities. The specific capacitance of the Cu<sub>2</sub>O-GN SC reached 92 F·g<sup>-1</sup> at a current density of 1.0 A·g<sup>-1</sup> and still kept 65 F·g<sup>-1</sup> at a high current density of 10 A·g<sup>-1</sup>. The triangular shapes exhibited the symmetrical property in the whole potential region, indicating the good capacitive behavior of rapid charge/discharge processes. The Cu<sub>2</sub>O-GN SC specific capacitance with the total mass loading as a function of current densities is also shown in Figure 8.7c. The specific capacitance results suggested a good rate capability of the SC. Figure 8.7d shows the Ragone plot of the Cu<sub>2</sub>O-GN SC. It had a specific energy of 25.0 W·h·kg<sup>-1</sup> at 693.5 W·kg<sup>-1</sup> and still remained 17.7 W·h·kg<sup>-1</sup> at 7000 W·kg<sup>-1</sup>, which proved that the Cu<sub>2</sub>O-GN SC was capable of delivering a high specific power with a little degradation in the energy storage.

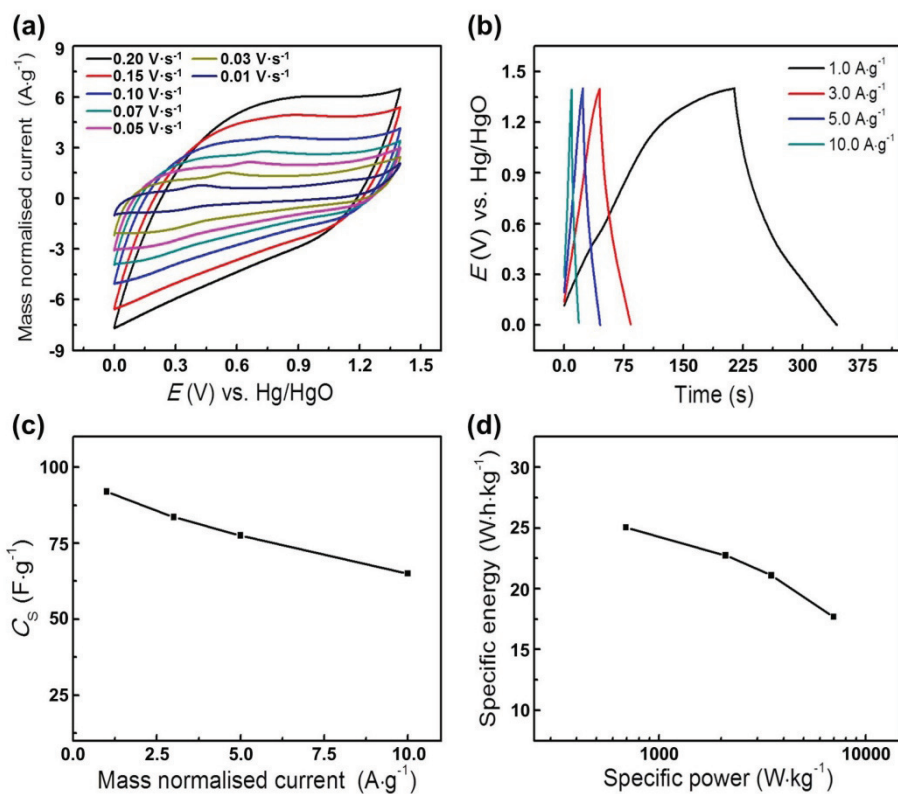


**Figure 8.7** Electrochemical performance of Cu<sub>2</sub>O-GN electrodes for symmetric supercapacitors: (a) CV curves at different scan rates from 0.01 to 0.2 V·s<sup>-1</sup>. (b) Charge-discharge curves at different mass normalised current from 1.0 to 10.0 A·g<sup>-1</sup>. (c) The relationship between the specific capacitance under different current densities from 1.0 to 10.0 A·g<sup>-1</sup>. (d) The corresponding Ragone plots related to specific energy and specific power of Cu<sub>2</sub>O-GN.

## 8.4 Conclusion

In summary, we have demonstrated a facile, simple, and cost-effective solvothermal procedure for preparing Cu<sub>2</sub>O-GN with high capacitance. Specifically, GN could affect the crystal orientation of Cu<sub>2</sub>O and lead to the growth of Cu<sub>2</sub>O crystals along a certain orientation forming rose rock-shaped Cu<sub>2</sub>O. Moreover, GO played an essential role in the transition of uniform Cu<sub>2</sub>O nanostructures and promoting the electrochemical property of Cu<sub>2</sub>O-GN. The electrochemical tests demonstrated that the rose rock-shaped Cu<sub>2</sub>O-GN exhibited good electrochemical properties. Among them, The Cu<sub>2</sub>O-GN electrode had a high specific capacitance of 415 F·g<sup>-1</sup> at 1 A·g<sup>-1</sup>, a great rate capability, and a long-term cycling stability. Thus, the special capacity of the composite suggested that Cu<sub>2</sub>O-GN would be very promising candidates for supercapacitor application.

## References

- [1] D. Chen, H. Feng, J. Li, *Chem. Rev.* **2012**, *112*, 6027.
- [2] J. Chen, C. Li, G. Shi, *J. Phys. Chem. Lett.* **2013**, *4*, 1244..
- [3] A. Ambrosi, C.K. Chua, A. Bonanni, M. Pumera, *Chem. Rev.* **2014**, *114*, 7150.
- [4] Y. Huang, J. Liang, Y. Chen, *Small* **2012**, *8*, 1805.
- [5] S.-H. Yu, D. E. Conte, S. Baek, D.-C. Lee, S.-K. Park, K. J. Lee, Y. Piao, Y.-E. Sung, N. Pinna, *Adv. Funct. Mater.* **2013**, *23*, 4293.
- [6] S.-K. Park, A. Jin, S.-H. Yu, J. Ha, B. Jang, S. Bong, S. Woo, Y.-E. Sung, Y. Piao, *Electrochim. Acta* **2014**, *120*, 452.
- [7] B. Jang, O. B. Chae, S.-K. Park, J. Ha, S. M. Oh, H. B. Na, Y. Piao, *J. Mater. Chem. A* **2013**, *1*, 15442.
- [8] X. Zhang, X. Sun, Y. Chen, D. Zhang, Y. Ma, *Mater. Lett.* **2012**, *68*, 336.
- [9] G. He, J. Li, H. Chen, J. Shi, X. Sun, S. Chen, X. Wang, *Mater. Lett.* **2012**, *82*, 61.
- [10] G. Wang, L. Zhang, J. Zhang, *Chem. Soc. Rev.* **2012**, *41*, 797.
- [11] R. R. Salunkhe, Y.-H. Lee, K.-H. Chang, J.-M. Li, P. Simon, J. Tang, N. L. Torad, C.-C. Hu, Y. Yamauchi, *Chem. - Eur. J.* **2014**, *20*, 13838.
- [12] X. Wang, G. Sun, P. Routh, D.-H. Kim, W. Huang, P. Chen, *Chem. Soc. Rev.* **2014**, *43*, 7067.
- [13] W. Zhang, B. Quan, C. Lee, S.-K. Park, X. Li, E. Choi, G. Diao, Y. Piao, *ACS Appl. Mater. Interfaces* **2015**, *7*, 2404.
- [14] X. Jin, K. Adpakpang, I. Young Kim, S. Mi Oh, N.-S. Lee, S.-J. Hwang, *Sci. Rep.* **2015**, *5*, 11057.
- [15] W. Zhang, M. Chen, X. Gong, G. Diao, *Carbon* **2013**, *61*, 154.
- [16] B. You, L. Wang, L. Yao, J. Yang, *Chem. Commun.* **2013**, *49*, 5016.
- [17] C. Zhu, J. Zhai, S. Dong, *Nanoscale* **2014**, *6*, 10077.
- [18] N. Ashok Kumar, J.-B. Baek, *Chem. Commun.* **2014**, *50*, 6298.

- [19] D. Snoke, *Science* **1996**, 273, 1351.
- [20] Y. Sui, W. Fu, Y. Zeng, H. Yang, Y. Zhang, H. Chen, Y. Li, M. Li, G. Zou, *Angew. Chem., Int. Ed.* **2010**, 49, 4282.
- [21] K. X. Yao, X. M. Yin, T. H. Wang, H. C. Zeng, *J. Am. Chem. Soc.* **2010**, 132, 6131.
- [22] C. Dong, Y. Wang, J. Xu, G. Cheng, W. Yang, T. Kou, Z. Zhang, Y. Ding, *J. Mater. Chem. A* **2014**, 2, 18229.
- [23] Y. S. Lee, D. Chua, R. E. Brandt, S. C. Siah, J. V. Li, J. P. Mailoa, S. W. Lee, R. G. Gordon, T. Buonassisi, *Adv. Mater.* **2014**, 26, 4704.
- [24] D. Liu, Z. Yang, P. Wang, F. Li, D. Wang, D. He, *Nanoscale*, **2013**, 5, 1917.
- [25] M. H. Kim, B. Lim, E. P. Lee, Y. Xia, *J. Mater. Chem.* **2008**, 18, 4069.
- [26] I. C. Chang, P.-C. Chen, M.-C. Tsai, T.-T. Chen, M.-H. Yang, H.-T. Chiu, C.-Y. Lee, *CrystEngComm* **2013**, 15, 2363.
- [27] F. Wu, Y. Myung, P. Banerjee, *Cryst. Growth Des.* **2015**, 15, 1588.
- [28] Y. Zhang, B. Deng, T. Zhang, D. Gao, A.-W. Xu, *J. Phys. Chem. C* **2010**, 114, 5073.
- [29] S. David, G. M. Kavoulakis, *Rep. Prog. Phys.* **2014**, 77, 116501.
- [30] L.-C. Chen, *Mater. Sci. Semicond. Process.* **2013**, 16, 1172.
- [31] K. Wang, X. Dong, C. Zhao, X. Qian, Y. Xu, *Electrochim. Acta* **2015**, 152, 433.
- [32] F. Jones, M. I. Ogden, *CrystEngComm* **2010**, 12, 1016.
- [33] S. Deng, V. Tjoa, H. M. Fan, H. R. Tan, D. C. Sayle, M. Olivo, S. Mhaisalkar, J. Wei, C. H. Sow, *J. Am. Chem. Soc.* **2012**, 134, 4905.
- [34] X.-Y. Yan, X.-L. Tong, Y.-F. Zhang, X.-D. Han, Y.-Y. Wang, G.-Q. Jin, Y. Qin, X.-Y. Guo, *Chem. Commun.* **2012**, 48, 1892.
- [35] M. Liu, R. Liu, W. Chen, *Biosens. Bioelectron.* **2013**, 45, 206.
- [36] B. Li, H. Cao, G. Yin, Y. Lu, J. Yin, *J. Mater. Chem.* **2011**, 21, 10645.
- [37] C. Xu, X. Wang, L. Yang, Y. Wu, *J. Solid State Chem.* **2009**, 182, 2486.
- [38] Y. Yang, C. Tian, J. Wang, L. Sun, K. Shi, W. Zhou, H. Fu, *Nanoscale*

- 2014**, *6*, 7369.
- [39] H. Meng, W. Yang, K. Ding, L. Feng, Y. Guan, *J. Mater. Chem. A* **2015**, *3*, 1174.
- [40] D. Fattakhova-Rohlfing, A. Zaleska, T. Bein, *Chem. Rev.* **2014**, *114*, 9487.
- [41] S. Stankovich, D. A. Dikin, R. D. Piner, K. A. Kohlhaas, A. Kleinhammes, Y. Jia, Y. Wu, S. T. Nguyen, R. S. Ruoff, *Carbon* **2007**, *45*, 1558.
- [42] W. S. Hummers, R. E. Offeman, *J. Am. Chem. Soc.* **1958**, *80*, 1339.
- [43] Y. Si, E. T. Samulski, *Chem. Mater.* **2008**, *20*, 6792.
- [44] C. Nethravathi, M. Rajamathi, *Carbon* **2008**, *46*, 1994.
- [45] C.-H. Kuo, M. H. Huang, *J. Am. Chem. Soc.* **2008**, *130*, 12815.
- [46] D. R. Dreyer, S. Murali, Y. Zhu, R. S. Ruoff, C. W. Bielawski, *J. Mater. Chem.* **2011**, *21*, 3443.
- [47] Y. Zhao, G. He, W. Dai, H. Chen, *Ind. Eng. Chem. Res.* **2014**, *53*, 12566.
- [48] S. Sun, X. Zhang, X. Song, S. Liang, L. Wang, Z. Yang, *CrystEngComm* **2012**, *14*, 3545.
- [49] M. C. Biesinger, L. W. M. Lau, A. R. Gerson, R. S. C. Smart, *Appl. Surf. Sci.* **2010**, *257*, 887.
- [50] S.-T. Yang, Y. Chang, H. Wang, G. Liu, S. Chen, Y. Wang, Y. Liu, A. Cao, *J. Colloid Interface Sci.* **2010**, *351*, 122.
- [51] J. Kim, L. J. Cote, F. Kim, W. Yuan, K. R. Shull, J. Huang, *J. Am. Chem. Soc.* **2010**, *132*, 8180.
- [52] L. Q. Lu, Y. Wang, *J. Mater. Chem.* **2011**, *21*, 17916.
- [53] B. Zhao, P. Liu, H. Zhuang, Z. Jiao, T. Fang, W. Xu, B. Lu, Y. Jiang, *J. Mater. Chem. A* **2013**, *1*, 367.
- [54] Y. Xia, Y. Xiong, B. Lim, S. E. Skrabalak, *Angew. Chem., Int. Ed.* **2009**, *48*, 60.
- [55] Y. Luo, S. Li, Q. Ren, J. Liu, L. Xing, Y. Wang, Y. Yu, Z. Jia, J. Li,

- Cryst. Growth Des.* **2007**, *7*, 87.
- [56] M. Zhu, Y. Wang, D. Meng, X. Qin, G. Diao, *J. Phys. Chem. C* **2012**, *116*, 16276.
- [57] M. Zhu, D. Meng, C. Wang, G. Diao, *ACS Appl. Mater. Interfaces* **2013**, *5*, 6030.
- [58] D. A. Barlow, J. K. Baird, C.-H. Su, *J. Cryst. Growth* **2004**, *264*, 417.
- [59] Z. Yin, C. Lee, S. Cho, J. Yoo, Y. Piao, Y. S. Kim, *Small* **2014**, *10*, 5047.
- [60] L. D. Burke, M. J. G. Ahern, T. G. Ryan, *J. Electrochem. Soc.* **1990**, *137*, 553.
- [61] G. Wang, J. Huang, S. Chen, Y. Gao, D. Cao, *J. Power Sources* **2011**, *196*, 5756.
- [62] B. Vidhyadharan, I. I. Misnon, R. A. Aziz, K. P. Padmasree, M. M. Yusoff, R. Jose, *J. Mater. Chem. A* **2014**, *2*, 6578.
- [63] M. Kang, A. A. Gewirth, *J. Phys. Chem. B* **2002**, *106*, 12211.
- [64] Y. Li, K. Ye, K. Cheng, D. Cao, Y. Pan, S. Kong, X. Zhang, G. Wang, *J. Electroanal. Chem.* **2014**, *727*, 154.
- [65] H. Park, T. Han, *Macromol. Res.* **2014**, *22*, 809.
- [66] S. M. Pawar, J. Kim, A.I. Inamdar, H. Woo, Y. Jo, B.S. Pawar, S. Cho, H. Kim, H. Im, *Sci. Rep.* **2014**, *6*, 21310.
- [67] W. Zhang, Z. Yin, A. Chun, J. Yoo, Y. S. Kim, Y. Piao, *ACS Appl. Mater. Interfaces* **2016**, *8*, 1733.
- [68] S.-I. Kim, J.-S. Lee, H.-J. Ahn, H.-K. Song, J.-H. Jang, *ACS Appl. Mater. Interfaces* **2013**, *5*, 1596.
- [69] G.-R. Li, H. Xu, X.-F. Lu, J.-X. Feng, Y.-X. Tong, C.-Y. Su, *Nanoscale* **2013**, *5*, 4056.
- [70] H. Sun, L. Cao, L. Lu, *Energy Environ. Sci.*, **2012**, *5*, 6206.

## 국 문 초 록

구리 나노선과 이의 복합체는 차세대 기능성 전극을 위한 유망한 전도성 물질로서 주목을 받고 있으며 이에 따른 많은 연구가 진행되고 있다. 구형, 판형, 정육면체형 등 다른 모양의 나노 입자들에 비해, 구리 나노선은 1차원적인 구조와 높은 종횡비로 인하여 특유의 성능을 나타내고 있다. 또한, 구리 나노선은 용액-공정으로 사용이 가능할 뿐만 아니라, 비용이 저렴하며, 전도성이 높고 유연성이 우수하다는 등 다양한 장점으로 인하여 전극 물질로서 큰 잠재적 가치를 보이고 있다. 본 연구에서는 차세대 전자 소자를 위한 구리 나노선과 이의 복합체를 합성하는 방법 및 다양한 기능성 전극의 제작 방법을 중점적으로 제안하였다.

첫째, 전체적인 용액-공정으로 구리 나노선을 이용한 투명전극을 제작하였다. 현재 투명전극 소재로 산화 인듐-주석이 가장 많이 사용되고 있다. 그러나 이 물질은 이온결합을 이용한 세라믹 물질이기 때문에 휘임에 취약하다. 반면에, 금속 나노선 기반 투명전극은 쉽게 휘 수 있기 때문에 차세대 유연 전자 소자에 적용이 가능하다. 본 연구에서는 이중 폴리올 환원법으로 휘어진 구리 나노선을 합성하고, 메니스커스-드래깅 증착법을 이용하여 유리와 PET 기판 위에 균일하게 코팅하였다. 그 다음, 용매-담금 가열법을 이용하여 저온에서 구리 나노선을 연결해 줌으로써 높은 투과도, 전도성, 유연성 및 내구성을 지닌 유연 투명전극을 제작하였다.

둘째, 다중 폴리올 합성법, 메니스커스-드래깅 증착법, 폴리 우레탄-낙인 패터닝법, 용매-담근 용접법, 우레탄-내장 전사법 등과 같은 자체적으로 설계한 혁신적인 기술들로 휘어진 구리 나노선을 기반으로 하는 유연한 투명전극을 제작하였다. 이와 같은 방법으로 제작된 유연 투명전극은 기존의 높은 제작 비용, 낮은 견고성, 높은 표면 거칠기 및 패터닝의 어려움 등의 기술적인 문제점들을 효과적으로 극복하였을 뿐만 아니라 높은 투과도, 낮은 면저항, 우수한 기계적 안정성과 매끄러운 표면을 구현하였다.

셋째, 구리 나노선과 환원된 산화 그래핀의 하이브리드 복합체를 이용하여 폴리에스터 옷에 착용 가능한 유연한 전극을 개발하였다. 이 과정에서 합성된 복합체의 모양은 구리 나노선들이 그래핀들을 다리처럼 이어주는 형태이다. 이때, 구리 나노선은 전자 전달을 위한 경로를 제공하고, 환원된 산화 그래핀은 구리 나노선이 접촉점에서 산화되는 것을 방지해주는 역할을 하여, 필름의 높은 전도도, 우수한 산화 안정성 및 유연성을 구현하였다. 또한, 복합체는 간단한 여과 방법으로 폴리에스테 천 위에 증착함으로써, 추가적인 처리 공정 없이, 쉽고 간편하게 옷에 착용 가능한 유연한 전극을 제작하였다.

마지막으로, 3차원 구조를 가지는 구리 나노선과 탄소 나노 튜브의 복합체를 이용하여 급속 충-방전할 수 있는 리튬이온전지의 음극을 제작하였다. 1차원 구조 및 높은 전도성을 갖는 구리 나노선과 탄소 나노 튜브의 높은 중횡비와 큰 비표면적을 이용하여 전자와 이온의 빠른 이동도를 구현하였다. 또한, 구리 나노선 필름의

다공성 구조를 이용하여 탄소 나노 튜브와 긴밀히 접촉한 구조를 형성함으로써, 제작된 음극의 저항을 감소시켰고, 리튬이온전지의 충-방전 성능을 향상시켰다. 이런 복합체로 제작된 리튬이온전지는 높은 전류에서도 고용량 및 높은 쿨롱 효율을 나타냈다. 또한, 유연성 리튬이온전지에 적용하여 10mm의 반경으로 1,000번 휘었을 때에도 높은 용량을 유지하였다.

결과적으로, 본 연구에서는 구리 나노선과 이의 복합체의 합성 연구를 위주로 진행하였다. 또한, 이런 나노 물질들을 이용하여 여러 가지 기능성 전극들을 제작하는 방법도 제안하였다. 구리 나노선을 기반으로 하여 제작된 유연 투명전극, 옷에 착용 가능한 전극, 리튬이온전지의 집전체같은 기능성 전극들은 기존보다 저렴하고 간단한 용액-공정법으로 제작하였을 뿐만 아니라 높은 전도성과 유연성을 보이고 있어, 차세대 유연 소자의 전극으로 사용될 만한 충분한 가능성을 보인다.

**주요어:** 구리 나노선, 유연 투명전극, 착용 가능한 전극, 리튬이온전지, 집전체.

**학 번:** 2014-31481